MAX PLANCK INSTITUTE
FOR DYNAMICS OF COMPLEX
TECHNICAL SYSTEMS
MAGDEBURG

PCF

PHYSICAL AND CHEMICAL
FOUNDATIONS OF
PROCESS ENGINEERING

Separation of Solid Solutions using Counter-Current Crystallization: Improved Operation through Antisolvents

Dissertation

Doktoringenieur

(Dr.-Ing.)

von:

M.Sc. Vico Tenberg

geb. am 22.09.1993 in Rheine

genehmigt durch die Fakultät für Verfahrens- und Systemtechnik der Otto-von-Guericke Universität Magdeburg

Promotionskommission:

Apl. Prof. Dr. rer. nat.	Heike Lorenz	(Vorsitz)
Prof. Dr.-Ing.	Andreas Seidel-Morgenstern	(Gutachter)
Prof. Dr.-Ing.	Michael Mangold	(Gutachter)
Prof.	Allan S. Myerson	(Gutachter)

Eingereicht am: 3. März 2023
Promotionskolloquium am: 7. Juli 2023

Abstract

Separating different components present in a solid solution is a challenging purification task. The components cannot be isolated in a single crystallization step. Crystallization-based compound-specific enrichment in either the liquid or solid phase can only be achieved by multistage or counter-current crystallization. Apart from developing such processes, solid-liquid equilibria and crystallization behavior determination is non-trivial for such systems and requires in-depth investigations applying a multitude of analytical methods, e.g. HPLC, PXRD, and DSC/FSC.

In this work, the impact of utilizing antisolvents to enhance crystallization processes are investigated experimentally for the model solid solution forming system L-valine /L-leucine and various water/antisolvent mixtures. Ethanol, isopropanol, and acetone were chosen as antisolvents. The experimentally determined solid-liquid equilibria were modeled empirically as well as predictively via a novel theoretical approach. The latter is based on combining NRTL and PC-SAFT models to describe the solid and liquid phases, respectively. The empirical models were used in a predictive process simulation of the counter-current crystallization to plan corresponding experiments. The predictions were successfully validated at pilot plant scale.

As a basis for future optimizations, a new quantification approach for solid solution separations was developed and demonstrated for the model system to identify optimal crystallization strategies and conditions. The L-valine /L-leucine system exhibits alyotropic behavior in analog to azeotropes in vapor-liquid equilibria. Using the methods and approaches developed in this work, a novel separation process based on a dual counter-current crystallization is capable of purifying also other alyotropic mixtures.

This work utilized various experimental and theoretical investigations of solid solutions and counter-current crystallization processes and deepened system knowledge and process understanding. These insights can be widely utilized to conceptually design counter-current crystallization processes capable to solve complex separation problems involving solid solutions.

Kurzzusammenfassung

Die Trennung von Mischkristallen stellt eine schwierige Aufgabe dar, da diese in einem einzigen Kristallisationsschritt nicht komplett aufgereinigt werden können. Eine Anreicherung durch Kristallisation der einzelnen Komponenten in der festen oder flüssigen Phase kann ausschließlich durch mehrstufige Prozesse wie fraktionierte oder Gegenstromkristallisation erreicht werden. Neben der Entwicklung solcher Prozesse, sind auch die Messung der komplizierten Fest-Flüssig Phasengleichgewichte und die Bewertung des Kristallisationsverlaufes nicht trivial. Hierzu werden aufwendige Experimente und analytische Methoden, wie beispielsweise HPLC, PXRD, und DSC/FSC, benötigt.
In dieser Arbeit wird der Einsatz der Verdrängungskristallisation zur Verbesserung der Effizienz des Kristallisationsprozesses für das Modellsystem der Aminosäuren L-Valin und L-Leucin in unterschiedlichen Wasser/Antisolvent-Mischungen untersucht. Als Verdrängungsmittel wurden hierzu Ethanol, Isopropanol und Aceton ausgewählt. Die analysierten Fest-Flüssig-Gleichgewichte dieser Systeme wurden sowohl empirisch als auch mit einem neuen kombinierten Ansatz aus NRTL und PC-SAFT Modellen prädiktiv modelliert. Die empirische Modellierung wurde in einer Prozesssimulation eines Gegenstromkristallisationsprozesses verwendet. Die Simulationsergebnisse wurden genutzt, um validierende Experimente im Pilotanlagen-Maßstab durchzuführen.
Um zukünftig weitere Optimierungen durchführen zu können, wurde eine Methode entwickelt, welche die Mischkristalltrennung unabhänging von der gewählten Kristallisationsstrategie und den Bedingungen quantifizieren kann.
Das Modellsystem aus L-Valin und L-Leucin zeigt ein alyotropes Phasenverhalten. Dieses ist analog zum bekannten azeotropen Phasenverhalten von Gas-Flüssig-Gleichgewichten. Mit den in dieser Dissertation erarbeiteten Strategien wurde ein neuer dualer Gegenstromkristallisationsprozess entwickelt, mit welchem alyotrope Mischungen aufgereinigt werden können.
Diese Arbeit stellt verschiedene experimentelle sowie theoretische Untersuchungen des Phasenverhaltens von Mischkristallen sowie der Gegenstromkristallisation vor. Die Ergebnisse tragen zu bei ein tieferes Verständnis für diese komplexen Thematiken zu schaffen. Dieses Verständnis kann genutzt werden, um Gegenstromkristallisationsprozesse kozeptionell zu planen und auszulegen, welche in der Lage sind komplexe Trennprobleme zu lösen.

Preface

A list of publications, connected with this dissertation, is given below. The following thesis partly takes results and approaches from these works, as indicated accordingly.

- The alyotrope separation, proposed in Section **4.4.4**, is partly published in [1].
- Publications [2] and [3] focus on thermodynamic modeling of solid solution equilibria, detailed in Section **3.4**. In [4], single solute equilibria are modeled using a similar approach.

Additionally, a master thesis was supervised as part of this dissertation. In her thesis, M.Sc. M. Hokmabadi determined solubilities and empirical model parameters of L-valine /L-leucine solid solutions in various water/antisolvent mixtures, whose results are used in Section **3.3** and [2].

[1] V. Tenberg, M. Sadeghi, A. Seidel-Morgenstern, and H. Lorenz, "Bypassing thermodynamic limitations in the Crystallization-based separation of solid solutions," *Sep. Purif. Technol.*, vol. 283, p. 120 169, 2022

[2] V. Tenberg, M. Hokmabadi, A. Seidel-Morgenstern, H. Lorenz, and M. Sadeghi, "Investigation of the Antisolvent Effect on the Phase Behavior of Amino Acid Solid Solutions," *Ind. Eng. Chem. Res.*, vol. 62, no. 1, pp. 753–761, 2023

[3] M. Sadeghi, V. Tenberg, S. Münzberg, A. Seidel-Morgenstern, and H. Lorenz, "Phase equilibria of L-Valine/L-Leucine solid solutions," *J. Mol. Liq.*, vol. 340, p. 117 315, 2021

[4] M. Sadeghi, F. Cascella, V. Tenberg, A. Seidel-Morgenstern, and H. Lorenz, "Solubility analysis of pharmaceuticals guaifenesin, ketoprofen, and artemisinin in different solvents," *J. Mol. Liq.*, vol. 343, p. 117 503, 2021

Contents

1. Introduction

Crystallization, being one of the oldest thermal separation processes, is an energy efficient unit operation exploited for purification and product design in many industrial, pharmaceutical, and scientific applications [5, 6]. To achieve crystallization, a multitude of different strategies can be applied, among others these are evaporative, cooling, melt, antisolvent, pH-shift, reactive crystallization etc.. Crystallization is commonly utilized in single step purification processes, in either batch, e.g. [7, 8], for increased control and flexibility or continuous operation, e.g. [9], to increase process productivity. Regardless of the chosen crystallization strategies or process types, knowledge about the solid-liquid equilibria, their corresponding phase diagrams, and thermodynamic descriptions [10, 11], is essential to design efficient and productive crystallization processes. This holds especially true, when dealing with more complex separation tasks, i.e. solid phase miscibility, mother liquor inclusion, etc.. Then, a single-step purification might not be sufficient to achieve satisfying separation. For such separation problems, multistage processes like fractional [12] or counter-current crystallization [13] are required. Solid phase miscibility, observed in solid solutions, or mixed crystals, [14, 15], occurs in roughly 14 % of known organic systems [16]. Such behavior is still relatively unknown and might thus be often disregarded. The multistage separation of solid solutions has been increasingly studied in recent years [12, 13, 17–26] for numerous model systems exhibiting various solid state miscibility behaviors. E.g. in [20], partial solid solutions of C_{60} and C_{70} fullerenes were investigated, while previous works in our research group focused on crystallization-based purification of potassium sulfate/ammonium sulfate mixtures, which exhibit complete miscibility over the whole composition range [26].

This thesis aims to extend previous works by combining counter-current crystallization with antisolvent crystallization and to derive conceptual heuristics for the design of efficient counter-current crystallization processes. This is fundamentally based on in-depth knowledge of solid-liquid equilibria. Therefore, in Sections **2.1.1** and **2.1.2**, various binary and ternary phase diagrams are introduced, which are discussed in detail, especially for solid solution forming systems. Simultaneously, in Section **2.1.2**, Roozeboom distribution diagrams [18] are partly derived and explained in analogue to their corresponding $x-y$ distribution diagrams known from vapor-liquid equilibria [27]. Basic thermodynamic expressions, relevant for solid-liquid equilibria, are introduced in Section **2.2**. Following these fundamentals, specific thermodynamic models such as Perturbed-Chain Statistical Associating Fluid Theory (PC-SAFT) and Non-Random Two-Liquid (NRTL) as well as empirical models for solid-liquid equilibria description are given in Sections **2.2.1**, **2.2.2**,

and **2.2.3**, respectively.
For the experimental part of this work, the amino acids L-valine and L-leucine were chosen as model systems. They exhibit complete miscibility [28] in the solid state as well as a "salting-in" effect, resulting in a so-called alyotrope [29, 30]. The solid-liquid equilibria of these amino acids in various water/antisolvent mixtures were extensively investigated experimentally and are described in Chapter **3**. High-performance liquid chromatography (HPLC) and powder X-ray diffraction (PXRD) were utilized as analytical methods and are explained in Section **3.2.2**. Ethanol, isopropanol, and acetone were chosen as model antisolvents. In Section **3.4**, predictive as well as semi-predictive approaches based on a combination of PC-SAFT and NRTL models are proposed. These are utilized to describe the determined quaternary equilibria of the mentioned model systems. In [31], a co-crystal V_3L was found for this system. Its stability and influence on the separation via counter-current crystallization are investigated in Section **3.5**.
Utilizing analogies to rectification, counter-current crystallization is introduced as a more efficient alternative to fractional crystallization and a novel quantification method is developed in Section **4.1**, which is partly based on the catalyst effectivity [32]. In Section **4.2**, a mathematical model to describe various crystallization strategies within a counter-current crystallization process is derived. This model is incorporated into an empirical process simulation in Section **4.3**. Using this simulation alongside a sensitivity analysis, optimal crystallization conditions and strategies for various regions of the solid-liquid equilibria of L-valine /L-leucine mixtures, are determined in Section **4.3.2**. Apart from purely simulative studies, this work finally features pilot plant scale experiments, for which the setup and its equipment are described in Section **4.4.1**. In Section **4.4.3**, results of pilot plant experiments are used to validate predictions for evaporative and antisolvent crystallization at different temperatures. As mentioned above, the L-valine /L-leucine system exhibits alyotropism, which limits the achievable purity by conventional counter-current crystallizations. This limitation is comparable to the effect of an azeotrope limiting the purity in a given vapor-liquid equilibrium, which can be achieved by e.g. rectification. During this work, a new process, shifting the alyotropic composition with antisolvent crystallization, analogue to pressure swing rectification, was proposed, predicted, and successfully validated. Section **4.4.4** gives detailed insight into this process, its experimental realization and theoretical prediction. Finally, Section **4.5** discussed potential process variants and optimizations based on the insight gathered on counter-current crystallization during this work. Processes for the separation of distinct co-crystals, in solid solution forming systems, as well as ternary solid solutions are proposed.
In Chapter **5**, a summary and conclusion of this work and an outlook of potential future research is given.

2. Thermodynamics of Crystallization and Theoretical Background

Crystalline compounds, as opposed to amorphous solids, show an ordered three-dimensional lattice in the solid phase. These lattices are generally defined by a repeating unit cell. In semi-amorphous or semi-crystalline material, the ordered crystalline structures are encapsulated by unordered amorphous regions [33]. These different states of solid matter are visualized in Figure 2.1.

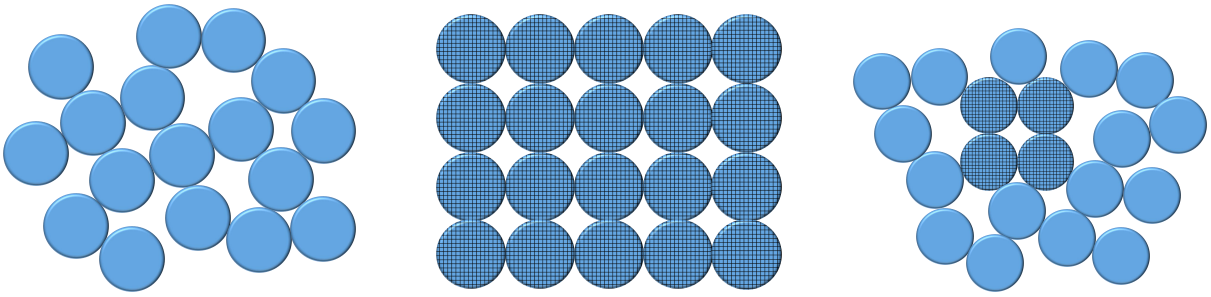

(a) Amorphous **(b)** Crystalline **(c)** Semi-Amorphous

Figure 2.1: Schematic two dimensional depiction of various solid-phase states. Patterned spheres indicate an ordered lattice.

Amorphous solid phases are inherently metastable in nature and will transform into crystalline structures given enough time, if kinetic resistances are surmountable. This metastability of amorphous materials is used in e.g. quenching. Here, hot material is submerged in cold liquid, to quickly decrease the materials temperature and decrease potential formation of ordered lattices [34]. The obtained metastable (semi-)amorphous material may have increased durability and strength as its crystalline counterpart, as known from metals etc.. Apart form amorphism, various materials may crystallize in different metastable and stable crystal structures, which is defined as polymorphism. Similar to quenching, distinct polymorphs can be obtained by different conditions. E.g. L-glutamic acid can be crystallized from aqueous solution as a metastable α and stable β polymorph at temperatures below 9 °C and above 27 °C, respectively [35].
Crystals can be obtained by crystallization from its melt, from solution, or from its gaseous phase. A melt solidifies when its temperature T falls below its melting temperature T_m. In a solution, crystallization occurs when the saturation concentration c^* is exceeded. The

exact value of c^* is highly dependent on the solute, solvent and temperature. The temperature dependency of the saturation concentration of a given solute in a solvent, also called solubility line, can be showcased in a c-T-diagram (see Figure 2.2). Generally, the solubility increases with increasing temperature of the system. Since the solubility line describes the saturation concentration, solutions below this line are defined as undersaturated while supersaturation describes solutions above this line. In the case of crystallization of a supersaturated solution, the concentration decreases continuously until the saturation concentration on the solubility line is reached.

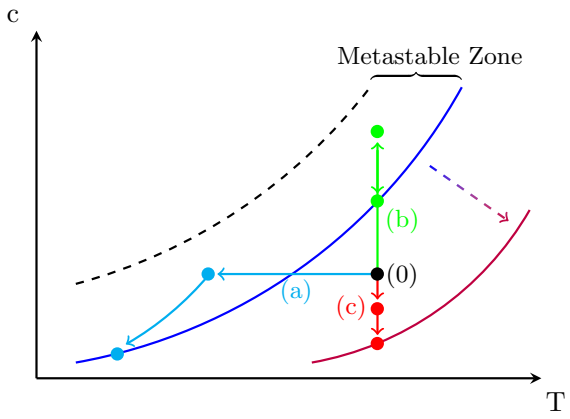

Figure 2.2: Solubility diagram of a pure solute in a solvent. Blue and purple lines: solubility lines of the solute at different solvent compositions; black dashed line: upper boundary of the metastable zone; (0) initial condition; (a, cyan) cooling, (b, green) isothermal evaporative, and (c, red) isothermal antisolvent crystallization.

Additionally, Figure 2.2 showcases the metastable zone (between blue and dashed black line) in which a supersaturated solution is present, however, practically no spontaneous nucleation takes place [36]. In this region, controlled crystallization can be performed by introducing small crystals to the solution, also called seeding. These seed crystals will grow in the supersaturated solution while decreasing the concentration until the saturation concentration is reached. If the metastable region is surpassed, the supersaturated solution becomes unstable and will spontaneously nucleate, which leads to uncontrolled crystallization.

In Figure 2.2, three crystallization methods, i.e. cooling (cyan, a), evaporative (green, b), and antisolvent crystallization (red, c), are illustrated. In the case of cooling crystallization, starting at the initial composition (0), the temperature is lowered until the solution becomes supersaturated and is located within the metastable zone. Here, crystallization is initialized, e.g. by seeding. Thus, the concentration of the solution starts to decrease with decreasing temperature until the saturation concentration on the solubility line is reached. Similarly, for isothermal evaporative crystallization, the concentration of the solution is increased by reducing the solvent fraction by evaporation to reach supersaturation. In the

metastable zone, crystallization can again be initialized and the concentration decreases to the saturation concentration on the solubility line without a change in temperature. With antisolvent crystallization, a more complex method is introduced. Here, a second solvent is added to the solution. Ideally, this antisolvent shows good miscibility with the first solvent, while possessing a low solubility for the solute. Due to the mixing of the solvents, the overall solubility for the solute decreases. In Figure 2.2, this is showcased by a change of the solubility line (from blue to purple, dashed arrow). First, the initial concentration is decreased slightly by the increased amount of solvent phase for a constant amount of solute. However, due to the change of the solubility, the solution becomes supersaturated. Following, the solute will crystallize until the supersaturation is reduced to the new saturation concentration in the present solvent mixture. In the antisolvent crystallization, in addition to temperature, solubility is dependent on the amount of added antisolvent and the specific compound used as antisolvent. Antisolvent crystallization is typically applied to reach high supersaturations, far exceeding the metastable zone. This results in heavy nucleation and therefore small, narrow crystal size distributions and increased yields. This is useful in the manufacturing of active pharmaceutical ingredients (API) used in inhalable aerosols, where small crystals are required to pass into the lungs of patients [37]. However, due to an additional compound present, potential safety regulations and recycling streams increase process complexity.

2.1 Solid-Liquid Equilibria and Phase Diagrams

In a system at equilibrium, one or multiple phases are in a stable state, depending on their composition and the systems conditions. The Gibbs phase rule gives an universal relation between the number of phases P, the number of independent components N, and the degrees of freedom F of a given system in equilibrium [38].

$$P + F = N + 2 \tag{2.1}$$

For crystallization processes, the pressure of a given system is generally neglected as degree of freedom, due to the insignificant effect on the solubility and the solid phase behavior, for melt and solution crystallization. Therefore, for pressure as a given degree of freedom without influence on the system, Eq. (2.1) is simplified to Eq. (2.2) [36].

$$P + F = N + 1 \tag{2.2}$$

Using Gibbs phase rule, the degrees of freedom, i.e. the number of independent variables,

can be determined for a given system, with which phase diagrams can be constructed. In the following sections various binary melt and ternary solution phase diagrams, including various solid phase behaviors, are presented and discussed.

2.1.1 Binary Systems

For a binary system, consisting of distinct components A and B, several phase regions can be determined in a melt phase diagram. In Figure 2.3, a composition-temperature diagram of an eutectic A and B mixture, in which the melting temperatures $T_{m,A}$ and $T_{m,B}$ are given.

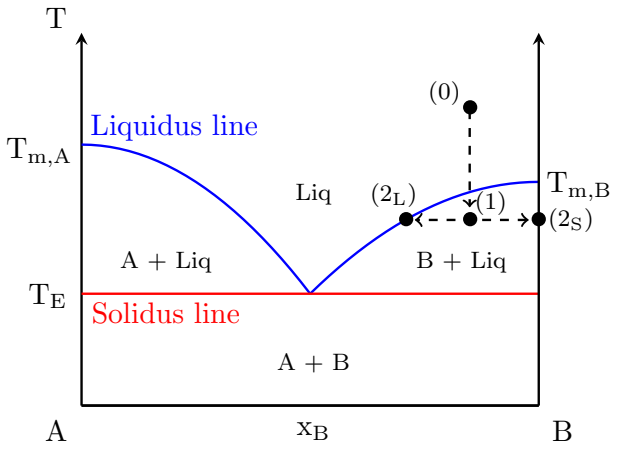

Figure 2.3: Binary eutectic phase diagram of A and B. Blue: liquidus lines; red: solidus line. (0) initial composition; (1) metastable melt; (2_S) pure solid and (2_L) its corresponding liquid phase. A and B within the phase diagram describe pure solid phases.

The liquidus lines (blue) and the solidus line (red) divide the liquid and solid phases from the mixed phase regions. The intercept of these lines is called the eutectic point, which is defined as the lowest possible melting point of a mixture. Its melting temperature is called eutectic temperature T_E. At the eutectic point, the maximum number of phases can be determined as $P_{max} = 3$ with no available degrees of freedom $F_{min} = 0$. Here, two solid phases, i.e. pure A and B, and one liquid phase at eutectic composition x_E are present. Neither temperature nor the composition can be changed without causing a phase change. Conversely, the minimum number of phases $P_{min} = 1$ corresponds to the maximum degrees of freedom $F_{max} = 2$. Here, temperature and the fraction of one component can be changed independently without requiring a phase change. The fraction of the second component is given by Eq. (2.3) as a function of the first component for $N = 2$.

$$\sum_{i=1}^{N} x_i = 1 \tag{2.3}$$

$$x_i = \frac{n_i}{\sum_{j=1}^{N} n_j} \tag{2.4}$$

Where x_i is the molar fraction and n_i is the molar amount of component i.
Below the solidus line, both components are solidified in a biphasic solid mixture. For $P = 2$, Eq. (2.2) yields one degree of freedom $F = 1$, which here, is temperature. Since only pure components are present, the composition of both phases is constant $x_A^{pure} = x_B^{pure} = 1$ and therefore, cannot be changed. Between the liquidus and solidus lines, a mixture of pure solid A or B and a mixed liquid phase having a composition on the liquidus line are present. Similarly, for a biphasic region, Eq. (2.2) gives $F = 1$, i.e. the temperature or composition of the liquid phase. In Figure 2.3, an arbitrary cooling crystallization process path is described. Stating at the initial liquid composition (0), the temperature is decreased until the liquidus line is crossed and the metastable mixture (1) is reached. Upon crystallization, (1) splits into a pure solid (2_S), here B, and a mixed liquid phase (2_L) along its connecting tie line. Therefore, changes to temperature in this region will directly correspond to a change in the liquid phase composition and vice versa. For a crystallization-based purification of an A/B mixture, such regions are preferred, since pure component can easily be separated after crystallization. The amounts and compositions of the resulting phases can directly be calculated by total and partial molar balances.

$$n_{0,L} = n_{2,L} + n_{2,S} \tag{2.5}$$

$$n_{0,L} x_{i,0,L} = n_{2,L} x_{i,2,L} + n_{2,S} x_{i,2,S} \tag{2.6}$$

Potentially, A and B might form co-crystals, which are defined as homogeneous crystalline compounds, consisting of two or more components with a constant molar ratio of the components, e.g. the arbitrary co-crystal A_1B_1, or AB in short, has a molar ratio A:B of 1:1. Since co-crystals are distinct compounds, they possess distinct melting temperatures, solubilities, etc.. Figure 2.4 shows a binary phase diagram for two components A and B including AB co-crystal formation.

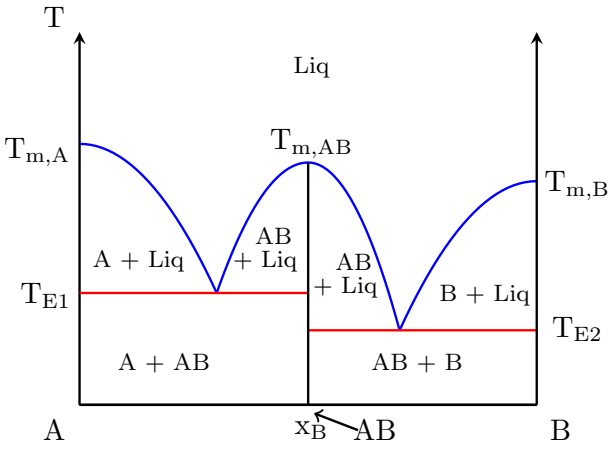

Figure 2.4: Binary eutectic phase diagram of A and B containing the co-crystal AB. Blue: liquidus lines; red: solidus lines; black: co-crystal compositional line.

Due to the melting temperature $T_{m,AB} \neq T_{m,A} \neq T_{m,B}$ of AB, two eutectic points are formed at T_{E1} and T_{E2}. Since AB is a pure component, Gibbs phase rule can again be used to determine the degrees of freedom in the various regions to the left and right of the co-crystal, in analogue to a simple eutectic system as shown in Figure 2.3. For the co-crystal itself, $P = N = 1$ and therefore, $F = 1$ is valid. Since the composition is constant, the degree of freedom is temperature, which can be changed along the black vertical line (see Figure 2.4) denoting the co-crystal AB.

Alternatively to systems crystallizing as pure components, so-called solid solutions, or mixed crystals, crystallize as one-phasic component mixtures [14, 15, 39]. Unlike co-crystals, solid solutions do not possess a specific constant composition or a distinct unit cell composition. Here, components A and B are statistically distributed in the crystal lattice. A and B can be integrated into each others lattices either subsitutionally, if similar molecule sizes and crystal lattices are present, or interstitially, where guest molecules are integrated in-between host molecules in the host's crystal lattice. In literature, many examples of inorganic solid solutions are found. E.g. finely tuned solid solutions in superconductors can improve their conducting properties [40–42]. Recently, organic solid solutions have been found to improve photovoltaic performances due to their tunable properties [43, 44]. In [45], a continuous antisolvent crystallization process was proposed to manufacture tuned organic solid solutions with amino acids L-isoleucine, L-leucine , and L-valine . Contrary to the design and manufacturing of solid solutions, their separation via fractional and counter-current crystallization was discussed in various publications prior to this work [12, 13, 17–26]. More detailed information on the separation of solid solutions via counter-current crystallization are given in Chapter **4**.

Solid solutions can possess complete or partial miscibility in the solid state. Their respective phase diagrams are presented in Figure 2.5.

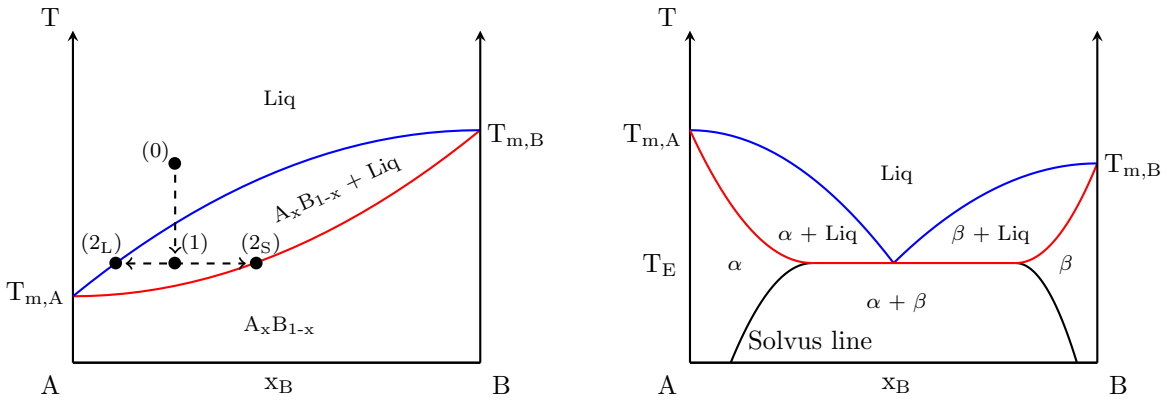

(a) Complete solid solution **(b)** Partial solid solution

Figure 2.5: Binary phase diagrams including complete (left) and partial (right) solid solutions of A and B. Blue: liquidus lines; red: solidus lines; black: solvus lines. Complete solid solution: A_xB_{1-x}; partial solid solution: α and β for A- and B-rich solid solutions, respectively. (0) initial composition; (1) metastable melt; (2_S) equilibrated solid and (2_L) liquid phases.

Figure 2.5a depicts a melt phase diagram of a complete solid solution forming system. Here, the composition change of the complete solid solution over the whole composition range is described by A_xB_{1-x}. In analog to eutectic systems, Gibbs phase rule can be applied to such systems as well. Here, the liquid and solid phases are one-phasic $P = 1$ and consist of two components $N = 2$. Therefore $F = 2$ holds according to Eq. (2.2), with temperature and composition being variable independently. Between the solidus and liquidus lines, the number of phases is increased to $P = 2$ and following, temperature and composition are dependent on each other. Contrary to eutectic systems in Figure 2.3, no pure component is crystallized by decreasing the temperature from point (0) to point (1) and instead yields a mixture in the solid (2_S) and liquid phases (2_L). Analogue to immiscible systems, crystallization for solid solutions can be described by Eqs. (2.5) and (2.6). Due to the crystallization, each of these mixtures is enriched in one the present components. Hence, near-complete resolution requires multistage crystallization (see Chapter **4**).

Apart from complete miscibility, partial miscibility behavior in the solid phase is presented in Figure 2.5b. Here, α and β denote solid solutions based on the host lattices of component A and B, respectively. The new regions containing solely α or β, between solidus and solvus lines, are therefore one-phasic $P = 1$, while still including A and B, thus $N = 2$. This again leads to the temperature and compositions being independent similar to the completely liquid regime above the liquidus line. The biphasic regions ($P = 2$, $N = 2$) between the liquidus and solidus lines as well as between both solvus lines show a temperature dependent composition for both phases. Hence, a crystallization-based purification can only be performed in these biphasic regions.

2.1.2 Ternary Systems

While Section **2.1.1** detailed melt phase diagrams of binary A and B mixtures, this chapter focuses on systems of A and B in presence of a solvent phase Solv. Here, crystallization is limited by the saturation of the solvent phase instead of the melting temperature of the crystals. The related isothermal analog to Figure 2.3, in which A and B exhibit eutectic behavior, is shown in Figure 2.6.

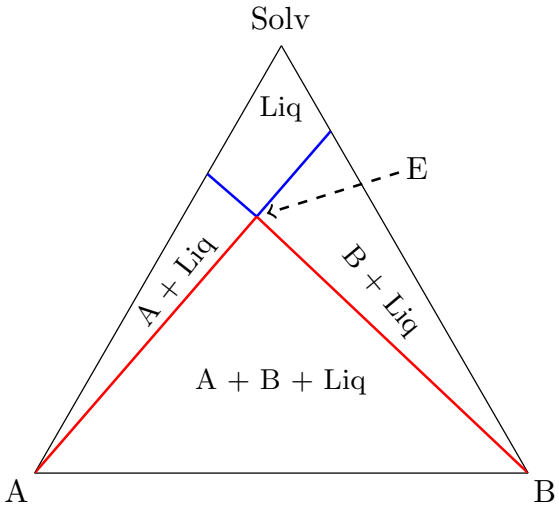

Figure 2.6: Ternary phase diagram of A and B in a solvent Solv at constant temperature. Blue: solubility lines; red: tie lines at eutectic composition bordering the bi- and triphasic regions; E: point of eutectic composition.

In this example, A and B exhibit a "salting-in" effect, which results in an increasing solubility of A and B in presence of the other component. Similarly to binary phase diagrams, several phase regions can be identified. Above the solubility lines (blue), the solution is undersaturated and therefore a one-phasic liquid ($P = 1$). Since three components are present ($N = 3$), Eq. (2.2) gives $F = 3$. These degrees of freedom are the temperature and the fractions of two of the components in the systems. Varying the fractions of two components yields the fraction of the remaining component following Eq. (2.3). Below the solubility lines, several regions containing solid as well as liquid phases can be found. Towards the edges, and therefore towards the pure components A and B, of the ternary phase diagram, pure A and B can be obtained by crystallization. Depending on the composition of the original solution and the supersaturation, the composition of the resulting liquid phase is determined. In this biphasic region, Eq. (2.2) yields $F = 2$, which are temperature and the fraction of one component in the system. These regions are limited by eutectic tie lines (red), which connect the pure solutes to the point of eutectic composition on the solubility lines and showcase the furthest tie line along which a single pure

solute crystallizes. Between these tie lines, a mixture of pure solid A and B crystallizes in equilibrium with a liquid phase of eutectic composition. Following, three phases are present at equilibrium conditions ($P = 3$), which yields one degree of freedom ($F = 1$) being the temperature since all compositions of the resulting liquid and solid phases are fixed as either pure or eutectic composition.
As an analogue to Figure 2.4, for a binary melt, Figure 2.7 shows the ternary phase diagram for a system including co-crystal formation.

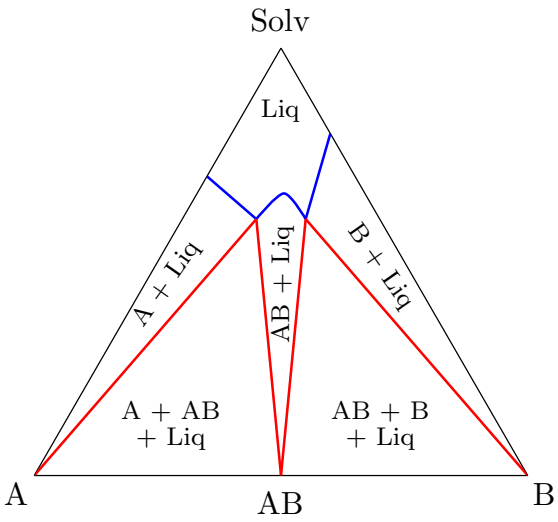

Figure 2.7: Ternary phase diagram of A and B in a solvent Solv including formation of co-crystal AB. Blue: solubility lines; red: tie lines at eutectic composition.

Similar to eutectic systems shown in Figure 2.6, a complete liquid phase is obtained for compositions above the solubility lines (blue). Pure solid A or B alongside their corresponding liquid phases are obtained towards the edges of the phase diagram. Analogously, the co-crystal AB is crystallized as a pure solid with an equilibrated liquid phase in the middle region of the diagram. In such ternary systems, a co-crystal results in two points of eutectic composition similar to binary systems (see Figure 2.4) and potentially a local solubility minimum. Comparable to the triphasic region in Figure 2.6, between the limiting tie lines (red), two pure solid phases crystallize along their tie lines and a liquid phase with eutectic composition.
If A and B exhibit solid phase miscibility, several phase behaviors are possible. In Figure 2.8, complete solid solutions with lyotropic (green) as well as alyotropic (blue) behavior are presented.

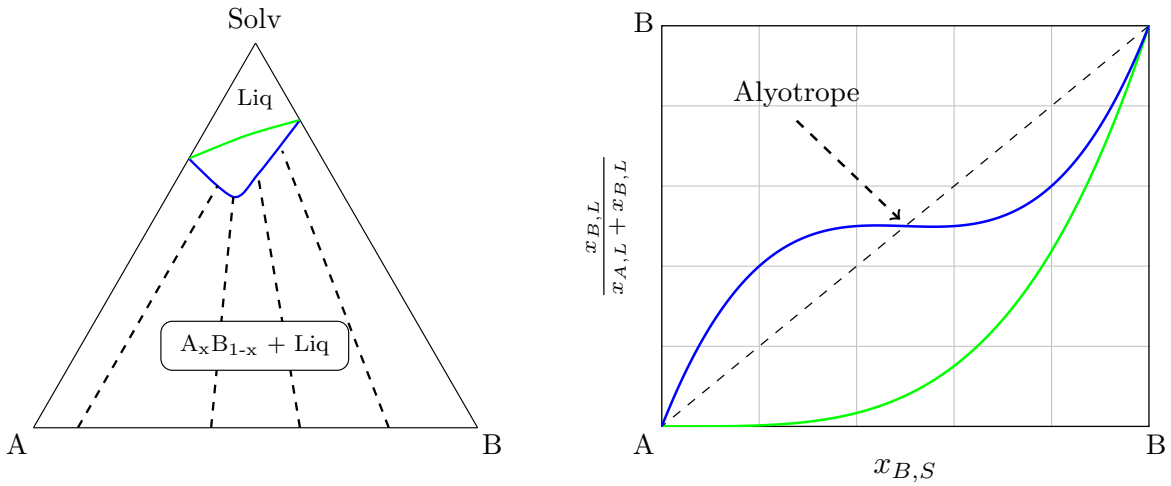

Figure 2.8: Left: ternary phase diagram of A and B in a solvent Solv. A and B exhibit full miscibility in the solid phase, forming A_xB_{1-x}. Right: corresponding distribution diagram. Green line: lyotropic behavior; blue line: solubility maximum alyotropic behavior; dashed black lines: tie lines connecting equilibrated liquid and solid phases (left) and 45° line (right).

Lyotropic solid solutions possess a continuous steady change in solubility between pure components, while alyotropic systems exhibit a discontinuity at a solubility maximum or minimum. At this extreme point, called alyotrope, the tie line is equal to the isopleth of a constant A to B ratio [29, 30]. Following, the compositions of the solids and the solutes in the liquid phase are equal and purification via crystallization is not possible at this point:

$$\frac{x_{B,L}}{x_{A,L}+x_{B,L}} = \frac{x_{B,S}}{x_{A,S}+x_{B,S}} = x_{B,S} \tag{2.7}$$

with $x_{A,S} + x_{B,S} = 1$ for a binary solid phase, following Eq. (2.3). As examples, potassium sulfate/ammonium sulfate/water [26] and L-valine /L-leucine /water [3, 28] mixtures exhibit complete miscibility in the solid phase with lyotropic and alyotropic behavior, respectively. The latter is investigated in detail in Chapter **3**.

Figure 2.8 (right) presents a distribution diagram of the behaviors shown in the ternary phase diagram (left). For systems involving solid solutions, plotting the solid against the solvent-free liquid fractions in such distribution diagrams is a helpful tool in designing crystallization processes [1, 13, 18, 26]. These distribution diagrams form the analogue to the well established $x - y$ distribution diagrams [27], used to describe vapor-liquid equilibria, where y_i and x_i are the vapor and liquid phase fractions of a component i. They can be used to graphically depict separation efficiencies by determining the distance between the equilibrium and 45° line (dashed black line). Further, the McCabe-Thiele

method can be utilized to determine the number of required theoretical separation stages for a given separation task [46]. Additionally, distribution diagrams offer a normalized depiction of tie lines in a ternary phase diagram. Due to the angled axis of ternary diagrams, comparing various tie lines to each other, especially when comparing multiple ternary phase diagrams, becomes non-trivial. The distribution diagram presents these tie lines as singular points in a two-dimensional plot, and thus, a straightforward comparison is possible. For crystallization of solid solutions, the component which is enriched in the solid and the liquid phase can be determined in the distribution diagram as well. For the lyotropic (green) system in Figure 2.8, component B is enriched in the solid phase, since the equilibrium line is below the 45° line which leads to an enrichment of A in the liquid phase. Systems with alyotropic behavior (blue) exhibit a crossing of the 45° line at the alyotrope, where Eq. (2.7) is valid. An alyotrope in a solid solution system behaves comparable to a homoazeotrope in vapor-liquid equilibria. Also, their depiction in their respective distribution diagrams is identical [18, 27]. Additionally, the enrichment of A and B in the respective phases is switched. Here, A is enriched in the solid phase on the A-rich and in the liquid phase on the B-rich side of the alyotrope. Generally, the component exhibiting lower solubility is enriched in the solid phase. Since the alyotrope in Figure 2.8 is a solubility maximum alyotrope, the alyotropic composition is always enriched in the liquid phase while A or B are enriched in the solid phase depending on the initial composition. The usage of distribution diagrams in the crystallization-based separation of solid solutions is shown in Chapter **4** of this work.

Apart from complete solid solutions, partial miscibility can occur in ternary systems. Figure 2.9 presents the ternary phase diagram and corresponding distribution diagram for such cases. Additionally, in the distribution diagram, obtained solid phases are denoted for each region. Here, the A- and B-rich solid solutions, α and β, can be crystallized along tie lines in the regions towards the edges of the ternary diagram. In these regions, tie lines connect specific liquid and solid compositions without crossing each other. For the distribution diagram, this yields the curved equilibrium lines shown in Figure 2.9 (right, designated with α and β), analogue to solid solution regions for complete miscibility (see Figure 2.8). The red lines in the ternary diagram depict limiting tie lines of these regions. It should be noted, that a specific tie line is a singular point on the equilibrium line in the distribution diagram. Therefore, the dashed red lines in Figure 2.9 are used to clarify the limitation while the actual tie line is located at the crossing of the equilibrium and the red dashed lines. In the miscibility gap, between the red lines, α and β crystallize along these limiting tie lines independently and a biphasic solid is formed. Each phase consists of its limiting composition α_{max} and β_{max}. Following this, the liquid phase, which is in equilibrium with both solid phases is located at the other end of the tie lines, at the solubility maximum, also referred to as double saturation point [19].

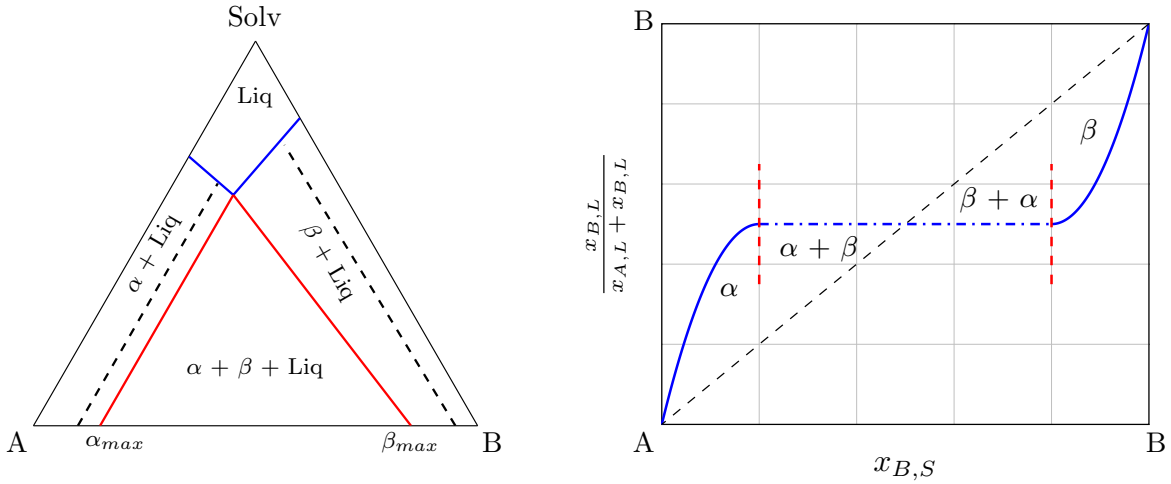

Figure 2.9: Left: ternary phase diagram of A and B in a solvent Solv. A and B exhibit partial miscibility in the solid phase, forming α and β as A- and B-rich solid solutions, respectively. Blue lines: solubility lines; red lines: limiting tie lines; dashed black lines: tie lines connecting equilibrated liquid and solid phases. Right: corresponding distribution diagram. Blue line: solid solution equilibrium line; blue dashdotted line: miscibility gap; black dashed line: 45° line.

Since the liquid phase composition is constant in the miscibility gap, regardless of the compositions of the solids, the distribution diagram depicts this region as a constant horizontal line (dashdotted blue line in Figure 2.9). On the isopleth of the solubility maximum, the solvent-free liquid and solid phases total composition are equal. Thus, the equilibrium line crosses the 45° line, limiting the purification similar to alyotropic behavior. However, no equilibrium tie lines are present in the miscibility gap. Therefore, this is distinctively different from alyotropic behavior even though its depiction in distribution diagrams is comparable. Crystallization in this region does not directly enrich the solid solution itself, but rather the ratio of α and β solid solutions. Partial solid state miscibility is the solid-liquid analogue to heteroazeotropes in vapor-liquid equilibria [18, 27], which similarly feature a miscibility gap in the liquid phase. Multiple systems exhibiting partial miscibility in the solid phase are reported in literature, e.g. in [18–20, 47, 48]. The partial solid solution system L-glutamic acid/L-asparitc acid is currently being investigated within our research group auxiliary to this work.

Comparable miscibility gaps are found in systems exhibiting solid solution behavior in presence of a co-crystal. E.g. this is observed in the L-valine /L-isoleucine system, forming a V_2I co-crystal [49, 50]. A representation of such behavior is shown in Figure 2.10. In systems exhibiting solid solutions as well as co-crystal formation, similar regions for pure α and β as A- and B-rich solid solutions are found. Also, miscibility gaps between these solid solutions and the co-crystal, here AB, are formed as depicted by the horizontal lines in the distribution diagram presented in Figure 2.10 (right).

Analogue to binary systems (see Figure 2.4), two points of eutectic composition are exhibited, each of which results in a crossing of the 45° line for each miscibility gap as explained previously for partial solid solutions.

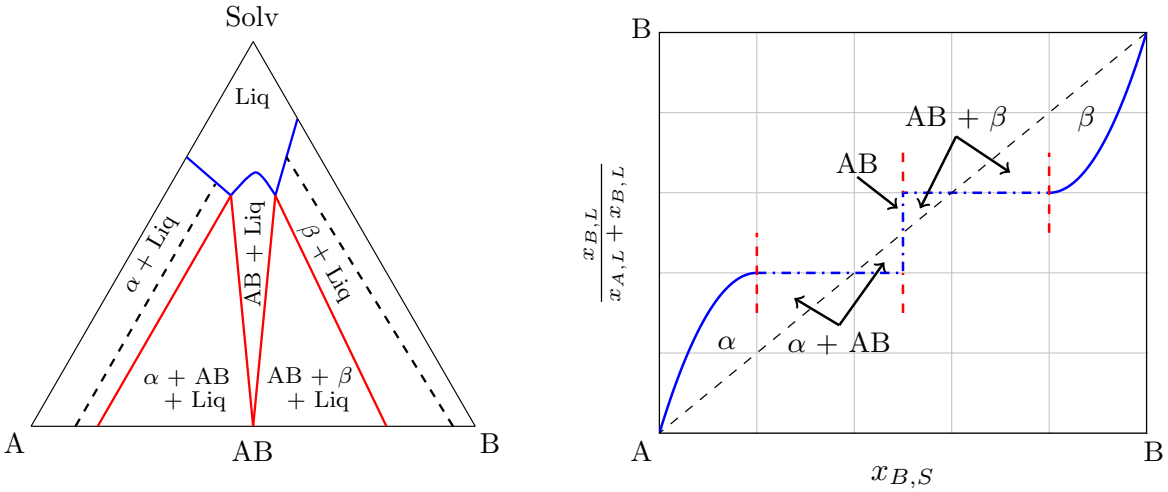

Figure 2.10: Left: ternary phase diagram of A and B in a solvent Solv including a distinct co-crystal AB. A and B exhibit partial miscibility in the solid phase, forming α and β as A- and B-rich solid solutions, respectively. Blue lines: solubility lines; red lines: limiting tie lines; dashed black lines: tie lines connecting equilibrated liquid and solid phases. Right: corresponding distribution diagram. Blue line: solid solution equilibrium line; blue dashdotted lines: miscibility gap (horizontal) and co-crystal (vertical); black dashed line: 45° line.

The co-crystal region in Figure 2.10, for a distinct co-crystal, behaves similarly to the co-crystal region in Figure 2.7. Here, a specific solid phase composition, that of the co-crystal, is in equilibrium with a range of liquid phase compositions. In the distribution diagram, this is depicted by a vertical line similar to how a miscibility gap is described by a horizontal line. Again, at the local solubility minimum of the co-crystal, the 45° is crossed. In total, this yields three crossings of the equilibrium and 45° line, each of which limits crystallization-based purification in the corresponding regions.
Alternatively, co-crystals in systems capable of forming solid solutions, may possess miscibility with present solid solutions. The behavior of partially miscible co-crystals is exemplified in Figure 2.11. Recently, in [51], the solid solution forming salicylic acid/antranilic acid system was investigated. It exhibits a 1:1 co-crystal miscible in the solid state at 55 °C, while forming a distinct non-miscible co-crystal at 25 °C. Miscibility in the solid state was also observed for the aforementioned V_2I co-crystal in the L-valine /L-isoleucine system [50]. Here, a solid solution based on the co-crystal AB is denoted as $\alpha\beta$. In such cases, the vertical line representing the distinct co-crystal in Figure 2.10, will not be a constant but rather a curved line, on which each solid possesses a corresponding liquid

phase composition. Following, in this region, $\alpha\beta$ crystallizes as a one-phasic solid along tie lines with an equilibrated liquid phase. This leads to a miscibility gap between the two solid solutions α or β with $\alpha\beta$, similar to distinct co-crystal formation in solid solution forming systems (see Figure 2.10).

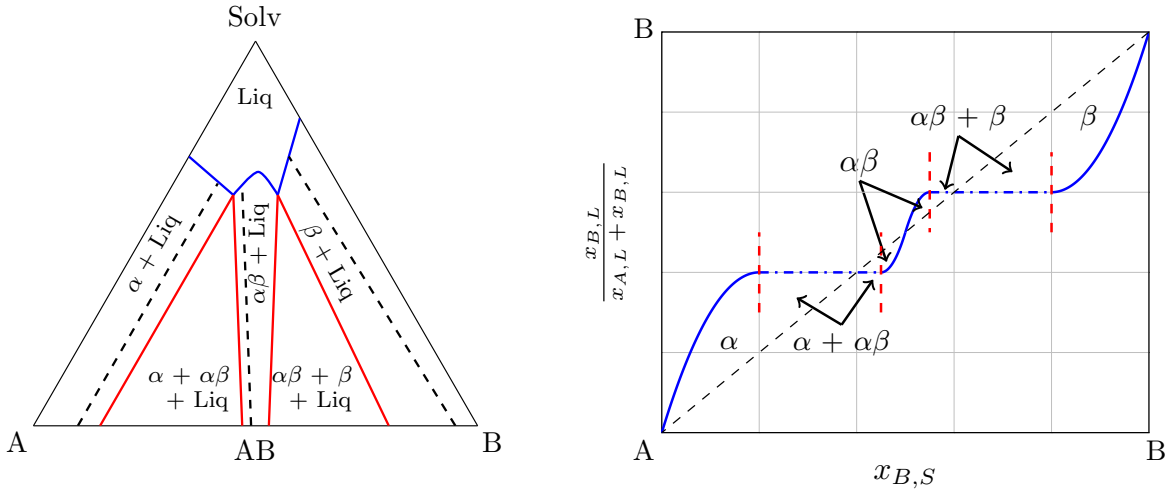

Figure 2.11: Left: ternary phase diagram of A and B in a solvent Solv including a partially miscible co-crystal AB. A and B exhibit partial miscibility in the solid phase, forming α and β as A- and B-rich solid solutions, respectively. $\alpha\beta$ denotes a solid solution based on AB. Blue lines: solubility lines; red lines: limiting tie lines; dashed black lines: tie lines connecting equilibrated liquid and solid phases. Right: corresponding distribution diagram. Blue line: solid solution equilibrium line; blue dashdotted line: miscibility gap; black dashed line: 45° line.

2.2 Thermodynamics of Solid-Liquid Equilibria

The thermodynamic equilibrium is defined as a stable state of one or multiple adjacent systems between which no interaction occurs without external influence. Following [52], this can be expressed as to following equations related to constant pressure p, temperature T, and chemical potential μ_i of component i for P number of phases.

$$p_{(1)} = p_{(2)} = \ldots = p_P \tag{2.8}$$

$$T_{(1)} = T_{(2)} = \ldots = T_P \tag{2.9}$$

$$\mu_{i,(1)} = \mu_{i,(2)} = \ldots = \mu_{i,P} \tag{2.10}$$

Specifically, for simple crystallization, where one liquid and one solid phase are in equilibrium, Eq. (2.10) yields:

$$\mu_{i,L} = \mu_{i,S} \tag{2.11}$$

The chemical potential μ is defined as the change of free Gibbs energy G per moles in a given system [53], and can be expressed as a function of the mixture fugacity $\hat{f}_i$ [52].

$$\mu_i = \left[\frac{\partial G}{\partial n_i}\right]_{p,T,n_j} = \mu_i^0 + RT \ln \frac{\hat{f}_i}{f_i^0} \tag{2.12}$$

Where $R = 8.314\ J\ K^{-1}\ mol^{-1}$ is the universal gas constant and μ_i^0 is the chemical potential at reference state. Fugacities describe a compounds potential to change its related system, e.g. from solid to liquid phase. Combining Eqs. (2.11) and (2.12) and simplifying for isothermal conditions, results in Eq. (2.13).

$$\hat{f}_{i,L} = \hat{f}_{i,S} \tag{2.13}$$

The mixture fugacity $\hat{f}$ can be expressed as a function of the molar fraction x, the activity coefficient γ, and the reference state fugacity f^0 of a pure component.

$$\hat{f}_i = f_i^0 x_i \gamma_i \tag{2.14}$$

The activity coefficient γ_i describes the deviation of a compound i from the ideal behavior in a mixture. Inserting this definition for both phases in Eq. (2.13), with $x_{i,S} = \gamma_{i,S} = 1$ for a pure solid, yields:

$$\frac{f_{i,S}^0}{f_{i,L}^0} = x_{i,L}\gamma_{i,L} \tag{2.15}$$

For systems capable of solid solution formation, the solid phase consists of multiple components. In such cases, Eq. (2.13) results in Eq. (2.16).

$$x_{i,S}\gamma_{i,S}\frac{f_{i,S}^0}{f_{i,L}^0} = x_{i,L}\gamma_{i,L} \tag{2.16}$$

Combining Eqs. (2.15) and (2.16) yields a relation capable of describing solid solution phase behavior [28]. For a system containing a binary *bin* solid solution and a corresponding ternary *ter* liquid phase (including solvent), this is given as follows:

$$x_{i,S}^{bin}\gamma_{i,S}^{bin} = \frac{x_{i,L}^{ter}\gamma_{i,L}^{ter}}{x_{i,L}^{bin}\gamma_{i,L}^{bin}} \tag{2.17}$$

Systems described by Eqs. (2.15) or (2.17), can be determined by their activities a. In [54], activity is defined as a dimensionless analogue to the concentration, with which the activity is equal if the systems behaves ideally. Here, the activity of the solutes in the liquid phase $a_{i,L}$ are equal to the fugacity ratio $\frac{f_{i,S}^0}{f_{i,L}^0}$ of pure solid and pure subcooled liquid. It can be expressed as a function of molar fraction x_i and activity coefficient γ_i [52].

$$\ln\left(\frac{f_{i,S}^0}{f_{i,L}^0}\right) = \ln\left(a_{i,L}\right) = \ln\left(x_{i,L}\gamma_{i,L}\right) \tag{2.18}$$

The activity of a pure solid can be calculated using its melting properties, such as melting temperature T_m and enthalpy of melting $\Delta H_m(T_m)$ [10, 55].

$$\ln\left(\frac{f_{i,S}^0}{f_{i,L}^0}\right) = -\frac{\Delta H_{m,i}(T_{m,i})}{RT}\left(1-\frac{T}{T_{m,i}}\right) - \frac{1}{RT}\int_{T_{m,i}}^{T}\Delta C_{p,m,i}(T)dT + \frac{1}{R}\int_{T_{m,i}}^{T}\frac{\Delta C_{p,m,i}(T)}{T}dT \tag{2.19}$$

In which, $\Delta C_{p,m}$ describes the molar melting heat capacity.
For given melting properties, using Eqs. (2.18) and (2.19) depending on the system at hand, the molar fraction of i in the liquid phase $x_{i,L}$, i.e. the solubility, can be calculated. However, for this, the activity coefficient γ needs to be determined. Many semi-empirical (NRTL [56], UNIQUAC [57], UNIFAC [58], etc.) and predictive models (SAFT [59], PC-SAFT [60, 61], etc.) for the calculation of activity coefficients are given in literature. This work utilizes PC-SAFT and NRTL models, which are further described in Sections **2.2.1** and **2.2.2**, respectively. Alternatively to the thermodynamic approach for solid-liquid equilibria description for solid solutions, an empirical model based solely on experimental data is proposed in Section **2.2.3**.

2.2.1 PC-SAFT: Perturbed-Chain Statistical Associating Fluid Theory

The PC-SAFT equation of state (EoS) is a model which combines the perturbation theory (see [62, 63]) with the SAFT EoS (see [59]). It portraits molecules in a system as chains of connected hard spheres with a given number of association sites. The PC-SAFT EoS is derived and explained in greater detail in [60, 61] for non-associating and associating systems, respectively. The interactions between chains of the same as well as different types can be described with a total of five component-specific parameters. Two of these parameters are only required for associating systems capable of forming hydrogen bonds. These parameters are number of hard spheres m in a given molecule, diameter of these spheres σ, dispersion interaction energy $\frac{u}{k}$, association energy $\frac{\varepsilon^{A_iB_i}}{k}$, and association volume $\kappa^{A_iB_i}$. Here, $k = 1.381 \cdot 10^{-23}\ J\ K^{-1}$ is the Boltzmann constant. Figure 2.12 illustrates a graphical representation of various interactions between identical and different molecules in the PC-SAFT EoS.

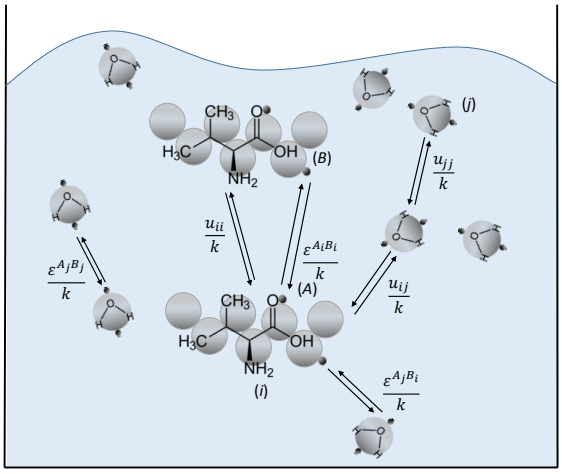

Figure 2.12: Graphical principle of PC-SAFT for the example of a L-valine (i) and water (j) solution. Dispersion $\frac{u}{k}$ and association $\frac{\varepsilon}{k}$ interactions are portrayed. Depiction inspired by [4].

As Figure 2.12 depicts, these interactions occur between molecules of the same type, as well as between different compounds. Additionally, the associating interaction takes the specific association sites A or B of the molecules into account. While for interactions between molecules of the same type the aforementioned parameters are used, interactions between different molecules are determined by the following mixing rules [60, 61].

$$\frac{u_{ij}}{k} = (1 - k_{ij}) \sqrt{\frac{u_i}{k} \frac{u_j}{k}} \tag{2.20}$$

$$\sigma_{ij} = \frac{1}{2} (\sigma_i + \sigma_j) \tag{2.21}$$

$$\frac{\varepsilon^{A_i B_j}}{k} = \frac{1}{2} \left(\frac{\varepsilon^{A_i B_i}}{k} + \frac{\varepsilon^{A_j B_j}}{k} \right) \tag{2.22}$$

$$\kappa^{A_i B_j} = \left(\frac{\sqrt{\sigma_i \sigma_j}}{\sigma_{ij}} \right)^3 \sqrt{\kappa^{A_i B_i} \kappa^{A_j B_j}} \tag{2.23}$$

Where k_{ij}, used in Eq. (2.20), is a correction parameter for the dispersion energy between two different molecules, thus, $k_{ij} = k_{ji}$ and $k_{ii} = k_{jj} = 0$ hold. Pure component parameters as well as k_{ij} are fitted to experimental data sets such as solubilities, densities etc.. Typically, k_{ij} is given as a function of temperature [64].

$$k_{ij} = k_{ij,T_0} + k_{ij,T} \cdot (T - T_0) \tag{2.24}$$

Where T_0 is a reference temperature, which depending on the source citation is usually 0 K or 298.15 K. However, k_{ij} can be set to zero to investigate the models capability to distinguish between different solvents based solely on pure component parameters, predictively.
Among other things, PC-SAFT can be used to calculate the compressibility factor Z. It describes the deviation from ideal and real behavior and is defined as follows.

$$Z = \frac{pv}{RT} \tag{2.25}$$

Where v is the molar volume. Here, the compressibility factor is determined as the sum of ideal gas $Z^{id} = 1$, hard-chain Z^{hc}, perturbation Z^{disp}, and association Z^{assoc} contributions.

$$Z = Z^{id} + Z^{hc} + Z^{disp} + Z^{assoc} \tag{2.26}$$

Equations for these contributions are given in [60] for Z^{hc} and Z^{disp} and in [59] for Z^{assoc}. Calculations of the various contributions of the compressibility factor are listed in Appendix A.1.
Using the compressibility factor, fugacity coefficients φ_i can be calculated.

$$\ln(\varphi_i) = \frac{\mu_i^{res}}{kT} - \ln(Z) \tag{2.27}$$

The calculation of the residual chemical potential is given in [60] and is listed in Appendix A.1.4. The activity coefficient γ_i is defined as the ratio of its fugacity f_i to its ideal state fugacity f_i^{id} [53]. To obtain γ_i as a function of φ_i, this can be rearranged as follows:

$$\gamma_i = \frac{f_i}{f_i^{id}} = \frac{f_i}{f_i^0 x_i} = \frac{f_i p}{f_i^0 x_i p} = \frac{\varphi_i}{\varphi_i^0} \tag{2.28}$$

with $\varphi_i = \dfrac{f_i}{p_i}$, which equals 1 for an ideal gas.

2.2.2 NRTL: Non-Random Two-Liquid Model

The NRTL model [56], is a semi-empirical model designed to calculate activity coefficients of mixtures as a function of temperature. For binary mixtures consisting of A and B, the model is given in [53].

$$\ln(\gamma_A) = x_B^2 \left[\tau_{AB} \left(\frac{G_{AB}}{x_B + x_A G_{AB}} \right)^2 + \frac{G_{BA}\tau_{BA}}{(x_A + x_B G_{BA})^2} \right] \tag{2.29}$$

$$\ln(\gamma_B) = x_A^2 \left[\tau_{BA} \left(\frac{G_{BA}}{x_A + x_B G_{BA}} \right)^2 + \frac{G_{AB}\tau_{AB}}{(x_B + x_A G_{AB})^2} \right] \tag{2.30}$$

Where G_{AB} and τ_{AB} are dimensionless interaction parameters, which are defined as follows:

$$G_{AB} = \exp(-\alpha\tau_{AB}) \tag{2.31}$$

$$G_{BA} = \exp(-\alpha\tau_{BA}) \tag{2.32}$$

$$\tau_{AB} = \frac{b_{AB}}{RT} \tag{2.33}$$

$$\tau_{BA} = \frac{b_{BA}}{RT} \tag{2.34}$$

Here, α, b_{AB}, and b_{BA} are the non-randomness parameter and adjustable interaction parameters, respectively. These temperature independent parameters are fitted to experimental phase equilibria data sets such as solubilities.

2.2.3 Empirical Solid-Liquid Equilibria Modeling

Alternatively to predictive and semi-predictive description of solid-liquid equilibria, empirical models are derived in this section. These models are solely based on experimental data sets and its parameters are directly fitted as such.
In [23], an empirical equilibrium model for complete solid solutions was initially proposed. This model is based on normalizing the three coordinates of the ternary phase diagram into Cartesian x-y coordinates. Two functions, P and Q, were defined to describe the saturated liquid and solid phase compositions, respectively.

$$P(x,y) = \begin{pmatrix} x \\ y = a(x) \end{pmatrix} \tag{2.35}$$

$$Q(x,y) = \begin{pmatrix} b^*(x,b) \\ y = 0 \end{pmatrix} \tag{2.36}$$

For the liquid phase P, the value of y can be described as a function a of x. The solid phase Q and the slopes of the tie lines are described by a function b^*, which depends on the composition of the solid phase x and another empirical function $b(x)$. Since, the solid phase does not include any solvent, $y = 0$ holds. Here, $a(x)$ and $b(x)$ are given as simple polynomials, while b^* is given in Eq. (2.38).

$$a(x) = \sum_{m=0}^{M_a} a_M x^M \tag{2.37}$$

$$b^*(x) = x_{A,S} + b(x)(x_{B,S} - x_{A,S}) \tag{2.38}$$

$$b(x) = \sum_{m=0}^{M_b} b_M x^M \tag{2.39}$$

The parameters a_M and b_M are fitted to experimental data sets. While this model is capable of describing the solid-liquid equilibria of complete solid solutions quite accurately, it suffers from unnecessary complexity for an empirical model.
An alternative simplified model was proposed in [26]. Here, the liquid phase molar fraction $x_{i,L}$ is directly calculated as an empirical function of the solid phase $x_{i,S}$. Again, polynomials are used to describe the trend of the tie lines. The molar fraction of the solvent $x_{Solv,L}$ is calculated by Eq. (2.3), while $x_{Solv,S} = 0$ holds, assuming no solvent is present in the solid phase.

$$\begin{pmatrix} x_{A,L} \\ x_{B,L} \\ x_{Solv,L} \end{pmatrix} = \begin{pmatrix} \sum_{m=1}^{M_A} a_m x_{A,S}^m \\ \sum_{m=1}^{M_B} b_m x_{B,S}^m \\ 1 - x_{A,L} - x_{B,L} \end{pmatrix} \tag{2.40}$$

This approach simplifies the empirical model, since the conversion to Cartesian coordinates is avoided. Since two sets of parameters are needed for both approaches, the number of parameters stays the same regardless of the chosen model. This model showed accurate results for various complete solid solution systems [1, 26]. However, it is limited to a single solvent or a constant composition of a solvent mixture for which experimental data is available.

During this work, this model was extended to be applicable for various solvent mixtures without requiring experimental data for all solvent compositions, and was firstly published in [1]. Here, its main use is the description of crystallization behavior of solid solutions in solvent/antisolvent mixtures. For this, the antisolvent factor ζ is defined as follows:

$$\zeta = \frac{n_{Anti}}{n_{Solv}} = \frac{x_{Anti}}{x_{Solv}} \tag{2.41}$$

Where n_{Anti} and n_{Solv} are the molar amounts of the antisolvent and solvent of a given mixture, respectively. Since the system, this work focuses on, exhibits an exponential solubility decrease with increasing antisolvent fraction (see Chapter **3**), an exponential function was chosen to include ζ into Eq. (2.40). This results in Eq. (2.42), in which $a_{m,1}$ and $b_{m,1}$ are fitted to data sets for pure solvent $\zeta = 0$, while $a_{m,2}$ and $b_{m,2}$ are fitted to solubility data obtained from mixed solvents with $\zeta \neq 0$. It should be noted, that $\hat{x}_{Solv,L} = x_{Solv,L} + x_{Anti,L}$ describes the total solvent phase of the solvent/antisolvent mixture.

$$\begin{pmatrix} x_{A,L} \\ x_{B,L} \\ \hat{x}_{Solv,L} \end{pmatrix} = \begin{pmatrix} \sum_{m=1}^{M_A} a_{m,1} \cdot \exp\left(a_{m,2} \cdot \zeta\right) x_{A,S}^m \\ \sum_{m=1}^{M_B} b_{m,1} \cdot \exp\left(b_{m,2} \cdot \zeta\right) x_{B,S}^m \\ 1 - x_{A,L} - x_{B,L} \end{pmatrix} \tag{2.42}$$

Example calculations of Eq. (2.42) and its comparison to experimental data sets are given in Section **3.3** of this work.

2.3 Summary

This initial chapter gives the theoretical and fundamental basis required to develop the ideas and approaches discussed in this dissertation. While cited sources provide more detailed insight into the discussed topics, a broader general overview should be obtained within this chapter. At first, crystallization itself was defined and various crystallization strategies employed in this work were introduced. Besides classical evaporative and cooling crystallization, antisolvent crystallization was exemplified. This aspect will be utilized in greater detail in solid-liquid equilibria determination in Chapter **3** and in the solid solution separation via counter-current crystallization described in Chapter **4**.
Further, various binary and ternary phase diagrams were discussed in Sections **2.1.1** and **2.1.2** to provide a basic understanding of solid-liquid phase behavior. Especially, for solid solutions in ternary systems, this is discussed in greater detail. In particular, the application of distribution diagrams for challenging solid solution forming systems is developed. The corresponding phase diagrams are utilized throughout this thesis to illustrate the complex phase behavior in a comprehensive manner.
Lastly, Section **2.2** introduces basic thermodynamic relations and (semi-)predictive models for the calculation of solid-liquid equilibria and corresponding activity coefficients, respectively. These models will be applied in Section **3.4** to predict solid-liquid equilibria of continuous solid solutions in various L-valine /L-leucine /water/antisolvent systems. As an alternative to the (semi-)predictive approach, an empirical model was extended in Section **2.2.3** to quantify solvent/antisolvent mixtures. The model's accuracy will be validated in Section **3.3** and subsequently utilized in a predictive process simulation of the counter-current crystallization process (see Section **4.2**).

3. Solid-Liquid Equilibria Investigation of Solid Solutions

3.1 Chemicals

Results of investigating the solid-liquid equilibria of specific solid solutions are given in this chapter. As an exemplary system, the amino acids L-valine and L-leucine were chosen, since they have been shown to exhibit full miscibility in the solid state when crystallized from aqueous solutions [28, 65]. Additionally, many studies including these amino acids, e.g. [66–79] among others, focused on (pseudo-)binary solubility studies in various solvents and solvent mixtures. One additional study investigated and modeled mixtures of L-valine and L-leucine , however, the formation of solid solutions was neglected [80]. Figure 3.1 shows the chemical structures of L-valine and L-leucine .

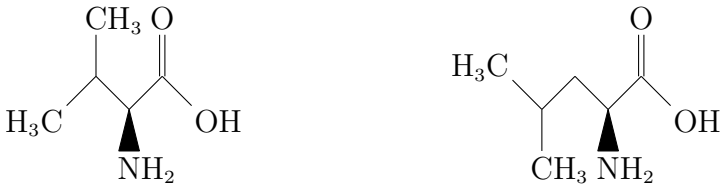

Figure 3.1: Chemical structures of L-valine (left) and L-leucine (right).

Prior to this work, solubilities and their corresponding tie lines of L-valine /L-leucine solid solutions of varying composition in water at 25 and 40 $°C$ were measured within the research group. These measurements are listed in Table A.2 and A.4, and agree well with available literature data from [28] for 25 $°C$. Data sets, determined at 25 °C, are published in [3], while data at 40 °C is not yet published at the time of writing. Our data, as well as literature data, indicated a solubility maximum alyotrope (see Figure 2.8) in this system. In addition to this, in [31], a co-crystal, abbreviated V_3L, consisting of three parts L-valine and one part L-leucine was found. However, this co-crystal was not reported in earlier solubility studies of this system. During investigations of this work, the solubility measurements were extended for various water/solvent mixtures and the manufacturing and stability of V_3L were investigated. Ethanol, isopropanol, and acetone were chosen as model antisolvents based on several factors such as handleability, toxicity, relative polarity, lower boiling temperature as water for easy recycling, etc.. In the following, the chemicals, measurement and analytical procedures as well as the resulting solid-liquid equilibria are

discussed in greater detail.
As solutes, the amino acids L-valine and L-leucine were both acquired from Iris Biotech GmbH with a purity of 98.8 % and 100.3 % relative to their assay reference, respectively. Copper(II) sulfate pentahydrate ($CuSO_4 \cdot 5H_2O$), used in HPLC measurements, was supplied by Merck KGaA. Solvents, apart form water, were supplied by VWR International in HPLC grade purity. Water used in experiments, was deionized via a Millipore40 filter (resistivity: 18.2 MΩ cm, total organic carbon (TOC): 3 ppb). All other chemicals were used as received without further purification. Additional information on these compounds are listed in Table 3.1.

Table 3.1: Chemicals used in this work. Purities and molar masses given by supplier. *: relative to reference purity.

Compound	CAS	Purity	Supplier	$M\,[g\,mol^{-1}]$
L-Valine	72-18-4	98.8 %*	Iris Biotech GmbH	117.15
L-Leucine	61-90-5	100.3 %*	Iris Biotech GmbH	131.17
$CuSO_4 \cdot 5H_2O$	7758-99-8	≥99.0 %*	Merck KGaA	249.68
Ethanol	64-17-5	>99.7 %	VWR International	46.07
Isopropanol	67-63-0	>99.8 %	VWR International	60.10
Acetone	67-64-1	>99.8 %	VWR International	58.08
Methanol	67-55-1	>99.9 %	VWR International	32.04

Further, additional data sets of the amino acids and selected solvents are given in Appendix A.3. Theses include parameters for several thermodynamic models as well as melting data obtained via fast scanning calorimetry (FSC) in [64]. FSC was used, due to thermal decomposition of these amino acids during conventional differential scanning calorimetry (DSC) measurements.

3.2 Solubility Determination

3.2.1 Experimental Procedures

Experimental procedures for the measurement of solubilities and crystallization behavior of the amino acids in water/antisolvent mixtures are explained in this section. Measurement procedures for solubilities in water, based on evaporative crystallization, measured in prior studies are explained in [3].
For solubility determinations in water/antisolvent mixtures, several compositions with varying L-valine and L-leucine ratios were given into enough deionized water of a known amount to be slightly undersaturated, sealed, and completely dissolved at elevated temperature. Complete dissolution is required to enable total recrystallization as solid solutions.

In these experiments, the amount of water used was $\sim 8\,mL$. When complete dissolution was achieved, the vials were left to cool down to ambient temperature, after which, the vials were opened and a specific amount of antisolvent was added, which initializes nucleation of crystals. The amount of added antisolvent was adjusted to keep a constant ζ (see Eq. (2.41)) in all samples of the measurement. The vials were resealed, including a magnetic stirrer, and were stirred at a desired temperature, controlled via thermostat, for at least 72 h to achieve equilibration. During this equilibration, the vials were manually shaken twice a day to lessen the impact of flotation observed within this system. The vials were weighted before and after the equilibration period to ensure no evaporation of antisolvent occurred.
Once equilibrium was reached, a few droplets of the liquid phase were sampled with a syringe and syringe filter (pore size: 0.45 µm), their weight recorded, and diluted in eluent for HPLC analysis (see Section **3.2.2**). Afterwards, the remaining suspension was separated via vacuum filtration (pore size: 10-16 µm). The liquid phase was discarded, while the solid phase was sampled, dried, and analyzed by PXRD as well as dissolved into eluent for HPLC analysis.

3.2.2 Analytical Methods

The main analytical methods, used in this work, are HPLC and PXRD, which are explained in the following sections. Usually, thermal methods like differential scanning calorimetry (DSC) are utilized as well, to understand phase behavior regarding crystallization processes. However, L-valine and L-leucine decompose before reaching their respective melting temperature. Thus, to acquire insight on their melting properties, more elaborate measurements, such as fast scanning calorimetry (FSC), are required [64]. Additional information and uses of such melting data are described in Section **3.4**.

High Performance Liquid Chromatography

In quantitative analysis of samples, HPLC is a powerful tool. It provides fast and accurate composition measurements. Its main purpose is the separation of various components in a given sample and to quantify each relevant component using a pre-calibrated detector. For the separation, a chromatography column is used as a stationary phase, consisting of tightly packed absorbent. The mobile phase, consisting of liquid eluent, is pumped through the column continuously. A small sample amount is injected into the eluent stream prior to the column and therefore flows through the column. Inside, different compounds interact differently with the stationary phase, which influences their individual residence times until the end of the column is reached. These interaction can be based on chemical bonds, size, charge, etc.. Following, increasing the length of the separation column leads to longer residence times and improved separation. After the separation column, a detector (i.e. IR,

UV, MS, ...) is used to quantify each component separately. The detector is calibrated with samples of known composition.
A Thermo Fischer Scientific Dionex UltiMate 3000 HPLC was used in this work. It was equipped with a Phenomenex Chirex® 3126 (D)-penicillamine column (particle size: 5 μm; pore size: 110 Å) at 25 °C and an UV-based diode array detector (DAD) operating at a wavelength of $\lambda = 280$ nm. As eluent, a 90:10 vol.% mixture of aqueous 2 mmol $CuSO_4$ solution and methanol was utilized. For all samples not containing acetone, a shorter column (length: 50 mm, diameter: 4.6 mm, referred to as short column) was chosen due to sufficient separation and short measurement duration. An example measurement, with this column, is shown in Figure 3.2. A continuous eluent flow rate of 0.5 mL min^{-1} and a sample injection volume of 3 µL were used for this column. In Figure 3.2, the absorbance A of the liquid (at $\lambda = 280$ nm) is plotted over the residence time t. Here, the absorbance is normalized to the UV absorption by the eluent. Due to UV-active compounds in the sample, the absorbance increases if a specific compound enters the detector. By integrating the resulting peak, the peak area A_P, between peak and base line, can be determined. It is proportional to the compounds quantity. Negative absorbances can be explained by pressure increases due to the sample injection into the eluent stream.

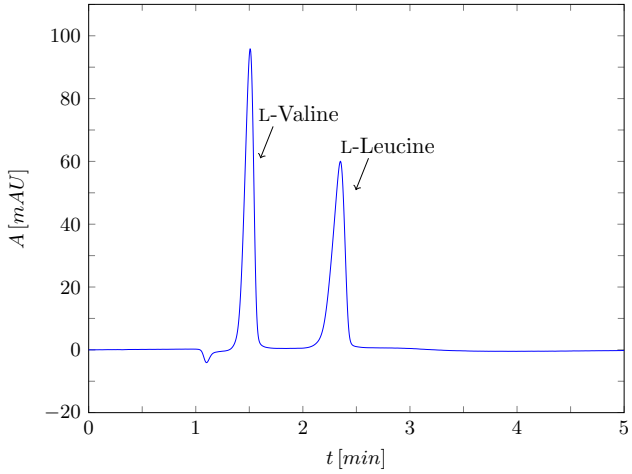

Figure 3.2: Chromatogram of an exemplified HPLC measurement of an aqueous L-valine / L-leucine solution using the short column.

Since acetone is an UV-active compound, an additional specific peak is observed in samples containing acetone (see Figure 3.3). To achieve sufficient separation and avoid overlapping of distinct peaks, an identical but longer version of the column (length: 250 mm, diameter: 4.6 mm, referred to as long column) was utilized. It was used with an eluent flow rate of 0.5 mL min^{-1} and a sample injection volume of 30 µL. During the separation and measurement the columns are kept at 25 °C.

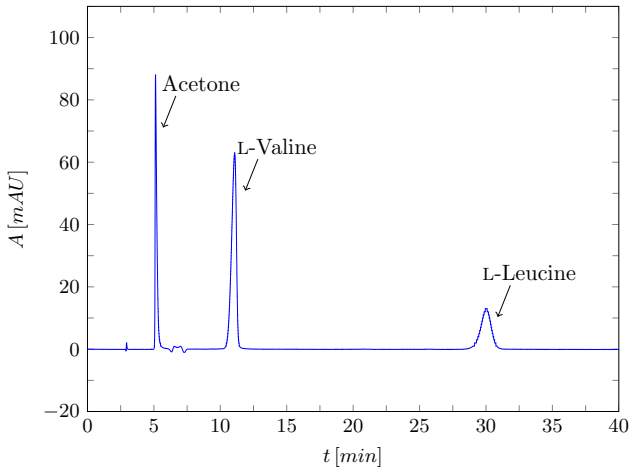

Figure 3.3: Chromatogram of an exemplified HPLC measurement of an aqueous L-valine /L-leucine /acetone solution using the long column.

To relate the obtained areas to actual quantities inside the sample, the detector was calibrated using at least five samples with known composition; here, weight fractions w_i of L-valine and L-leucine . These calibration samples were injected into the HPLC with the same injection volume depending on the column used. After the column was exchanged or an extended amount of time between measurements passed, a new calibration was prepared. Otherwise, a single known sample was measured to verify the validity of the current calibration. Figure 3.4 presents an example calibration for L-valine and L-leucine .

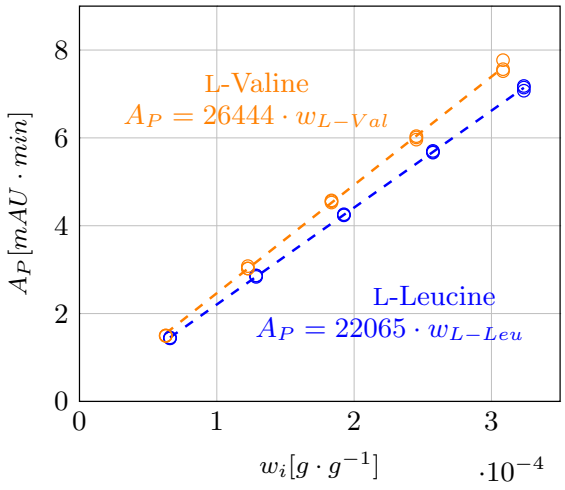

Figure 3.4: Exemplified calibration lines of HPLC measurements of various L-valine /L-leucine solutions. Orange: L-valine ; blue: L-leucine ; o: experimental data; dashed line: linear regression.

As seen in Figure 3.4, the calibration samples were measured in triplicate, which was also done for samples with unknown composition. The calibration measurements can be

described by a linear regressed line with an y-axis intersection of 0. Following, the slope of the calibration line, the calibration factor F_c, can be determined by linear regression with Eq. (3.1).

$$F_{c,i} = \frac{\overline{A}_{P,i}}{w_i} \tag{3.1}$$

$$\overline{A}_{P,i} = \frac{\sum_{k=1}^{K} A_{P,i,k}}{K} \tag{3.2}$$

Where K is number of repeated experiments, here $K = 3$.
If a sample with unknown composition is measured and peak area determined, its mass fraction $w_{i,Spl}$ can be calculated using the Eq. (3.3). If the unknown sample is of higher concentration than the calibration is valid for, the sample may be diluted with eluent. This is described by a dilution factor F_d, using the mass of the sample m_{Spl} and the mass of additional eluent m_{Elu}.

$$w_{i,Spl} = \frac{A_{P,i}}{F_{c,i} F_d} \tag{3.3}$$

$$F_d = \frac{m_{Spl}}{m_{Spl} + m_{Elu}} \tag{3.4}$$

Weight fractions w_i determined by HPLC measurements can be converted to molar fractions x_i using Eq. (3.5) [81].

$$x_i = \frac{\frac{w_i}{M_i}}{\sum_{n=1}^{N} \left(\frac{w_n}{M_n} \right)} \tag{3.5}$$

To acquire statistical relevance of repeated measurements, statistical methods are used. In this work, the population standard deviation σ and standard uncertainty U are determined following [82]. Population standard deviation σ is calculated using the mean (analogue to Eq. (3.2)) within Eq. (3.6).

$$\sigma(x) = \sqrt{\sum_{k=1}^{K} \frac{(x_k - \overline{x})^2}{K}} \tag{3.6}$$

From the population standard deviation σ, standard uncertainty U is calculated using the

confidence factor Z_c for a specific level of confidence. This gives a probability of correctly assuming that the true value is within the specified range. Thus, the higher the probability level, the higher value of Z_c is acquired, which leads to a larger standard uncertainty range (see Eq. (3.7)). This work used a confidence level of 95 %, therefore $Z_c = 1.96$ [82].

$$U(x) = \frac{\sigma(x) Z_c}{\sqrt{K}} \tag{3.7}$$

Powder X-Ray Diffraction

PXRD measurements give qualitative information about the crystal structure of a given solid sample via X-ray radiation [83]. The reflection of the radiation beam by the solid sample can be quantified by Bragg's law.

$$n_I \lambda = 2d \sin(\Theta) \tag{3.8}$$

Where n_I, d, and Θ are the order of interference, layer spacing, and angle of interference, respectively. A simplified scheme of Bragg's law is presented in Figure 3.5.

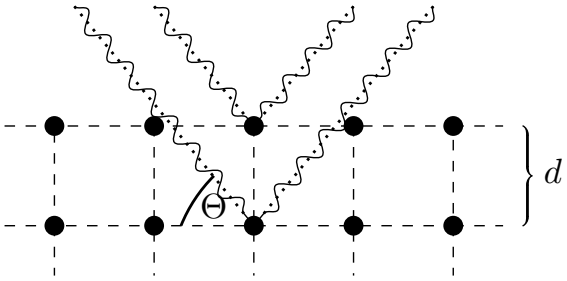

Figure 3.5: Schematic representation of Bragg's law. Dashed lines and dots: repeating crystal structure; wavy lines: X-ray radiation; Θ: angle of interference; d: layer spacing. According to [83].

In PXRD measurement, several angles Θ are radiated for a set time and its reflections measured by a detector opposite to the X-razy tube. Due to a sample in the measurement, interferences to the reflection are introduced depending on the solid's crystal structure. For these, a diffraction pattern, the diffractogram, can be obtained, which is unique to each crystal structure (see Figure 3.6). This is used in the qualitative analysis of a given solid sample, i.e. for polymorph or residual compound detection.

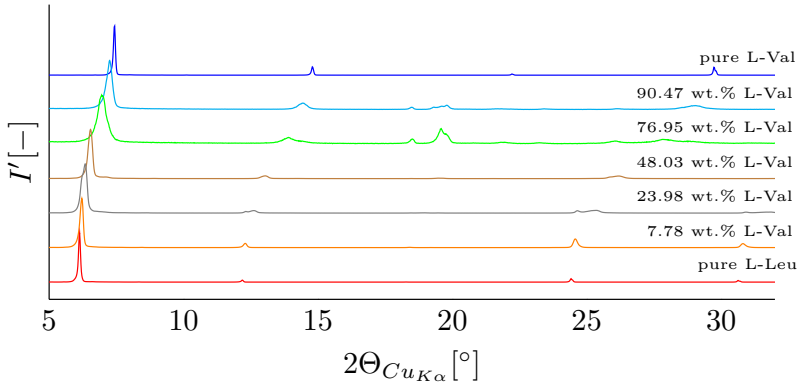

Figure 3.6: PXRD patterns of various L-valine and L-leucine mixtures obtained from aqueous solution via evaporative crystallization and subsequent equilibration at 25 °C. Published in [3].

Figure 3.6 depicts several PXRD patterns of various L-valine /L-leucine solid solutions acquired from aqueous solution [3]. To allow for better comparability between different measurements, these patterns were normalized to their highest intensity value $I'_{max} = 1$ following Eq. (3.9).

$$I' = \frac{I - I_{min}}{I_{max} - I_{min}} \quad [0, \ldots, 1] \tag{3.9}$$

In this work, the solid phase was dried overnight in a vacuum oven, at 200 mbar and 40 °C, before its measurement via PXRD. The dried samples were measured using a PANanlytical X'Pert Pro diffractometer with $Cu_{K\alpha}$ radiation. Measurements were conducted from 5 to 32° with a step size of 0.0167°, in which each step was scanned for 200 s.
In the following, an brief example analysis of Figure 3.6 is given to clarify the interpretation of various PXRD patterns during this work. Here, pure component diffraction patterns of L-valine and L-leucine are shown at the top (blue) and bottom (red), respectively. Since both compounds possess similar lattice parameters of the monoclinic cell, they crystallize in similar crystal lattices and exhibit comparable PXRD patterns [31]. L-valine and L-leucine possess multiple characteristic peaks at 6 and 7.5°, 12 and 15°, and 24 and 30°, respectively. For mechanical mixtures of these components, i.e. no molecular mixing in the solid phase, all of these characteristic peaks are visible in one PXRD pattern. This indicates biphasic behavior, since two pure component phases can be observed. On the other hand, if solid solutions were formed, only one peak in between each the characteristic peaks is detected. Hereby, its location is depending on the ratio of L-valine and L-leucine in the sample. This results in the gradual shifts of the characteristic peaks with changing composition, as it can be seen e.g. in Figure 3.6. Following this, PXRD measurements in this work were predominately used to validate solid solution formation. In some

samples, i.e. 76.95 and 90.47 *wt.*% L-valine , a second phase can be observed at around 19.5°. This can be attributed to the formation of a V_3L co-crystal [31]. This co-crystal is investigated further in Section **3.5**.

3.3 Solubility Studies in Solvent/Antisolvent Systems

The previous sections discussed the experimental procedures and analytical methods. In this section, the results of the solid-liquid equilibria investigations of L-valine /L-leucine solid solution systems are shown. As mentioned previously, solubility data at 25 and 40 °C in water were measured by M.Sc. S. Münzberg prior to this work (see Figure 3.7). This work extends theses data sets with solubility measurements of various water/antisolvent mixtures, again at 25 and 40 °C. Ethanol, isopropanol, and acetone were chosen as exemplary antisolvents. All data sets of the measured liquid and solid phase compositions as well as corresponding PXRD diagrams are given in Appendix A.2, partly published in [1–3], and are indicated accordingly. Additionally, parameters fitted to empirical polynomial models, described in Section **2.2.3** as Eqs. (2.40) and (2.42), are given in Appendix A.2 as well. These models and their parameters are used alongside experimental data to highlight various solid-liquid behaviors. Figure 3.7 presents the solubilities of L-valine /L-leucine solid solutions in water at 25 and 40 °C.

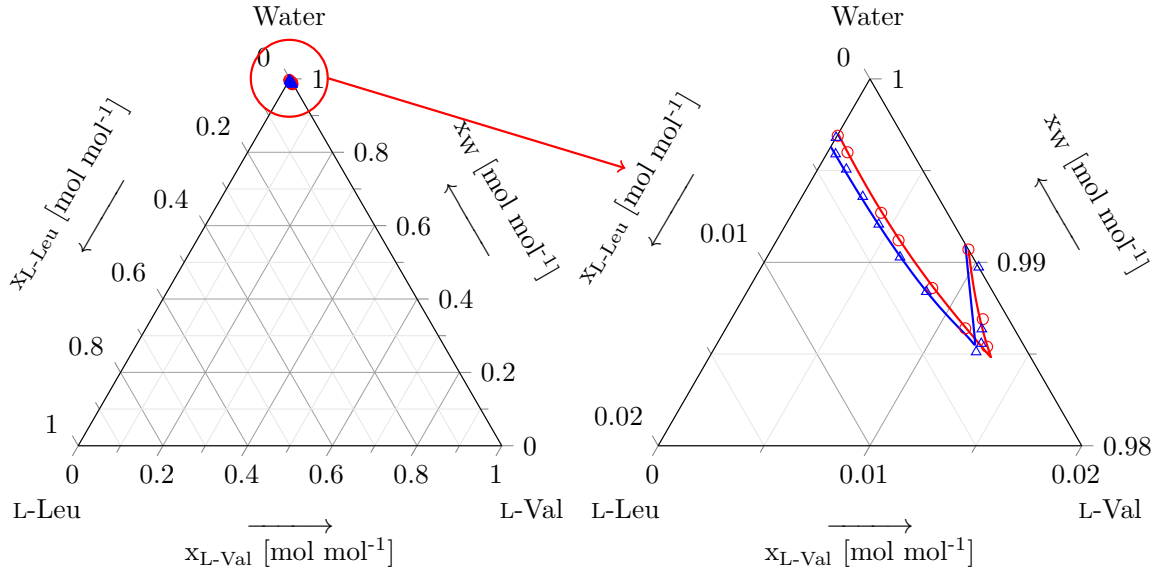

Figure 3.7: Ternary phase diagram of L-valine and L-leucine in water at 25 (o, red) and 40 °C (△, blue). Dots: experimental data; solid lines: calculated using Eq. (2.40). Right: zoomed view of the ternary phase diagram. Partly published in [3].

As shown in Figure 3.7, the overall solubility of L-valine and L-leucine in water is relatively small (<1.5 mol%). L-Valine exhibits a roughly 2 to 2.5 times higher solubility as

L-leucine at the regarded temperatures. At 40 °C, both amino acids show slightly higher solubility values when compared to 25 °C. However, the overall dependency of the solubility on temperature is low for both pure solutes and their mixtures. The aqueous L-valine /L-leucine system shows solubility maximum alyotropic behavior (see Figure 2.8) for all measured temperatures. The solubility maximum is located at molar ratios of ∼ 88/12 and ∼ 84/16 L-valine /L-leucine at 25 and 40 °C, respectively. As observable in Figure 3.7, the polynomial model given as Eq. (2.40) is able to portrait the solubilities of these solid solutions with great accuracy. However, small deviations can be seen for pure L-leucine and in L-valine rich regions at 40 °C.

The distribution diagram (see Figure 3.8) illustrates the tie line behaviors of the data sets portrayed in Figure 3.7 in a two-dimensional manner. The polynomial model (see Eq. (2.40)) is again able to replicate measured data sets and alyotropic behaviors well. As discussed in more detail in Section **2.1.2**, a greater area between equilibrium and 45° lines in the distribution diagram gives a greater slope of a specific tie line in the ternary phase diagram and with it a better separation via crystallization along this tie line. At 25 °C, when compared to 40 °C, an increased area is observed on the L-leucine side of the alyotrope. On the L-valine side, this phenomenon is reversed, due to the shift in alyotropic composition.

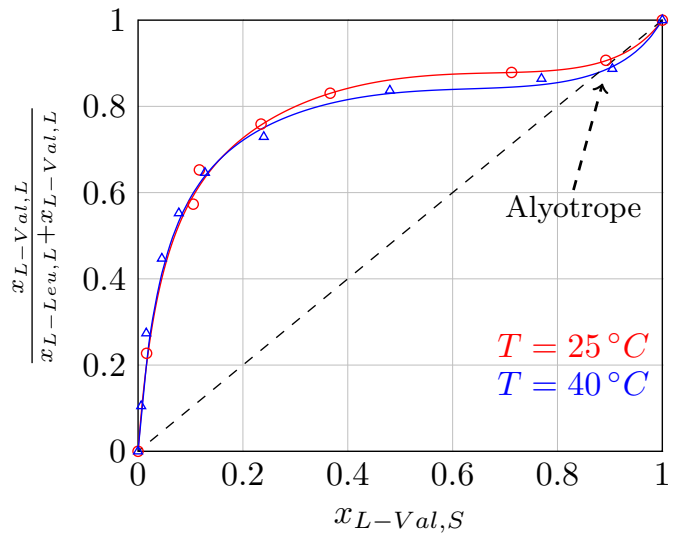

Figure 3.8: Distribution diagram of L-valine and L-leucine in water at 25 (o, red) and 40 °C (△, blue). Dots: experimental data; solid lines: calculated using Eq. (2.40). Dashed line: 45° line. Partly published in [3].

It should be noted, that in theory, the alyotrope is located perfectly at the solubility maximum. However, the distribution diagram (see Figure 3.8) shows the crossing of the 45° line at molar ratios of ∼ 90/10 and ∼ 88/12 L-valine /L-leucine , at 25 and 40 °C, according to Eq. (2.40). This deviation, between the solubility maximum and the definition

of alyotropes given in Eq. (2.7) from [29], is likely due to the challenging measurement of the exact location of the solubility maximum and its tie lines. In close vicinity to the alyotrope, small deviation in the liquid phase composition have a relatively large impact on the equilibrated solid phase composition. This is showcased in the distribution diagram by an almost horizontal trend of the equilibrium line near the alyotrope. Nevertheless, in both definitions, a slight shift of the alyotrope and solubility maximum towards L-leucine with an increasing temperature is observed. This shift results from a larger increase in general solubility of L-leucine rich solutions with temperature compared to L-valine rich solutions, since the solubility of L-valine seems to be less temperature dependent than that of L-leucine . A similar phenomenon was observed in various systems forming partial solid solutions. Here, the double saturation point of partial solid solutions could be shifted with a comparable temperature change [18–20]. However, the overall temperature dependency of the L-valine /L-leucine system, and therefore its effect on the alyotropic composition, is relatively minor.

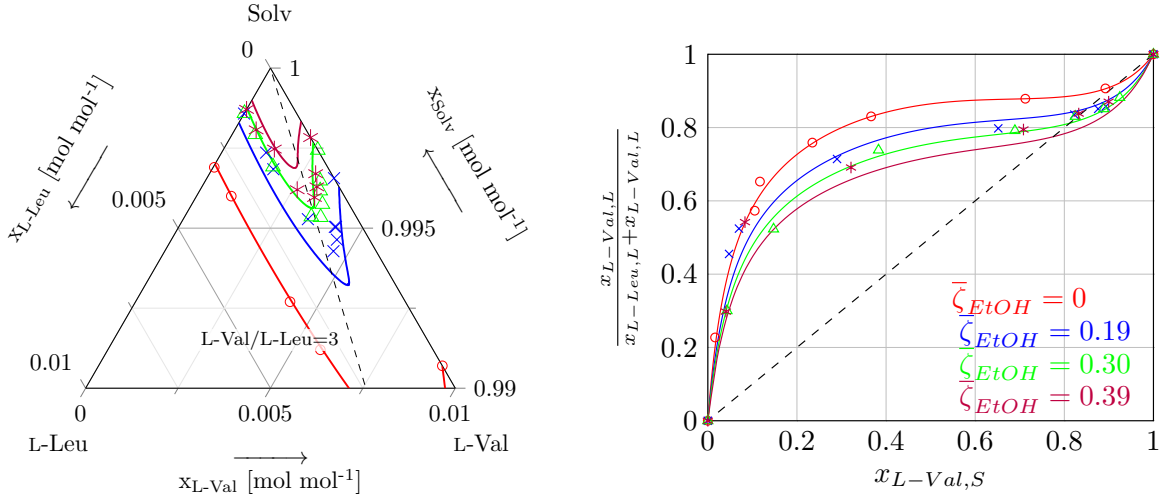

Figure 3.9: Left: ternary phase diagram of L-valine and L-leucine in various water/ethanol mixtures at 25 °C. Dots: experimental data; solid lines: calculated using Eq. (2.42); dashed line: constant L-valine /L-leucine = 3 ratio (left) and 45° line (right). Right: corresponding distribution diagram. Partly published in [1].

A comparable shift can be observed, if instead of temperature, the solvent composition is varied. Figure 3.9 presents the ternary (left) and distribution (right) diagram of the solid-liquid equilibria of L-valine and L-leucine mixtures in various water/ethanol solutions at 25 °C. It should be noted, that the solvent phase *Solv* changes composition depending on the amount of ethanol, since multiple ternary diagrams are superimposed into one. Ethanol acts as an antisolvent and decreases the solubility of the solutes with an increasing antisolvent fraction. Since ethanol effects the solubility of L-valine more than solubility of L-leucine (see Figure 3.9 (left)), the alyotropic composition also changes with an increasing amount of antisolvent. The dashed line in the ternary diagram of Figure 3.9 denotes a

constant L-valine /L-leucine ratio of three to one, and with it, the change of the alyotrope composition becomes easier to observe. Again, the distribution diagram (see Figure 3.9 (right)) provides a more clear depiction of said shift, however, the decrease in solubility cannot be represented. According to the empirical model, given in Eq. (2.42), the molar alyotropic composition is shifted from ∼ 90/10 in water to ∼ 78/22 L-valine /L-leucine in a water/ethanol mixture with $\overline{\zeta}_{EtOH} = 0.39$. Additional measurements were performed using isopropanol and acetone as antisolvents. Their equilibrium data sets for various compositions are listed in Appendix A.2. In these systems, a comparable shift of the alyotropic composition, with a decreasing L-valine to L-leucine ratio with increase of the antisolvent factor ζ, was observed. Eq. (2.42) shows similar accuracy as in Figure 3.9 for the description of these antisolvents. Additionally, isopropanol shows a comparable decrease of solubility and comparable tie line behavior to ethanol. Acetone exhibits a stronger antisolvent effect and decreases the solubility more strongly per mole of antisolvent when compared to ethanol and isopropanol.

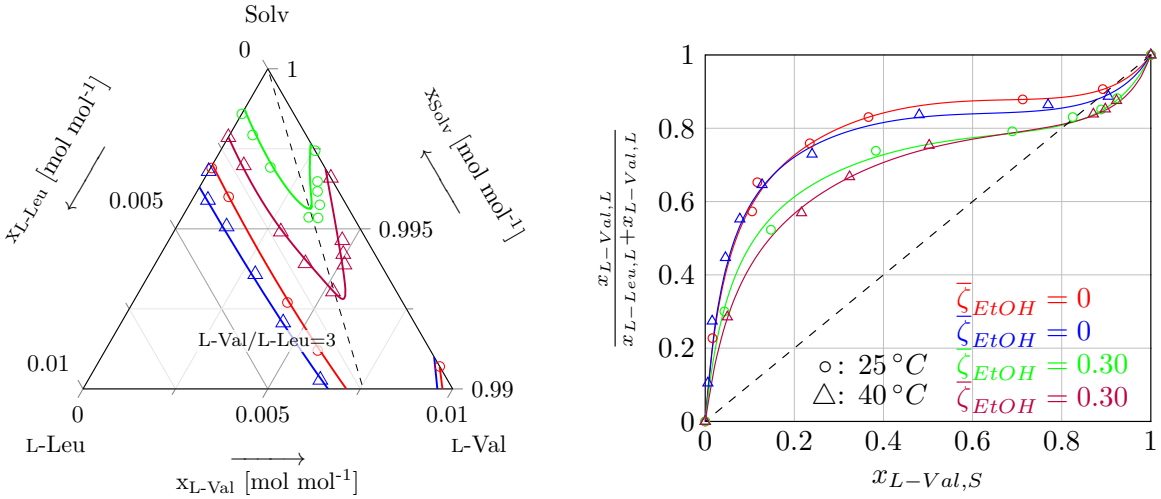

Figure 3.10: Left: ternary phase diagram of L-valine and L-leucine in water and a water/ethanol mixture ($\overline{\zeta}_{EtOH} = 0.30$) at 25 (○) and 40 °C (△). Dots: experimental data; solid lines: calculated using Eq. (2.42); dashed line: constant L-valine /L-leucine = 3 ratio (left) and 45° line (right). Right: corresponding distribution diagram. Partly published in [1].

When comparing solubilities of L-valine and L-leucine in water/ethanol mixtures at different temperatures, an increase of the solubility with temperature can be observed (see Figure 3.10). However, the relative solubility maximum and with it the alyotropic composition does not seem to change with temperature for ethanol as antisolvent. In analogue to solid-liquid behavior in water, the distribution diagram shows a decrease of the area between the equilibrium and 45° line on the L-leucine side of the alyotrope and a slight increase of said area towards L-valine. Therefore, even without a shift of the alyotrope, a change in temperature influences the separation efficiency via crystallization. See Section **4.3.2** for more information.

3.4 Modeling Solid-Liquid Equilibria of Continuous Solid Solutions

Results of thermodynamic modeling of continuous solid solutions are shown and compared to experimental data sets in this section. The modeling approach is based on equilibrium models for complete solid solutions proposed in [28], while in [84] an alternative semi-empirical model based on NRTL is given. The related theory, equations, and the models themselves are given in Section **2.2** in greater detail. Eq. (2.17) gives a relation of equilibrated solid and liquid phase compositions for regarded solute mixtures in a solvent. In this work, the activity coefficients γ_i of the solutes are calculated by semi-empirical NRTL (see Section **2.2.2**) and predictive PC-SAFT (see Section **2.2.1**) models for the solid and liquid phases, respectively. Pure component activities $a_{i,S}^{pure}$ (see Eq. (2.18)) are either calculated using Eq. (2.19) and melting data given in [64], or pure solute solubility is given as experimental data, while activity coefficients are calculated by PC-SAFT. Using experimental solubility data as model inputs anchors the model to the pure component solubilities and provides a perfect match for the pure solute predictions. However, the region, where solid solutions are formed, is still calculated predictively. In the following, results of both approaches are shown and compared. The model parameters of NRTL and PC-SAFT models as well as melting data are given in Appendix A.3. Parameters of NRTL were fitted to ternary solubility data in water at 25 °C. Since this prediction assumes thermodynamic equilibrium, the formation of the metastable co-crystal V_3L is not regarded in the calculations. However, due to its presence in the experimental data sets, the actual equilibrium results may differ from the measured data sets. More information on this can be found in Section **3.5**. Figure 3.11 presents results of thermodynamic modeling of L-valine /L-leucine solid solutions in water at 25 °C. Overall, the various modeling approaches were able to predict the alyotropic crystallization behavior. Further, both model variants show reasonable agreement with the experimental data sets towards the edges of the ternary phase diagram. However, the model accuracies decrease towards the solubility maximum. For the prediction of the solubility curve, the method relying on melting data yields slightly lower solubility values (dashed line). Crystallization behavior of the system is predicted almost identically by both models. Thus, the calculated equilibrium lines in the distribution diagram are almost completely overlapping.

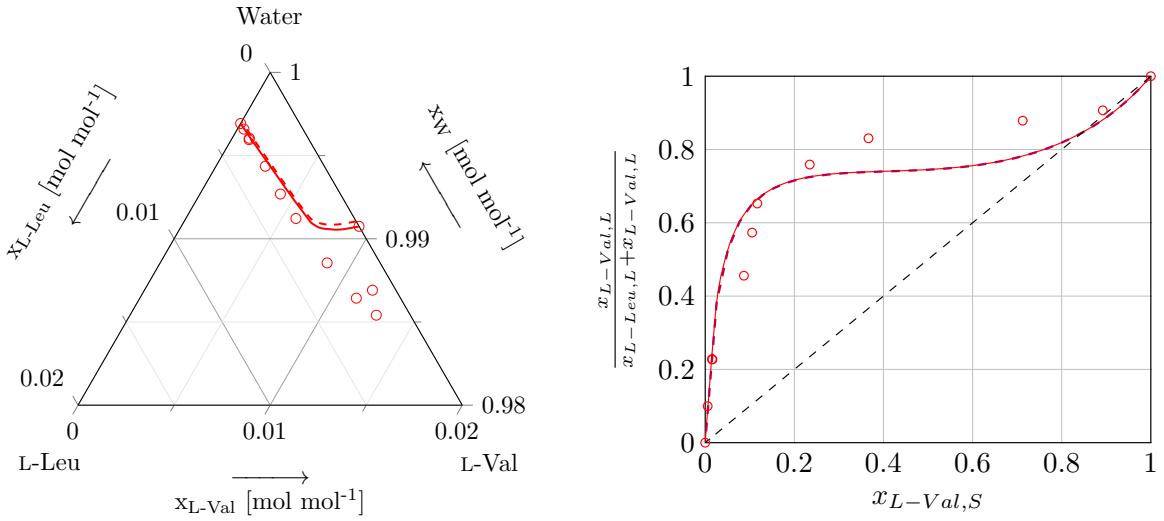

Figure 3.11: Left: ternary phase diagram of L-valine and L-leucine in water at 25 °C. Dots: experimental data; solid line: calculated with given pure solute solubility data; dashed line: calculated with pure component activity from melting data; Right: corresponding distribution diagram. Dashed black line: 45° line. Published in [2, 3].

In an effort to improve model accuracy, the k_{ij} parameter between L-valine and L-leucine, previously kept at 0, was fitted to experimental data. However, no significant improvement of the prediction was observed [3], and thus, $k_{L-Val,L-Leu} = 0$ was chosen for further modeling.

Since modeling of ternary systems involving continuous solid solutions was successful [3], the various approaches are extended to quaternary systems containing an antisolvent [2]. Following, Eq. (2.17) is extended for a quaternary *qua* liquid phase.

$$x_{i,S}^{bin}\gamma_{i,S}^{bin} = \frac{x_{i,L}^{qua}\gamma_{i,L}^{qua}}{x_{i,L}^{bin}\gamma_{i,L}^{bin}} \tag{3.10}$$

Where $x_{i,L}^{bin}\gamma_{i,L}^{bin} = a_{i,S}^{pure} = const.$, independent of the solvent composition.

Pure component PC-SAFT parameters of the antisolvents are available in literature (see Table A.19). NRTL parameters were already fitted to the ternary system in [3] and are still valid, since the binary solid phase does not change. However, k_{ij} between the antisolvents and solutes have to be determined with fitting to pure component solubility data sets using Eq. (2.18). For L-valine, solubility data sets in ethanol, isopropanol, and acetone at various temperatures are given in [70]. The solubility data for L-leucine and fitted k_{ij} parameters, determined in this work, are given in Table A.6 and A.20, respectively. Figure 3.12 presents solubilities of L-valine and L-leucine in various antisolvents and their predictions using PC-SAFT.

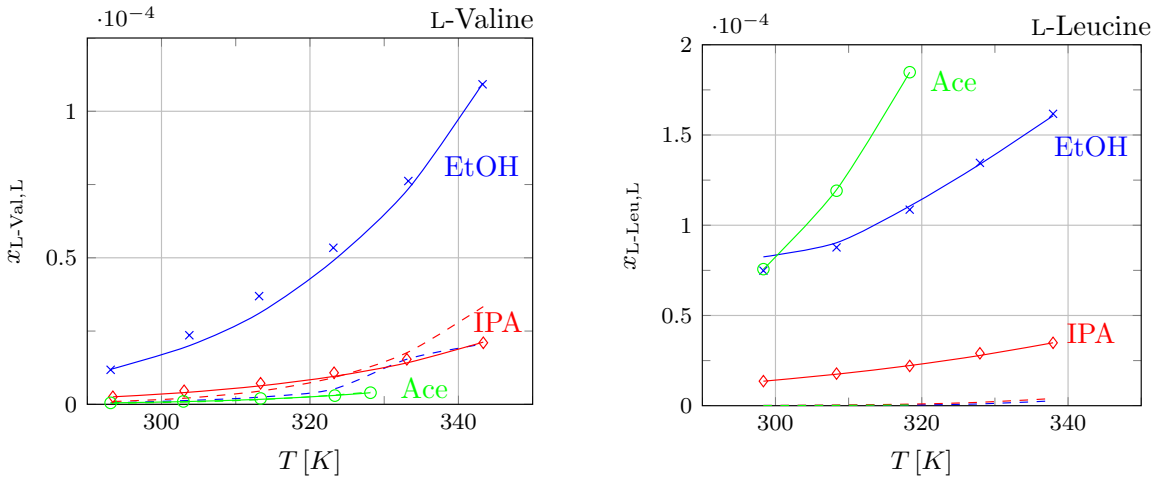

Figure 3.12: Solubilities of L-valine (left, from [70]) and L-leucine (right) in ethanol (x, blue), isopropanol (◇, red), and acetone (o, green) and their respective predictions by PC-SAFT at various temperatures. Dashed lines: calculated with $k_{ij} = 0$. Published in [2].

According to these data sets, L-valine exhibits lower solubility in the antisolvents overall when compared to L-leucine. Ethanol shows the highest, while acetone yields the lowest solubility with L-valine as a solute. For L-leucine, it gives the highest solubility out of the chosen antisolvents due to its lower relative polarity. Isopropanol dissolves the least amount of L-leucine. Ethanol for L-valine and acetone for L-leucine show the largest influences of temperature on the solubility. A overall trend of the solubility with solvent polarity can be observed for L-valine, which is more polar compared to L-leucine. The least polar solvent, being acetone, shows the highest solubility for L-leucine, while ethanol as the most polar solvent shows only slightly lower values. The low solubility of L-leucine in isopropanol could be explained by sterical hindrances of these two larger molecules (relative to the other mixtures).

Isopropanol, for both solutes, and acetone, for L-valine, exhibit only small temperature dependencies. PC-SAFT predictions, with fitted k_{ij} parameters, agree well with the solubility data sets apart form a slight underestimation of L-valine solubility in ethanol and an overprediction of L-leucine solubility in ethanol at around 25 °C. It should be noted, that for the fitting of k_{ij} only the lowest and highest points were used, while the lines between those points were calculated predictively. If $k_{ij} = 0$ is used, the solubility is generally underestimated for both solutes. However, L-valine solubility in isopropanol and acetone can be predicted reasonably well with $k_{ij} = 0$. For L-valine in ethanol as well as L-leucine in all of the chosen solvents, the solubilities are vastly underestimated without the correction via k_{ij}. Especially, for L-leucine, the model is not able to distinguish significantly between the chosen antisolvents.

k_{ij} parameters, fitted to pure component solubilities, are used in the subsequent qua-

ternary modeling. Firstly, Figure 3.13 presents the (pseudo-)ternary and distribution diagrams of the thermodynamic modeling of L-valine /L-leucine in various water/ethanol mixtures at 25 °C via melting properties acquired form [64]. For this, no additional experimental data sets are required, since the NRTL parameters were already fitted to ternary data. This leads to a significantly decreased experimental effort required for the description of solid-liquid equilibria as compared to empirical models in Section **2.2.3**, which require extensive experimental data sets.

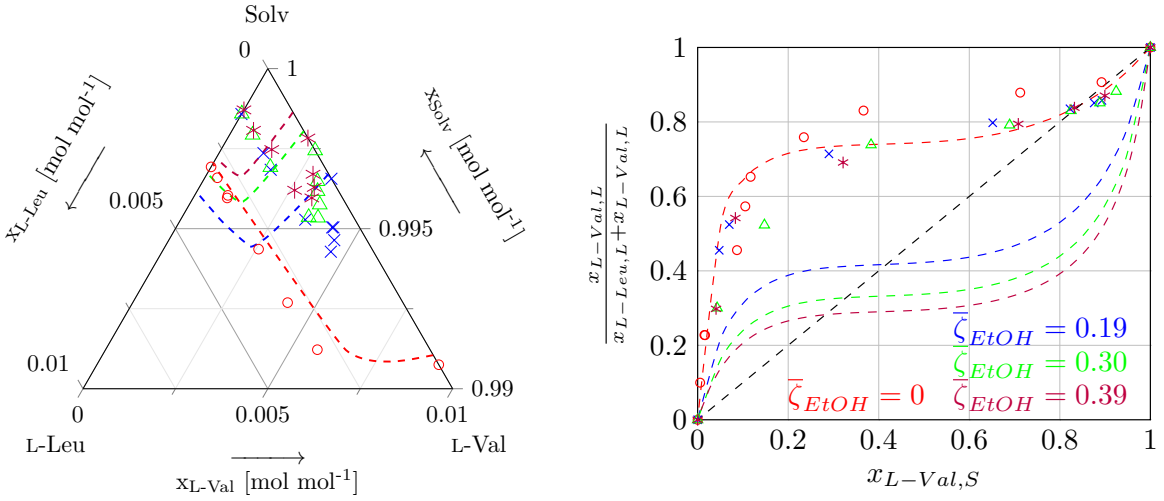

Figure 3.13: Left: ternary phase diagram of L-valine and L-leucine in various water/ethanol mixtures at 25 °C. Dots: experimental data; dashed lines: calculated with pure component activity from melting data. Right: corresponding distribution diagram. Dashed black line: 45° line. Partly published in [2].

Here, thermodynamic predictions, using melting data in their calculations, show alyotropic behavior and an overall decrease in solubility along an increasing ethanol fraction. Pure component solubilities of L-valine are described relatively well with a correct trend of solubilities. Further, L-leucine solubility increases for small fractions of ethanol, before decreasing with higher fractions. This not only results in inaccurate description of the solubility lines but also in large deviations of the alyotropic composition. Nevertheless, this model is capable of predicting alyotropic behavior and shows the correct trend of solubility decrease and shift of alyotropic composition.

Alternatively, Figure 3.14 presents calculated solid-liquid equilibria for L-valine /L-leucine in various water/ethanol mixtures at 25 °C, predicted with known (pseudo-)binary pure component solubilities.

Due to anchoring of the model with pure component solubility data to the edges of the phase diagrams, solubility decreases with increasing ethanol fractions can be described qualitatively for all compositions. Similar to predictions using melting data, the trend of the alyotrope shift can be described qualitatively as well. However, predictions via given

solubility data sets yield higher quantitative accuracy. If melting data is used to calculate pure component activities with Eq. (2.19), it will result in constant values regardless of solvent composition as it should be realistically. However, the model described in this work is not able to predict reliable results using just melting data. Extending the model with pure component solubilities, improves its accuracy, while still reducing experimental effort significantly as compared to Eq. (2.42).

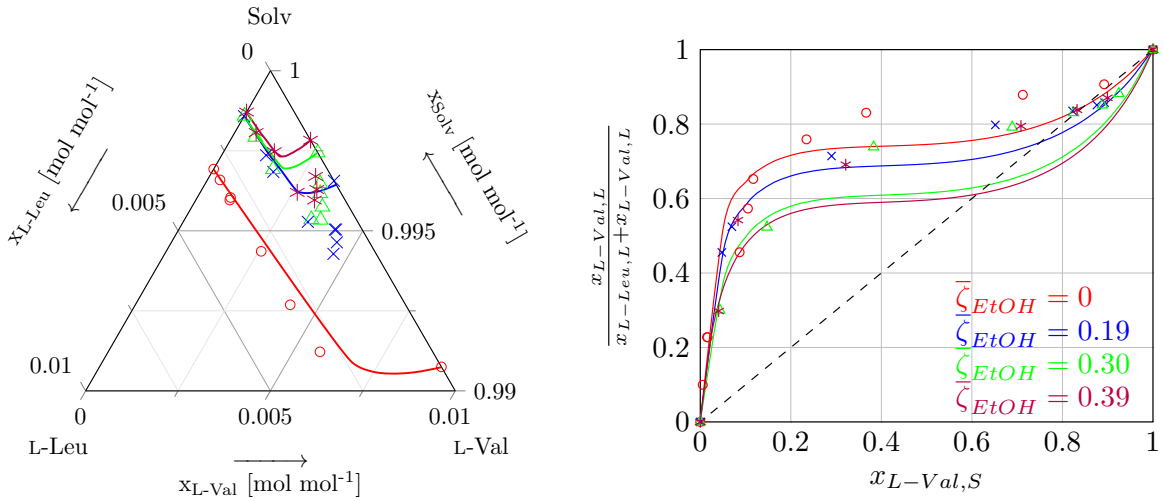

Figure 3.14: Left: ternary phase diagram of L-valine and L-leucine in various water/ethanol mixtures at 25 °C. Dots: experimental data; solid lines: calculated with given pure solute solubility data. Right: corresponding distribution diagram. Dashed line: 45° line. Partly published in [2].

Additionally, for this approach, only pure component solubility data is required. Following, more complex solid-liquid equilibria investigations for solid solutions (see Section **3.1**) can be avoided. This results in a model, useful for initial antisolvent screenings for solid solution crystallization processes without extensive experimental effort. However, for more precise process simulations, the empirical model given in Eq. (2.42) should be utilized in combination with more detailed experimental data sets.

Further examples, predicting L-valine /L-leucine solid-liquid behavior in water/isopropanol and water/acetone mixtures at 25 °C, are shown in Figures 3.15 and 3.16. Modeling systems including water/isopropanol shows similar results to modeling of water/ethanol systems in regards to solubility accuracy as well as shifts in alyotropic compositions. However, for mixtures containing acetone, while the decrease in solubility can be predicted, the shift of the alyotropic composition does not follow a reasonable trend. Determination of solid-liquid equilibria, which due to an increased equilibration time for solid solutions might allow more volatile compounds like acetone to evaporate. This might lead to inaccurate data sets, which in turn yield an inaccurate prediction using semi-empirical models. For such compounds, more elaborate experimental setups are required, to determined more accurate solid-liquid equilibrium data sets.

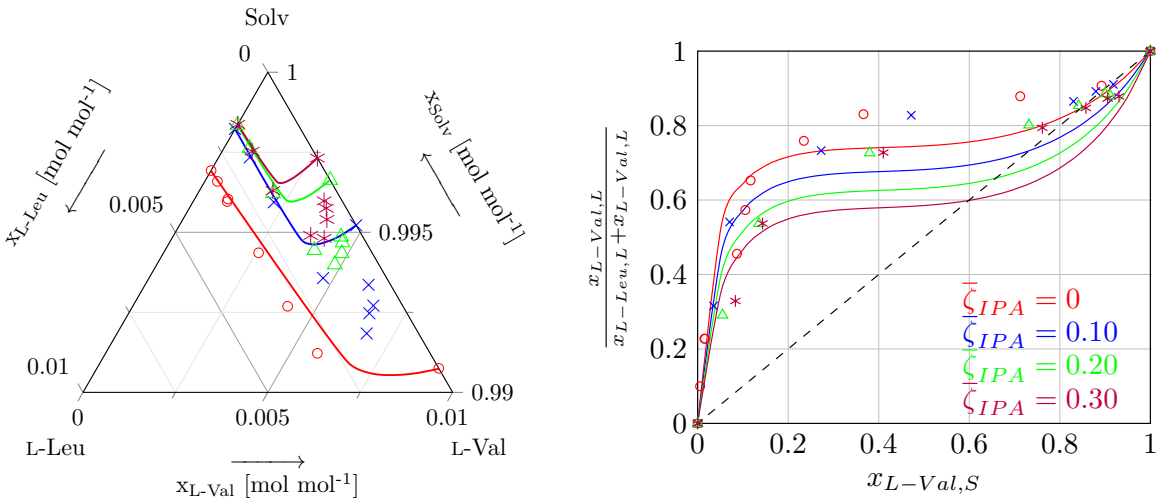

Figure 3.15: Left: ternary phase diagram of L-valine and L-leucine in various water/isopropanol mixtures at 25 °C. Dots: experimental data; solid lines: calculated with given pure solute solubility data. Right: corresponding distribution diagram. Dashed line: 45° line. Published in [2].

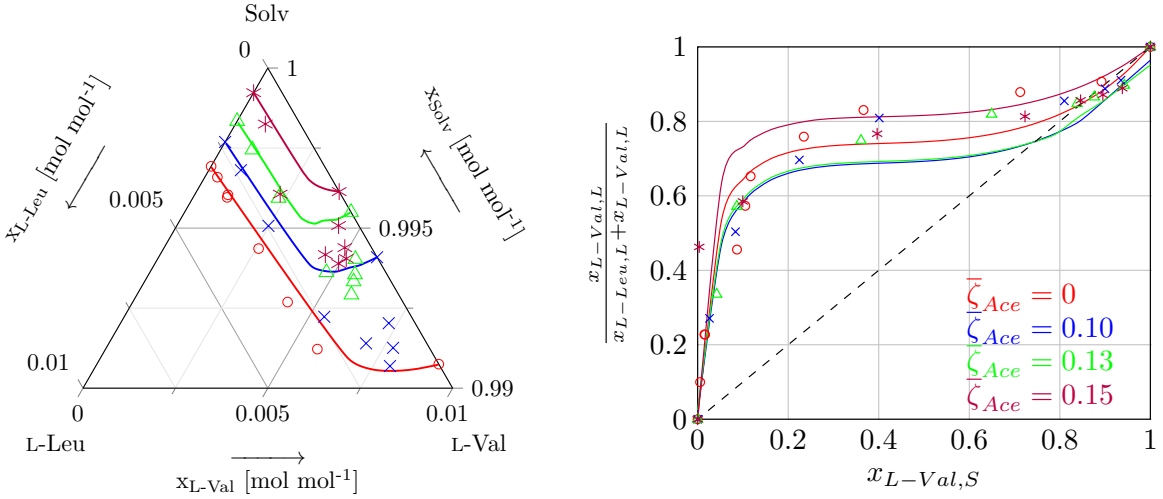

Figure 3.16: Left: ternary phase diagram of L-valine and L-leucine in various water/acetone mixtures at 25 °C. Dots: experimental data; solid lines: calculated with given pure solute solubility data. Right: corresponding distribution diagram. Dashed line: 45° line. Published in [2].

3.5 Stability Investigation of V_3L Co-Crystal

As reported in [31], in the L-valine /L-leucine system a V_3L co-crystal is formed, if recrystallized from water in the right composition range. Additionally, crystal lattice parameters and a calculated diffractogram of V_3L are given. During the solid-liquid equilibria investigation in this work, V_3L was unsystematically found in numerous solid samples independent of temperature and solvent composition. Example diffractograms of this are presented in Figure 3.17.

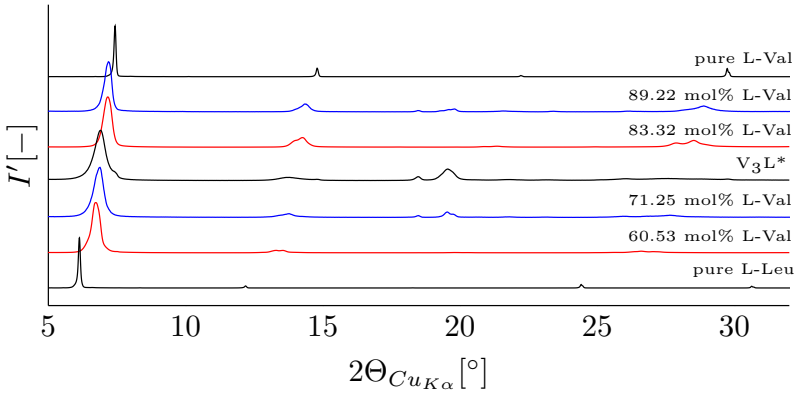

Figure 3.17: PXRD patterns of various solid phases gathered during solubility experiments of L-valine /L-leucine mixtures at 25 °C. Blue: water as solvent phase, slow crystallization; red: water/ethanol ($\overline{\zeta}_{EtOH} = 0.1924$) as solvent phase, fast crystallization; black: diffractogram of pure components; *: calculated diffractogram acquired from [31].

In Figure 3.17, characteristic peaks of V_3L are observed in samples recrystallized slowly by water evaporation (blue) at angles of 18 to 20°. In samples recrystallized from water/ethanol mixtures (red), via fast antisolvent crystallization, these characteristic peaks are missing. However, biphasic behavior is observed at the 14 to 14.5° and 26 to 27.6° peaks. These peaks are also present in the calculated diffractogram of V_3L. Assuming complete solid phase miscibility of L-valine and L-leucine , V_3L has to be present in all mixed samples shown in Figure 3.17.

Interestingly, even though V_3L is found in several solid phases, their corresponding liquid phases do not show typical co-crystal behavior (see Figure 2.10) in neither their ternary nor their distribution diagrams. Typical co-crystal behavior of a comparable system is observed in the L-valine /L-isoleucine system, which forms a V_2I co-crystal [50]. This leads to the hypothesis, that V_3L is a metastable compound, since equilibration in the liquid is much faster as compared to the solid phase. Additionally, due to the faster crystallization, smaller crystals are obtained via antisolvent crystallization, which again, equilibrate faster than larger crystals. This could be a reason, that metastable V_3L is harder to detect when obtained from water/ethanol solutions.

To test this hypothesis, V_3L needs to be manufactured as or purified into a pure form. Since co-crystals dissociate in solution, a simple purification via HPLC is not possible. An alternative approach is dry or liquid-assisted grinding of pure amino acids L-valine and L-leucine at V_3L composition. By grinding, energy is introduced into the system, which enables molecular mixing and phase transitions into solid solutions and co-crystals. This favors metastable states if enough energy is supplied. For this, a Retsch MM400 grinding mill was used. In this work, $\sim$ 1 g of amino acids, with a molar ratio of 3/1 L-valine /L-leucine , were ground for 30 min at 25 Hz in a 10 mL stainless steel vessel alongside two stainless steel balls ($\varnothing$ = 10 mm) without or in presence of solvents. After grinding, samples were dried overnight at 40 °C in a vacuum oven and analyzed via PXRD. Figure 3.18 depicts an excerpt of the results of PXRD measurements of dry or liquid-assisted grinding runs using various amounts of either water or ethanol as added solvent.

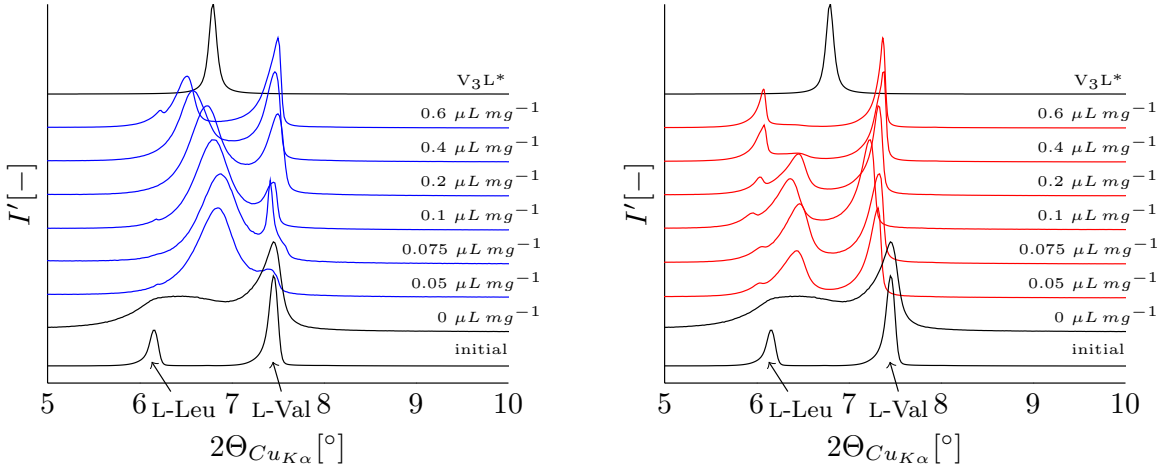

Figure 3.18: Characteristic parts of PXRD patterns of samples produced by liquid-assisted grinding of 3/1 L-valine /L-leucine using various amounts of added water (left, blue) or ethanol (right, red). Ground at 25 Hz for 30 min. *: calculated diffractogram acquired from [31].

In Figure 3.18, the initial sample illustrates the starting condition of a 3/1 L-valine /L-leucine mixture. Only pure component peaks are observed at 6 and 7.5° for L-leucine and L-valine , respectively. Additionally, the pre-calculated V_3L pattern with a characteristic peak at 6.8° is shown. Grinding of the initial sample, without any added liquid, resulted in a partially amorphous solid, in which L-valine seemed to remain mostly crystalline and L-leucine transformed into a mostly amorphous solid. V_3L cannot be seen in the PXRD pattern of this sample. Further, a slight peak widening can be observed for almost all samples, which can be attributed to a decrease in mean particle size due to grinding. This, however, was not further investigated during this work.

With addition of water to the grinding process, formation of V_3L is observed. Here, a smaller fraction of added water, favored co-crystal formation. Since a larger fraction of L-valine still remained in most samples (peak at 7.5°), the resulting solid solution is based on

V_3L and L-leucine . This shows a partial miscibility of the co-crystal and pure components, analogue to Figure 2.11. However, a small fraction of unconverted L-leucine is present in some samples. The best conversion of the initial sample into V_3L was obtained with 0.05 $\mu L\ mg^{-1}$ added water. A similar trend in V_3L formation is observed, when ethanol, instead of water, is used as added liquid. Smaller amounts of ethanol again tend to yield more V_3L, while at larger amounts of ethanol practically no co-crystal was formed. Larger fractions of L-valine and L-leucine are observed and less V_3L is formed overall as compared to samples ground in presence of water. Therefore, higher solubility of the solutes in water, as compared to ethanol, aids formation of V_3L, due to increased liquid phase mass transfer. Additionally, influences of grinding time were investigated. Since manufacturing of V_3L was the goal of these experiments, 0.05 $\mu L\ mg^{-1}$ water was added during grinding, as it yielded the most V_3L out of the performed experiments. Figure 3.19 presents PXRD patters resulting for varying grinding times of water-assisted grinding.

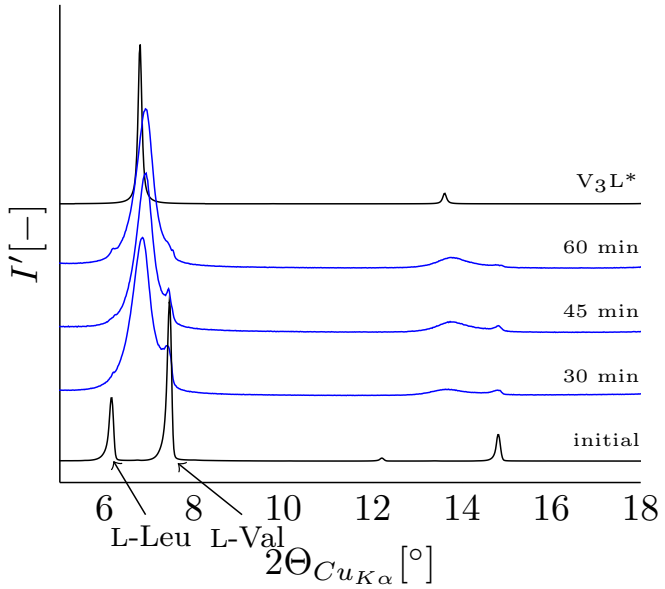

Figure 3.19: PXRD patterns of samples produced by liquid-assisted grinding of 3/1 L-valine /L-leucine with varying grinding times. Ground at 25 Hz with 0.05 $\mu L\ mg^{-1}$ added water. *: calculated diffractogram acquired from [31].

In Figure 3.19, all ground samples show a L-valine and a small L-leucine fraction, which were not converted by grinding. A significant decrease of residual L-valine is observed with an increase in grinding time (peak at 7.5 and 15°). After grinding for 60 min, almost all L-valine and L-leucine was converted into a V_3L and L-valine based solid solution. This is observed at the characteristic co-crystal peak, which is slightly shifted to higher angles when compared to its calculated pattern. An additional characteristic V_3L peak is observed at 13.5° for all samples also showing this shift. An increased grinding time, which supplies a larger amount of energy to the system, leads to an increased formation of V_3L and underlines the hypothesis of V_3L being metastable.

To further test this theory, slurry equilibration experiments were performed. For this, several samples of 3/1 L-valine /L-leucine with varying solid phases were given into a corresponding saturated aqueous solutions according to its solubility (see Section **3.3**). The samples consisted of (1): a physical mixture of L-valine and L-leucine ; (2): a ground mixture obtained after grinding for 60 min with 0.05 µ$L\ mg^{-1}$ added water (see Figure 3.19); (3): a 50/50 wt.% physical mixture of (1) and (2). The suspensions were sealed into vials and stirred at 25 °C for three weeks. Afterwards, the solid phases were filtered, dried, and analyzed via PXRD. Figure 3.20 presents the related PXRD patterns.

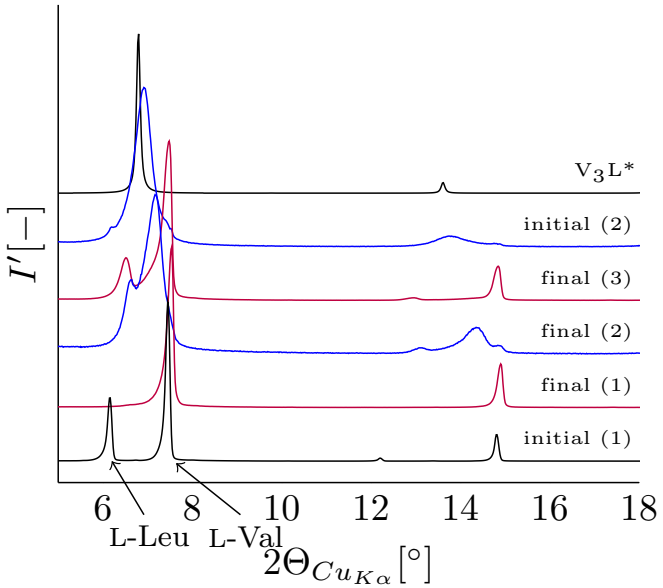

Figure 3.20: PXRD patterns of samples before and after slurry equilibration at 25 °C for three weeks. (1): physical mixture of L-valine and L-leucine ; (2): ground mixture obtained after grinding for 60 min with 0.05 µ$L\ mg^{-1}$ added water; (3): physical 50/50 wt.% mixture of (1) and (2). *: calculated diffractogram acquired from [31].

After three weeks of slurrying, sample (1), which was a physical mixture of 3/1 L-valine /L-leucine initially, resulted in an almost pure L-valine solid phase. This could be, due to a slight deviation of the liquid phase composition near to the solubility maximum, which has a large impact on the corresponding solid phase equilibrium composition. In this sample, no V_3L was found. In sample (2), originally mostly V_3L, two solid solutions based on L-valine and L-leucine with the co-crystal are observed. The formation of these solid solutions requires a decrease of pure V_3L to supply pure amino acids for the solid solutions. A more clear decrease of the co-crystal fraction is observed with sample (3). Here, both amino acids (1) as well as V_3L (2) were present initially. Only solid solutions based on L-valine and L-leucine can be found after three weeks. Similar to (1), no pure co-crystal is remaining in this sample after equilibration. This, in addition to the decrease of V_3L in sample (2), again indicates metastable behavior of the heteromolecular compound found

in this system.

In an alternative approach to obtain pure V_3L, sublimation experiments were performed. Various sublimation experiments including L-valine and L-leucine were conducted in literature and were used as guidance regarding sublimation temperatures and pressures during this work [85–89]. Additionally, in [89], an unidentified crystal structure was observed during sublimation of L-valine /L-leucine mixtures, matching V_3L's PXRD pattern. The sublimation was performed in a vacuum tube at a pressure of 300 mbar. The tube was submerged in an oil bath for temperature control. At the upper part of the tube, a cold finger was used, for recrystallization from the gaseous phase, and cooled with an external water supply to be at ∼20 °C. An initial sample, containing mostly V_3L, was produced via liquid-assisted grinding as explained prior. This sample was sublimated at different temperatures (142 and 152 °C) until recrystallization on the cold finger was observed. The sublimation was stopped, and the recrystallized as well as residual solid phases were analyzed by PXRD measurement. Additionally, at 142 °C, effects of longer sublimation time, i.e. 3 h, were investigated. The resulting PXRD patterns are presented in Figure 3.21.

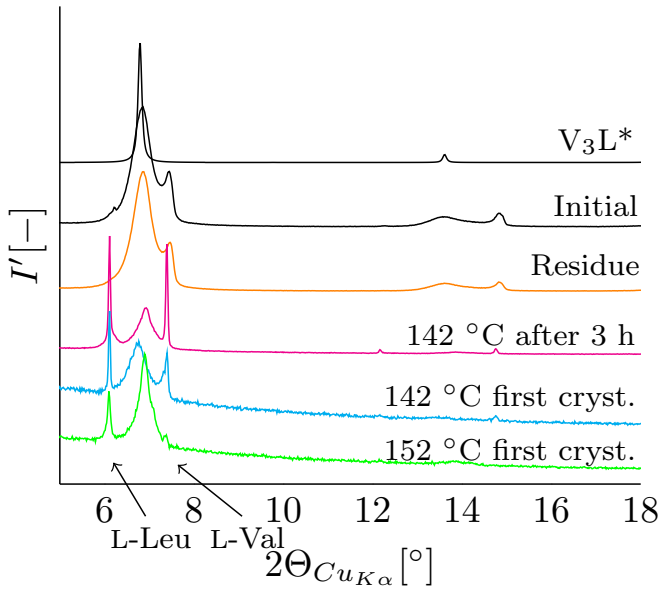

Figure 3.21: PXRD patterns of various samples obtained during the sublimation experiments at 300 mbar, various temperatures, and sublimation times. *: calculated diffractogram acquired from [31].

The pattern of the initial sample, manufactured by liquid-assisted grinding, shows it mainly consists of V_3L, alongside a small fraction of L-leucine and a slightly larger L-valine fraction. In Figure 3.21, after sublimation, only the residual solid phase after 3 h at 142 °C is shown. Residual solids of other experiments were comparable and show very little deviation from the initial sample overall. However, in the residue, pure L-leucine was not observed, implicating L-leucine sublimates largely before the other components. Since

recrystallized samples were collected directly after crystallization (green and cyan in Figure 3.21), only a tiny amount was available for PXRD measurement. This leads to low intensities and therefore, a relatively high amount of noise. In theses samples, all components of this system, being L-leucine , V_3L, and L-valine , are observed with their characteristic peaks at 6, 6.8, and 7.5°, respectively. In the sample sublimated at 142 °C, all compounds are found in relatively similar quantities. Sublimate at 152 °C exhibits only a tiny fraction of pure L-valine and a larger V_3L fraction. Following, V_3L was obtained in higher purity by sublimation at higher temperatures. This could again be reasoned with V_3L being metastable, since at higher temperatures, a steeper temperature gradient between the gaseous phase and cold finger is formed. This leads to faster and therefore, less equilibrated crystallization. After sublimating for 3 h at 142 °C (purple), all compounds were observed. However, relative to L-valine and L-leucine , V_3L is observed in lower relative amounts when compared to the first crystals formed (cyan). During sublimation, no solid solution based on pure L-valine or L-leucine was observed in any of the sublimates. However, in samples sublimated for 3 h at 142 °C and at 152 °C until first crystals were observed, a shift of V_3L's characteristic peak (normally at 6.8°) towards pure L-valine , which might indicate a V_3L-based solid solution. Solid solutions as well as V_3L are assumed to dissociate into gaseous L-valine and L-leucine molecules and recrystallize onto the cold finger. Here, due to the steep temperature gradient, initially metastable V_3L forms as seen in the samples collected directly after crystallization. L-Valine and L-leucine are formed predominately during extended sublimation times.

As mentioned previously in this chapter, V_3L was found in numerous solid phase samples during the solid-liquid investigations. However, unlike V_2I (see [50]), V_3L did not show the typical co-crystal system's behavior in the liquid phase. This can be observed when comparing the solubility data e.g. for water in Figure 3.7 with the schematic co-crystal behavior in presence of solid solutions in Figure 2.10. None of our data sets for ternary or quaternary systems exhibit local extreme points of eutectic composition. This, in combination with the metastability of V_3L investigated in this chapter, entails one of the following possibilities as true. Either, due to the metastability of V_3L and the faster equilibration in the liquid phase, V_3L does not have an influence on the liquid phase solubility and hence does not show typical co-crystal system's behavior. Or, alternatively, local points of eutectic composition are located extremely close together and investigations of solid-liquid equilibria are not precise enough to distinguish them particularly in the low overall solubility values observed in this system in Section **3.3**. Additionally, this would require V_3L to be partially miscible with the pure amino acids, since a local minima at the composition of the co-crystal is not observed in all experiments. However, regardless which of these possibilities holds true, both behave similar to a purely alyotropic system (see Figure 2.8). Therefore, the formation of metastable V_3L can largely be disregarded during the design of crystallization-based separation processes as seen in Chapter **4**.

4. Counter-Current Crystallization

4.1 General Principle

Counter-current process schemes are often used in industry and research due to their more efficient mass and energy transfer properties as comparable to co-current processes. E.g., in simple heat exchangers, counter-current flow schemes are utilized to increase heat transfer and with it, the efficiency of the apparatus [90]. An arbitrary comparison between co- and counter-current heat transfer is presented in Figure 4.1, showcasing the efficiency increase with counter-current operations.

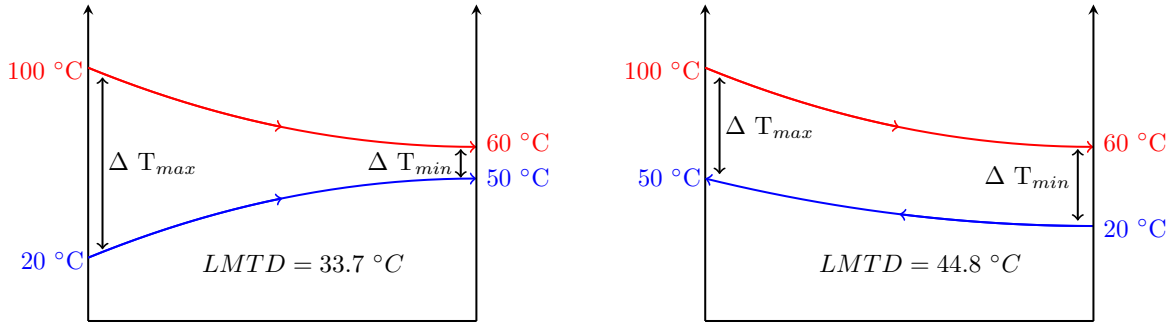

(a) Co-current **(b)** Counter-current

Figure 4.1: Arbitrary temperature trends of a heat exchanger operating in co- (left) and counter-current (right). Red: hot streams; blue: cold streams.

In Figure 4.1, a hot stream is cooled down form 100 to 60 °C with a cold stream, which itself is heated from 20 to 50 °C in the process. To quantify the driving force between hot and cold streams in the heat exchanger, for each operating scheme, the logarithmic mean temperature difference ($LMTD$) is calculated, according to [91], as follows.

$$LMTD = \frac{\Delta T_{max} - \Delta T_{min}}{\ln\left(\frac{\Delta T_{max}}{\Delta T_{min}}\right)} \tag{4.1}$$

where ΔT_{max} and ΔT_{min} are the maximum and minimum temperature differences at the respective sides of the heat exchanger. For the co- and counter-current schemes mean logarithmic temperatures of $LMTD = 33.7\,°C$ and $44.8\,°C$ are determined, respectively.

This translates to a larger temperature difference and therefore, overall driving force between hot and cold streams for the counter-current scheme when compared to co-current operation.
Apart from usage in heat exchangers, counter-current operating schemes are often utilized in separation processes to increase the driving force i.e. in terms of increased concentration gradients. Examples for counter-current operation in separation processes are rectification, counter-current extraction, chromatography and crystallization [13]. While this work predominately focuses on the latter, its process variations are influenced by well known techniques from other counter-current processes, mainly from rectification. Hence, the rectification process is briefly explained in the following section.
Rectification is a process utilizing multistage counter-current distillation [92]. In distillation, two or more components are separated via temperature due to their differences in boiling temperatures. In a simple distillation, a low-boiling component A is enriched in the head as a vapor phase, which is usually condensed and collected inside a distillate vessel. Contrary, a high-boiling component B remains mostly in the liquid phase. Rectification intensifies this process by applying the counter-current scheme, and thus increasing the mean concentration difference between the rising vapor and the liquid which is flowing down the column. Figure 4.2 (left) depicts a simple rectification column separating low- and high-boiling components A and B. Here, the feed stream is supplied in the middle of the column, while the distillate, rich in A, and the bottoms, rich in B, are withdrawn at the top and bottom of the column, respectively. At the bottom, a reboiler, partially evaporates the bottoms and its vapor is redirected into the column, which supplies the energy required to separate A and B into the column. At the top, the distillate is completely condensed and partially given back into the column as a cold liquid. These flows are characterized by the reflux and reboiling ratios R_D and R_B, respectively.

$$R_D = \frac{n_{L,J_{max}}}{n_D} \tag{4.2}$$

$$R_B = \frac{n_{V,J_0}}{n_B} \tag{4.3}$$

In the equations above, L and V describe the liquid and vapor phases and D and B are the distillate and bottom streams, respectively. It should be noted that the indices of the separation stages J of the various streams are based on which stage the streams originate from, e.g. $n_{L,J_{max}}$ is the liquid stream exiting the last stage at the top of the column.
Usually, these reflux streams are used to control the temperatures at the top and bottom of the column and with them, the temperature gradient. These temperatures as well as the overall temperature gradient in the column, set the purities, which can be obtained with respect to A and B in the distillate and at the bottom, respectively.

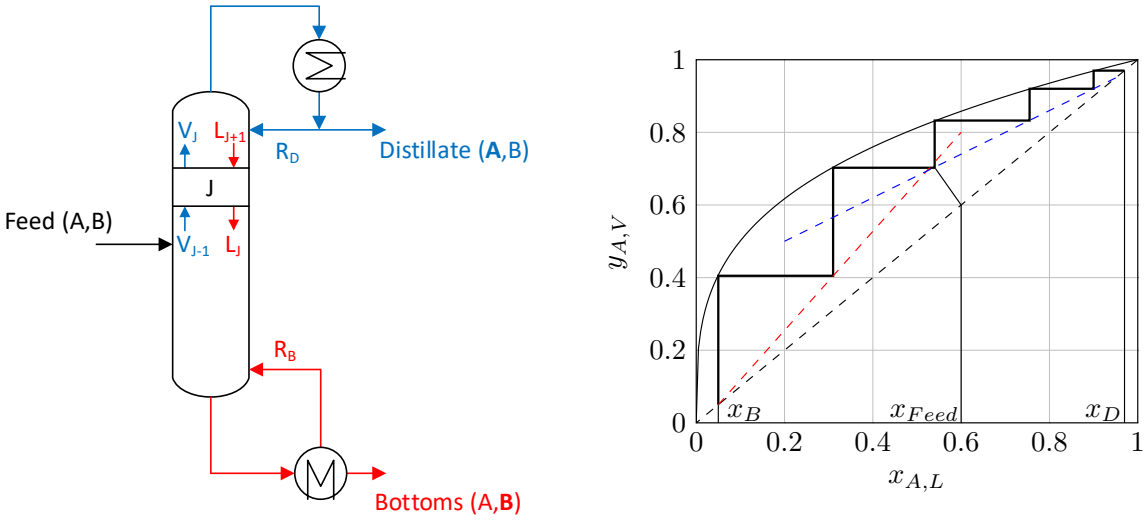

Figure 4.2: Schematic representation of a rectification process. Left: process flow sheet. Red: liquid streams enriched in B; blue: vapor streams enriched in A. With R_D and R_B being reflux ratios of the distillate and bottoms, respectively. Right: corresponding distribution diagram. Red and blue dashed lines: operating lines; black dashed line: 45° line; black lines: curved equilibrium line and theoretical separation stages.

To predict the separation of a binary mixture in a rectification column based on the reflux ratios, general molar balances around a theoretical stage J are derived for the rectifying (above feed inlet) and stripping (below feed inlet) sections. For a stage J (see Figure 4.2), this results in the following relation.

$$y_{i,J}n_{V,J} + x_{i,J}n_{L,J} = y_{i,J-1}n_{V,J-1} + x_{i,J+1}n_{L,J+1} \tag{4.4}$$

Where y_i and x_i are vapor and liquid phase molar fractions of compound i.
Since this relation is valid for all theoretical stages in the column, it can be used to describe the rectifying and stripping section by combining it with the reflux ratios given in Eqs. (4.2) and (4.3) (e.g. [92]). This specifies operating lines for the respective sections, shown in the distribution diagram (Figure 4.2, right) as blue and red dashed lines.

$$y_i = \frac{R_D}{R_D+1}x_i + \frac{1}{R_D+1}x_{i,D} \tag{4.5}$$

$$y_i = \frac{R_B+1}{R_B}x_i - \frac{1}{R_B}x_{i,B} \tag{4.6}$$

The reflux ratios dictate the slope and with it the y-intersect point of the operating lines in the distribution diagram. A comparable equation can be derived for the separation stage to which the feed is supplied [92].

$$y_i = \frac{q_F}{q_F - 1} x_i + \frac{1}{q_F - 1} x_{i,Feed} \tag{4.7}$$

q_F is defined as the caloric factor and describes the vaporization energy requirement considering the latent heat of vaporization in the feed stream. Figure 4.3 illustrates the influence of various values of q_F on illustrating the feed stream in distribution diagrams.

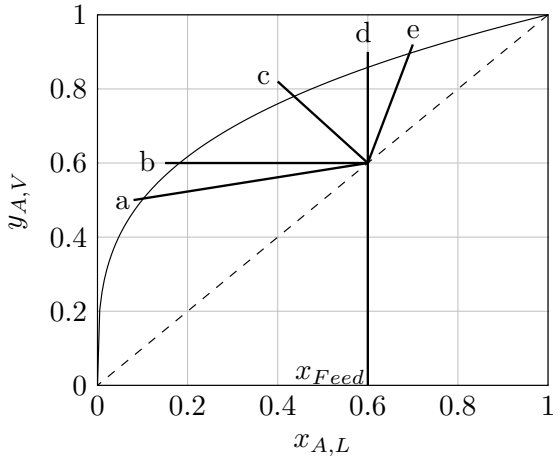

Figure 4.3: Distribution diagram of a feed stream entering a rectification column. Black dashed line: 45° line; curved line: equilibrium line; linear lines: feed entering at different caloric factors q_F; a: superheated vapor $q_F < 0$; b: saturated vapor $q_F = 0$; c: vapor-liquid mixture $0 < q_F < 1$; d: boiling liquid $q_F = 1$; e: subcooled liquid $q_F > 1$. Illustration inspired by [92].

For $q_F = 0$ and for $q_F = 1$, the feed is present as a saturated vapor or boiling liquid, respectively. Therefore, the feed is given into the column along a horizontal line for a vapor and a vertical line for a completely liquid feed at boiling temperature, in accordance with the axis of the diagram. If q_F possesses a value between 0 and 1, a partially evaporated liquid/vapor mixture is present. The angle of the feed line in the distribution diagram is dependent on the ratio of vapor to liquid, whereas a larger vapor fraction leads to a lower q_F value and therefore a more horizontal line. Two extreme cases, for $q_F < 0$ and $q_F > 1$ are applicable, if the feed is supplied as superheated vapor or subcooled liquid, respectively.

For known reflux ratios, operating lines, and a known feed composition as well as its caloric factor, the number of theoretical separation stages, required for solving a given separation task, can be determined graphically via the McCabe-Thiele method [46]. The resulting stage construction was shown in the distribution diagram in Figure 4.2 (right).

Transfer to Crystallization

In analogue to rectification, counter-current crystallization can be an alternative to classical fractional crystallization. Both types of crystallization processes are shown schematically in Figure 4.4.

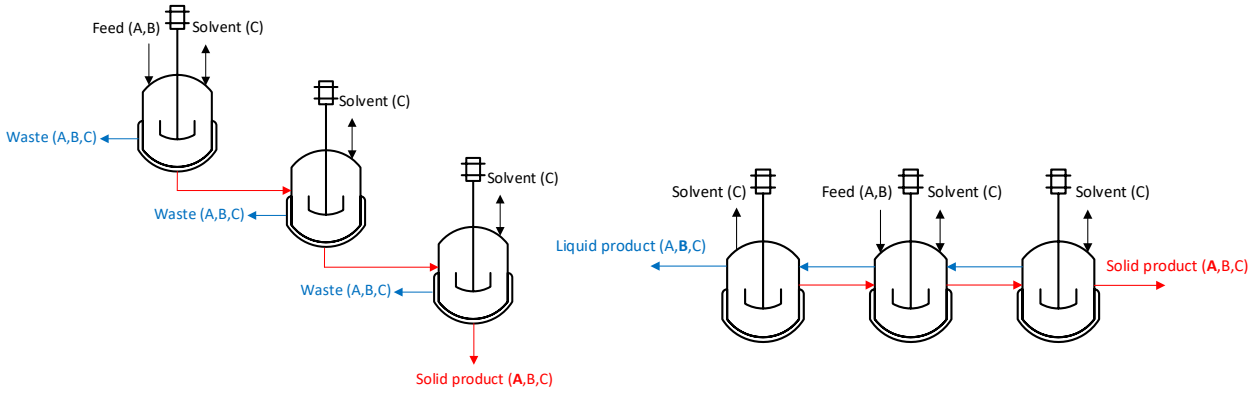

Figure 4.4: Schematic representation of three stage fractional (left) and counter-current (right) crystallization processes. Red: solid streams enriched in A; blue: liquid streams enriched in B.

Fractional crystallization processes are used to purify target compounds to high purities, using a multistage crystallization cascade [12]. Via repeated crystallization and redissolving the resulting solid phase in fresh solvent, potential impurities can be subsequently removed further as compared to the previous stage. The resulting mother liquors, which are saturated with impurity-rich solute are separated and discarded after each crystallization step. This process can be utilized to achieve extremely high purities in the crystalline phase, applicable for providing highly valuable APIs or to purify a target compound from a solid solution forming system as discussed in this thesis.

Since in the fractional crystallization, the liquid phase is discarded after every separation step, large amounts of waste streams are accumulated. While these waste streams mostly contain the impurities (i.e B) also a significant amount of target compound A is lost with the waste fractions. Counter-current crystallization is used to minimize waste streams by reusing liquid phases to partially dissolve solid phases and therefore enable the target compound to be recaptured in the next crystallization cycle. Several literature sources describe counter-current solution crystallization aspects to purify solid solutions for various systems, among others [13, 17–26]. While these works focus mainly on solution crystallization, multiple studies of counter-current melt crystallization of solid solutions are given in literature as well, e.g. [93–96].

If solid phase molar fractions are plotted against solvent-free liquid phase molar fractions for solid solution forming systems, a distribution diagram is obtained, similar to Figure 4.2 (right).

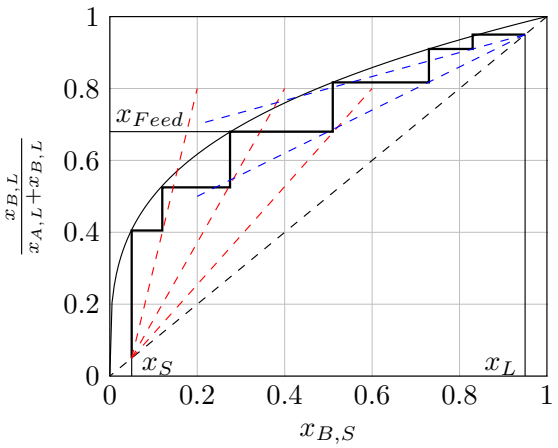

Figure 4.5: Distribution diagram of a counter-current crystallization. Red and blue dashed lines: operating lines; black dashed line: 45° line; black lines: curved equilibrium line and theoretical separation stages. Inspired by [13].

In [13], derivations of operating lines for counter-current crystallization are given. Since only solutes are regarded here, for the liquid phase, solvent-free molar fractions and masses are used.

$$x'_{B,L,J} = \frac{x_{B,L,J}}{x_{A,L,J} + x_{B,L,J}} \quad [0, \ldots, 1] \tag{4.8}$$

$$n'_{L,J} = n_{L,J}\left(1 - x_{Solv,L,J}\right) \tag{4.9}$$

Again, two sections can be defined in a counter-current crystallization cascade. Crystallizers, in the first section, between liquid product $J = 1$ and feed crystallizer $J = J_{Feed}$, are described as follows.

$$x'_{B,L,J+1} = \left(1 - \frac{n_{S,J}}{n'_{L,J+1}}\right) x'_{B,L,J+1} - \frac{n_{S,J}}{n'_{L,J+1}} x_{B,S,J} \tag{4.10}$$

Analogously, in the section between feed crystallizer $J = J_{Feed}$ and the solid product $J = J_{max}$ the following equation is valid [13].

$$x'_{B,L,J} = \left(\frac{n_{S,J-1}}{n'_{L,J}} - 1\right) x_{B,S,J_{max}} - \frac{n_{S,J-1}}{n'_{L,J}} x_{B,S,J-1} \tag{4.11}$$

Due to the need for complete recrystallization to fully rebuild the crystal lattice, the feed streams are typically completely dissolved. Therefore, the feed can always be treated as a

saturated liquid stream, which eliminates the need for an equation, analogue to Eq. (4.7). If all streams are known, Eqs. (4.10) and (4.11) can be used to construct operating lines for each specific stage and then, a graphical separation stage construction can be performed as illustrated in Figure 4.5.

For the description of rectification, operating lines for the different sections are identical, since refluxes do not change over said sections. However, in counter-current crystallization, each crystallizer exhibits a different reflux, due to gradually varying purification grades. Depending on the supersaturation, a specific tie line is obtained for each crystallizer, which leads to different solid and liquid phase compositions. Generally, lower supersaturations provide less crystals with higher purity, while higher supersaturations conversely result in more crystals with lower purification. Therefore, without knowledge of the exact streams, a graphical construction and a prediction of required separation stages is virtually impossible without further constraints, e.g. constant grades of purification. In addition to the complicated prediction, the different behavior of each separation stage makes a quantitative comparison between various stages difficult. This is especially true, if in the different stages different temperatures or crystallization strategies are used.

To support a reasonable comparison and quantification, a novel approach to describe the purification effectiveness, designated as β_i', was developed during this work. This approach was partly published in [1]. It is based on an analogy to the catalyst effectivity η_{cat}, which exploits the Thiele modulus Φ. In chemical reaction engineering, this modulus describes relation between reaction and diffusion rates [32]. The following dependency provides the dimensionless catalyst effectivity [97].

$$\eta_{cat} = \frac{\tanh(\Phi)}{\Phi} \quad [0, \ldots, 1] \tag{4.12}$$

Hereby η_{cat} quantifies on a normalized scale poor ($\eta_{cat} = 0$) and very good ($\eta_{cat} = 1$) performance, respectively.

Similarly, a quantification can be derived for the crystallization of solid solutions. A graphical depiction of the basis of this approach is given in Figure 4.6, which illustrates a distribution diagram depicting the influences of various purification outcomes during the crystallization of solid solutions. As mentioned before, to allow the formation of a solid solution with a enriched composition, complete dissolution is required prior to recrystallization. Hence, it is assumed, that initially, a homogeneous liquid phase is present inside the crystallizer. When supersaturation is generated using specific means, the subsequent crystallization supplies the system with a solid phase. Analogue to how feed streams are treated in rectification (see Figure 4.3), this solid phase is supplied into the crystallizer corresponding to a specific angle β_i in the distribution diagram.

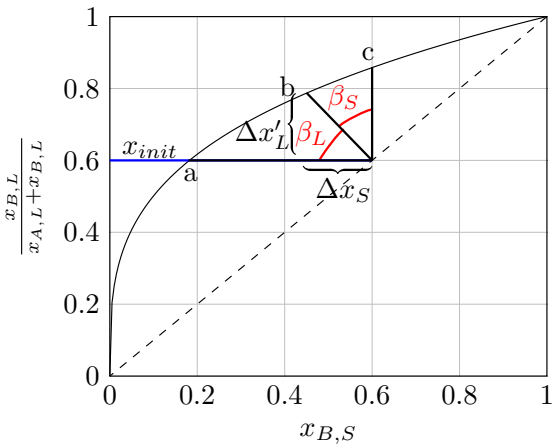

Figure 4.6: Distribution diagram of crystallization within a counter-current crystallization cascade. Black dashed line: 45° line; blue line: liquid initial composition; black lines: linear process pathways and curved equilibrium line; red: angle β_L and β_S; a: infinitesimal crystallization $\beta'_L = 0$; b: partial crystallization $0 < \beta'_L < 1$; c: complete crystallization $\beta'_L = 1$; braces: purification in the liquid $\Delta x'_L$ and solid Δx_S phases for case b. Based on [1].

Increasing values of β_L and β_S describe increased purification of the liquid and solid phase, respectively. These values are determined as a function of the composition change of the solvent-free liquid and solid phases using tangent and cotangent functions as shown in Eq. (4.13).

$$\tan(\beta_L) = \cot(\beta_S) = \left|\frac{\Delta x'_L}{\Delta x_S}\right| = \left|\frac{x'_{B,L} - x'_{B,L,init}}{x_{B,S} - x'_{B,L,init}}\right| \tag{4.13}$$

It holds $\beta_S = 90° - \beta_L$. Analogue to the mentioned catalyst effectivity η_{cat} (see Eq. (4.12)), the degree of purification of solid solution crystallization can be normalized as β'_i following Eq. (4.14).

$$\beta'_i = \frac{\beta_i}{\beta_{max}} = \frac{\beta_i}{90°} = \frac{\beta_i}{\pi/2} \quad [0, \ldots, 1] \quad i = L, S \tag{4.14}$$

In this work, β_L and β'_L are utilized predominately instead of β_S and β'_S, since they are proportional to supersaturation and describe increased crystallization with higher values. In Figure 4.6, three cases can be identified, which are explained in the following section. If only infinitesimal crystallization **(a)** occurs, virtually no solid phase is generated and therefore the composition of the liquid phase is not changed singificantly from the initial composition. This yields a horizontal line in the distribution diagram. The resulting

crystals are highly purified, since only a tiny amount of crystals nucleate. Opposite, if e.g. all solvent is evaporated and the solutes are completely crystallized **(c)**, the solid phase composition is equal to the solvent-free initial composition, resulting in a vertical depiction. For the crystallized solid, no purification occurs. It should be noted, that for cooling and antisolvent crystallization, a complete crystallization cannot be achieved, due to limiting residual solubilities at lower temperatures or in the antisolvent.
For real applications, a partial crystallization **(b)** can be assumed, which enriches the solid as well as liquid phases in their different directions (see Figure 4.4). Depending on the relative crystallization amounts, the slopes of crystallization lines in the distribution diagram change. The resulting angles β_L or β'_L, between the crystallization and initial line, quantify the purification of the liquid phase. E.g. for infinitesimal crystallization ($\beta_L = 0°$ and therefore $\beta'_L = 0$), the solid phase is highly purified, while it is not enriched at all via complete crystallization ($\beta_L = 90°$, $\beta'_L = 1$).
The introduced normalized angle β'_L can be utilized to compare the separation efficiency for different crystallizers in a counter-current cascade. Its main advantage is a straightforward quantitative comparison regardless of chosen crystallization strategy and crystallization conditions. This is especially useful, if due to different temperatures or use of antisolvents, the equilibrium lines change with supersaturation. An example of its use to aid in choosing crystallization strategies and conditions will be given in Section **4.3.2**. Sections **4.4.3** and **4.4.4** will give further interpretation of β'_L within counter-current separation processes.

4.2 Mathematical Model

For the mathematical description of a steady-state counter-current crystallization, a generalized crystallizer J (see Figure 4.4) is used as a building block. The inlet streams of J are dependent on its position within the cascade and the location of the feed. Therefore, if J is the first $J = 1$ or the last $J = N$ crystallizer in the cascade, it is not supplied with a solid S or liquid L, respectively, from the previous crystallization cycle $k-1$ according to the counter-current scheme. Hence, $S_{J=1}^{k-1} = 0$ and $L_{J=N}^{k-1} = 0$. Similarly, if J is not supplied with any feed $n_{S,Feed,J\neq J_{Feed}} = 0$ holds.
A specific crystallization cycle k for a crystallizer J can be divided into smaller substeps, where each physical operation in the process can be looked at separately and equations describing these operations can be derived. In Sections **4.2.1**, **4.2.2**, and **4.2.3** all of the relevant substeps will be explained for evaporative, cooling, and antisolvent crystallization, respectively. Balance equations suitable for process simulations will be derived. For evaporative crystallization, a preceding process model was developed by M.Sc. S. Münzberg and the utilized equations are mainly based on [26]. However, this model is extended during this work and applied to other crystallization strategies [1]. Additionally, it should

be noted, that these are transient models in which the time scale is normalized to the crystallization cycle time k.

4.2.1 Evaporative Crystallization

In this section, the mathematical model of isothermal evaporative crystallization in a counter-current crystallization involving solid solutions is detailed. In evaporative crystallization, solvent is evaporated to increase the supersaturation of a solution and eventually achieve crystallization (see Figure 2.2), either spontaneous or initialized via seeding, ultrasound etc.. The process of purifying solid solutions via evaporative crystallization in a counter-current scheme is divided into six substeps: **(1)**: mixing of solid and feed; **(2)**: mixing of solid and liquid; **(3)**: complete dissolution of remaining solid; **(4)**: solvent evaporation until desired supersaturation (without crystallization); **(5)**: crystallization along the corresponding tie line and solid-liquid separation; **(6)**: correction for residual moisture due to mother liquor adherent to the crystals. These substeps are presented in Figure 4.7 as characteristic process pathways of a specific crystallization cycle k in crystallizer J. Below, all substeps and their equation are explained.

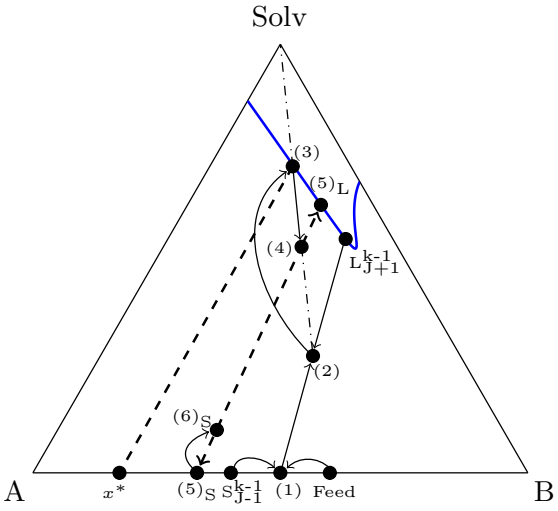

Figure 4.7: Exemplary ternary phase diagram of evaporative crystallization. **(1)**: mixing of solid and feed; **(2)**: mixing of solid and liquid; **(3)**: dissolution; **(4)**: evaporation of solvent; **(5)**: crystallization; **(6)**: correction for residual moisture. Blue line: solubility line; arrows: process pathways; dashed line/arrows: tie line/process pathways along tie line; dashdotted line: constant A:B ratio. Modification of Fig. 2a in [26].

(1): Mixing of Solid and Feed

In the first substep, potential solid feed *Feed* is physically mixed with the solid phase product S_{J-1}^{k-1} from the previous crystallizer $J-1$ of the previous crystallization cycle

$k-1$. This simple mixing can described with total and partial molar balances for N components, as follows:

$$n_{S,J}^{k,(1)} = n_{S,J-1}^{k-1,(6)} + n_{S,Feed,J} \tag{4.15}$$

$$x_{i,S,J}^{k,(1)} n_{S,J}^{k,(1)} = x_{i,S,J-1}^{k-1,(6)} n_{S,J-1}^{k-1,(6)} + x_{i,S,Feed,J} n_{S,Feed,J} \quad [i = 1, \ldots, N] \tag{4.16}$$

Hereby, the solid input is the outlet stream of the last substep $\mathbf{(6)}_S$ of the previous crystallization cycle $k-1$.

(2): Mixing Solid and Liquid

The solid phase obtained in substep **(1)** is mixed with the liquid phase product from $J+1$ and $k-1$ according to the counter-current scheme. Again, the liquid phase input L_{J+1}^{k-1} is the outlet of the previous cycle $k-1$ and is designated by $\mathbf{(6)}_L$. Substep $\mathbf{(6)}_L$ is not shown in Figure 4.7 since its composition is equal to substep $\mathbf{(5)}_L$'s. This is explained in greater detail in its corresponding section **(6)** below. Substep **(2)** is quantified with total and partial balances, analogue to **(1)**.

$$n_{SL,J}^{k,(2)} = n_{S,J}^{k,(1)} + n_{L,J+1}^{k-1,(6)} \tag{4.17}$$

$$x_{i,SL,J}^{k,(2)} n_{SL,J}^{k,(2)} = x_{i,S,J}^{k,(1)} n_{S,J}^{k,(1)} + x_{i,L,J+1}^{k-1,(6)} n_{L,J+1}^{k-1,(6)} \quad [i = 1, \ldots, N] \tag{4.18}$$

Here, SL describes a suspension of solid in a continuous liquid phase, in contrast to wet crystals, which are denoted as solid S even though solvent may be present as residual moisture.

(3): Complete Dissolution

To completely dissolve the solid in the liquid, solvent needs to be added to the suspension. In a real experimental setting, solvent is added in excess to completely dissolve to solid. In addition to solvent, which is evaporated to reach the supersaturation, also the excess solvent is evaporated in substep **(4)**. However, in the mathematical model, the exact amount of solvent required to completely dissolve the solid and to reach a homogeneously saturated liquid phase is added. Again, total and partial molar balances are used.

$$n_{L,J}^{k,(3)} = n_{SL,J}^{k,(2)} + n_{Solv,J}^{k} \tag{4.19}$$

$$x_{i,L,J}^{k,(3)} n_{L,J}^{k,(3)} = x_{i,SL,J}^{k,(2)} n_{SL,J}^{k,(2)} + x_{i,Solv,J}^{k} n_{Solv,J}^{k} \quad [i = 1, \ldots, N] \tag{4.20}$$

For a pure solvent $x_{A,Solv,J}^{k} = x_{B,Solv,J}^{k} = 0$ holds.
Since the compositions move on the isoplethic line during solvent addition and dissolution, the ratio of substances A to B does not change (see dashdotted line in Figure 4.7). Therefore, the following equation is valid.

$$\frac{x_{A,L,J}^{k,(3)}}{x_{B,L,J}^{k,(3)}} = \frac{x_{A,SL,J}^{k,(2)}}{x_{B,SL,J}^{k,(2)}} \tag{4.21}$$

To determine the amount of solvent needed for complete dissolution, additional equations for the descrition of the solubility are requried. In this work, empirical polynomial models, derived in Section **2.2.3**, are used to calculate of these solubilities. Alternatively, thermodynamical models (see Section **2.2**) can be used to describe the solid-liquid equilibria. However, higher accuracy can be obtained with the empirical approach as exhibited in Sections **3.3** and **3.4**.

$$\begin{pmatrix} x_{A,L,J}^{k,(3)} \\ x_{B,L,J}^{k,(3)} \\ x_{Solv,L,J}^{k,(3)} \end{pmatrix} = \begin{pmatrix} \sum_{m=1}^{M_A} a_m \left(x_{A,S,J}^{k,*} \right)^m \\ \sum_{m=1}^{M_B} b_m \left(x_{B,S,J}^{k,*} \right)^m \\ 1 - x_{A,L,J}^{k,(3)} - x_{B,L,J}^{k,(3)} \end{pmatrix} \tag{4.22}$$

Here, $x_{i,S,J}^{k,*}$ describes the corresponding equilibrated solid composition to the liquid phase composition on the solubility line at **(3)**. These fractions are used as supporting variables to solve these equations. Due to the nature of this problem, these equations need to be solved numerically. Information on the global simulation structure and the utilized solver are given in Section **4.3**. The initial conditions are set by the previous crystallization cycle $k-1$ for each variable. For $k = 1$, these values are set to 10^{-6}. The boundary conditions for the variables are $0 \leq x \leq 1$ and $0 \leq n \leq \infty$.

(4): Solvent Evaporation

During the evaporation substep, solvent is evaporated to reach a metastable state with a desired composition. In a real experimental setting, crystallization will occur before the

desired composition is reached and the formed crystals are stirred for an extended amount of time at stable conditions to ensure proper equilibration along the corresponding tie line. In our model however, it is assumed that no nucleation takes place in this substep and the metastable composition is reached in a homogeneous liquid phase. This leads to the total and partial substance balances below.

$$n_{L,J}^{k,(4)} = n_{L,J}^{k,(3)} - n_{Evap,J}^{k} \tag{4.23}$$

$$x_{i,L,J}^{k,(4)} n_{L,J}^{k,(4)} = x_{i,L,J}^{k,(3)} n_{L,J}^{k,(3)} - x_{i,Evap,J}^{k} n_{Evap,J}^{k} \quad [i = 1, \ldots, N] \tag{4.24}$$

Assuming pure solvent is evaporated, $x_{A,Evap,J}^{k}$ and $x_{B,Evap,J}^{k}$ are considered to be zero. Since the above balances contain five unknown variables, being $n_{L,J}^{k,(4)}$, $x_{A...C,L,J}^{k,(4)}$ and $n_{Evap,J}$, an additional equation is needed for solution. For this, a so called evaporation factor δ_J is set as a constant parameter for each crystallizer in this model. This evaporation factor is defined as the ratio of evaporated solvent amount to the total amount of solvent in state **(3)** prior to evaporation [26].

$$\delta_J = \frac{n_{Evap,J}^{k}}{x_{Solv,L,J}^{k,(3)} n_{L,J}^{k,(3)}} \tag{4.25}$$

(5): Crystallization

In the fifth substep, nucleation is initiated and crystals precipitate. Due to this, the metastable point **(4)** splits into a solid $\mathbf{(5)_S}$ and a liquid phase $\mathbf{(5)_L}$ along its corresponding tie line. Since, a description of the tie lines is necessary here, this process step is calculated numerically, analogue to substep **(3)**. Again, the initial conditions are given by the previous cycle $k-1$, while boundary conditions are defined by $0 \leq x \leq 1$ and $0 \leq n \leq \infty$. For this, the total and partial mass balances are used in combination with the empirical tie line description.

$$n_{L,J}^{k,(5)} + n_{S,J}^{k,(5)} = n_{L,J}^{k,(4)} \tag{4.26}$$

$$x_{i,L,J}^{k,(5)} n_{L,J}^{k,(5)} + x_{i,S,J}^{k,(5)} n_{S,J}^{k,(5)} = x_{i,L,J}^{k,(4)} n_{L,J}^{k,(4)} \quad [i = 1, \ldots, N] \tag{4.27}$$

$$\begin{pmatrix} x_{A,L,J}^{k,(5)} \\ x_{B,L,J}^{k,(5)} \\ x_{Solv,L,J}^{k,(5)} \end{pmatrix} = \begin{pmatrix} \sum_{m=1}^{M_A} a_m \left(x_{A,S,J}^{k,(5)} \right)^m \\ \sum_{m=1}^{M_B} b_m \left(x_{B,S,J}^{k,(5)} \right)^m \\ 1 - x_{A,L,J}^{k,(5)} - x_{B,L,J}^{k,(5)} \end{pmatrix} \tag{4.28}$$

(6): Correction for Residual Moisture

While in substep **(5)** a perfect liquid-solid separation is assumed, under real conditions, the solid phase will always have some remaining mother liquor attached to it. To take this into account, a parameter for the residual moisture R_M is set. This parameter is used to correct the liquid and solid phases considering this residual moisture. For the solid phase, this yields:

$$n_{S,J}^{k,(6)} = (1 + R_M)\, n_{S,J}^{k,(5)} \tag{4.29}$$

$$x_{i,S,J}^{k,(6)} n_{S,J}^{k,(6)} = \left(x_{i,S,J}^{k,(5)} + x_{i,L,J}^{k,(5)} R_M\right) n_{S,J}^{k,(5)} \quad [i = 1, \ldots, N] \tag{4.30}$$

For the liquid phase, the total amount of liquid decreases by the amount of liquid which is left on the solids. However, its composition does not change between $\mathbf{(6)}_L$ and $\mathbf{(5)}_L$.

$$n_{L,J}^{k,(6)} = n_{L,J}^{k,(5)} - R_M n_{S,J}^{k,(5)} \tag{4.31}$$

$$x_{i,L,J}^{k,(6)} = x_{i,L,J}^{k,(5)} \quad [i = 1, \ldots, N] \tag{4.32}$$

The resulting amounts and compositions of **(6)** for cycle k are then used as input variables in substeps **(1)** and **(2)** of the next cycle $k + 1$ according to the counter-current scheme as previously explained.

4.2.2 Cooling Crystallization

Cooling crystallization used within a counter-current process developed to purify solid solutions, is similar to evaporative crystallization in terms of the essential process pathways in the ternary diagram. However, there are some key differences as presented in Figure 4.8. Nevertheless, substeps **(1)** to **(3)** and **(6)** are identical to the model for evaporative crystallization and explained in Section **4.2.1**.

(4): Cooling from $\mathbf{T_0}$ to $\mathbf{T_1}$

To achieve a supersaturated metastable solution, the temperature is reduced from T_0 to T_1. In the mathematical model, it is assumed, that no crystallization takes place in this substep. Since nothing is added or taken from the system and no phase change occurs, all amounts and compositions remain equal to substep **(3)** as shown in Figure 4.8.

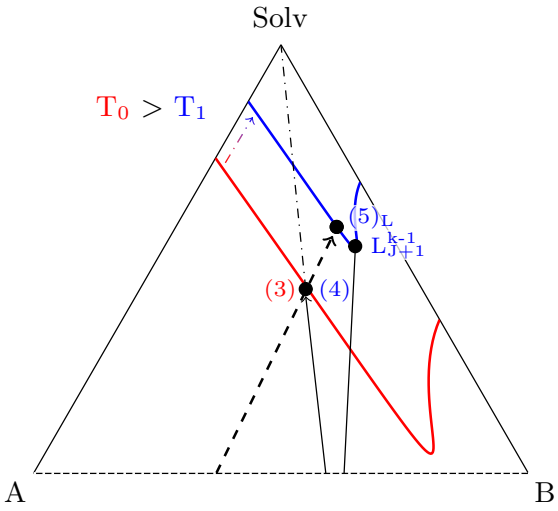

Figure 4.8: Zoomed view of the ternary phase diagram of cooling crystallization. **(3)**: dissolution; **(4)**: cooling; **(5)**: crystallization. Red line: solubility line at T_0; blue line: solubility line at $T_1 < T_0$; arrows: process pathways; dashed arrows: process pathways along tie line; dashdotted line: constant A:B ratio.

$$n_{L,J}^{k,(4),T_1} = n_{L,J}^{k,(3),T_0} \tag{4.33}$$

$$x_{i,L,J}^{k,(4),T_1} = x_{i,L,J}^{k,(3),T_0} \quad [i = 1, \ldots, N] \tag{4.34}$$

(5): Crystallization

Since **(4)** is a metastable solution, after decreasing the temperature, it will split into $\mathbf{(5)_L}$ and $\mathbf{(5)_S}$ along its corresponding equilibrium tie line for T_1. Therefore, total and molar balances and the empirical solid-liquid equilibrium description are used, in analogue to the evaporative crystallization. However, unlike in balancing substep **(3)**, where parameters for T_0 were used, now parameters for T_1, need to be considered.

$$n_{L,J}^{k,(5),T_1} + n_{S,J}^{k,(5),T_1} = n_{L,J}^{k,(4),T_1} \tag{4.35}$$

$$x_{i,L,J}^{k,(5),T_1} n_{L,J}^{k,(5),T_1} + x_{i,S,J}^{k,(5),T_1} n_{S,J}^{k,(5),T_1} = x_{i,L,J}^{k,(4),T_1} n_{L,J}^{k,(4),T_1} \quad [i = 1, \ldots, N] \tag{4.36}$$

$$\begin{pmatrix} x_{A,L,J}^{k,(5),T_1} \\ x_{B,L,J}^{k,(5),T_1} \\ x_{Solv,L,J}^{k,(5),T_1} \end{pmatrix} = \begin{pmatrix} \sum_{m=1}^{M_A} a_m(T_1) \left(x_{A,S,J}^{k,(5),T_1}\right)^m \\ \sum_{m=1}^{M_B} b_m(T_1) \left(x_{B,S,J}^{k,(5),T_1}\right)^m \\ 1 - x_{A,L,J}^{k,(5),T_1} - x_{B,L,J}^{k,(5),T_1} \end{pmatrix} \tag{4.37}$$

4.2.3 Antisolvent Crystallization

An alternative to classical evaporative and cooling crystallization is antisolvent crystallization in which a poor solvent is given into the system to decrease the solubility of dissolved compounds. This eventually leads to precipitation. In comparison to evaporative crystallization shown in Figure 4.7, the antisolvent crystallization process is identical for substeps **(1)** and **(2)**. However, other substeps need to be extended and become more complex, due to the presence of an additional component. Figure 4.9 shows the process pathways of an isothermal antisolvent crystallization in a ternary phase diagram. Here, *Solv* denotes the solvent phase regardless of the solvent/antisolvent composition. Below, solvent mixtures are denoted as $\hat{x}_{Solv}$ while x_{Solv} and x_{Anti} describe, in more detail, the individual solvent and antisolvent, respectively.

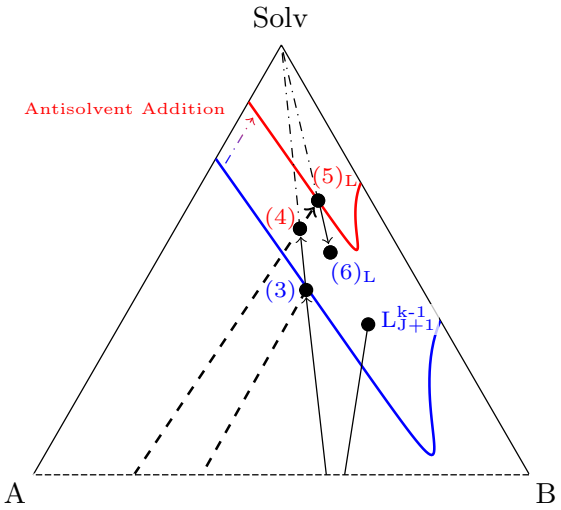

Figure 4.9: Zoomed view of the (pseudo-)ternary phase diagram of antisolvent crystallization. **(3)**: dissolution; **(4)**: antisolvent addition; **(5)**: crystallization; **(6)**: antisolvent evaporation and correction for residual moisture. Blue: solubility line of pure solvent; red: solubility line of solvent/antisolvent mixture; arrows: process pathways; dashed line/arrows: tie line/process pathways along tie line; dashdotted lines: constant A:B ratio; Solv: various solvent/antisolvent mixtures.

(3): Complete Dissolution

Due to antisolvent crystallization performed in a previous crystallization cycle, residual antisolvent may be present in the liquid and solid inputs, which will slightly decrease the solubility of the mixture and will result in a higher amount of solvent required for complete dissolution. Reasons for residual antisolvents will be discussed in more detail in substep **(6)**. If no residual antisolvent is remaining at this point, substep **(3)** is calculated as it is for evaporative crystallization, shown in Section **4.2.1**. The amount of residual antisolvent

is described with the antisolvent factor. Its general definition is given in Eq. (2.41).

$$\zeta_J^{k,(3)} = \frac{x_{Anti,L,J}^{k,(3)}}{x_{Solv,L,J}^{k,(3)}} \tag{4.38}$$

To describe the dissolution, total and partial molar balances are used, assuming that the ratio of A:B remains constant as discussed in Section **4.2.1**.

$$n_{L,J}^{k,(3)} = n_{SL,J}^{k,(2)} + n_{Solv,J}^{k} \tag{4.39}$$

$$x_{i,L,J}^{k,(3)} n_{L,J}^{k,(3)} = x_{i,SL,J}^{k,(2)} n_{SL,J}^{k,(2)} + x_{i,Solv,J}^{k} n_{Solv,J}^{k} \quad [i = 1, \ldots, N] \tag{4.40}$$

$$\frac{x_{A,L,J}^{k,(3)}}{x_{B,L,J}^{k,(3)}} = \frac{x_{A,SL,J}^{k,(2)}}{x_{B,SL,J}^{k,(2)}} \tag{4.41}$$

To quantify the residual antisolvent, the simple polynomial model (see Eq. (2.40)) is extended to consider solvent/antisolvent mixtures in Eq. (2.42).

$$\begin{pmatrix} x_{A,L,J}^{k,(3)} \\ x_{B,L,J}^{k,(3)} \\ \hat{x}_{Solv,L,J}^{k,(3)} \end{pmatrix} = \begin{pmatrix} \sum_{m=1}^{M_A} a_{m,1} \cdot \exp\left(a_{m,2} \cdot \zeta_J^{k,(3)}\right) \left(x_{A,S,J}^{k,*}\right)^m \\ \sum_{m=1}^{M_B} b_{m,1} \cdot \exp\left(b_{m,2} \cdot \zeta_J^{k,(3)}\right) \left(x_{B,S,J}^{k,*}\right)^m \\ 1 - x_{A,L,J}^{k,(3)} - x_{B,L,J}^{k,(3)} \end{pmatrix} \tag{4.42}$$

Where, $x_{i,S,J}^{k,*}$ again describes the corresponding equilibrated solid molar fraction of substep **(3)**.

(4): Addition of Antisolvent

In analogue to Sections **4.2.1** and **4.2.2**, in substep **(4)** supersaturation is created, by addition of antisolvent. Still no crystallization takes place. The system reaches a metastable composition, since antisolvent addition results in a decrease in solubility for components A and B in the solvent mixture *Solv*. Eq. (4.43) shows the total molar balance of the antisolvent addition. The composition in substep **(4)** is calculated solving substance specific balances (see Eq. (4.44)).

$$n_{L,J}^{k,(4)} = n_{L,J}^{k,(3)} + n_{Anti,J}^{k,(4)} \tag{4.43}$$

$$x_{i,L,J}^{k,(4)} n_{L,J}^{k,(4)} = x_{i,L,J}^{k,(3)} n_{L,J}^{k,(3)} + x_{i,Anti,J}^{k,(4)} n_{Anti,J}^{k,(4)} \quad [i = 1, \ldots, N] \tag{4.44}$$

The antisolvent factor $\zeta_J^{k,(4)}$ (see Eq. (4.45)) needs to be specified in the mathematical model. Here, the amount of antisolvent $n_{Anti,J}^{k,(4)}$ can be calculated exploiting the definition of ζ in Eq. (2.41). However, due to residual or impure antisolvent, $\zeta_J^{k,(4)}$ is extended.

$$\zeta_J^{k,(4)} = \frac{n_{Anti,J}^{k,(4)} x_{Anti,Anti,J}^{k,(4)} + n_{L,J}^{k,(3)} x_{Anti,L,J}^{k,(3)}}{n_{Anti,J}^{k,(4)} x_{Solv,Anti,J}^{k,(4)} + n_{L,J}^{k,(3)} x_{Solv,L,J}^{k,(3)}} \tag{4.45}$$

In Eq. (4.45), $n_{Anti,J}^{k,(4)} x_{Anti,Anti,J}^{k,(4)}$ and $n_{L,J}^{k,(3)} x_{Anti,L,J}^{k,(3)}$ describe the amounts of added pure antisolvent and residual antisolvent to the pure solvent $n_{L,J}^{k,(3)} x_{Solv,L,J}^{k,(3)}$, respectively. The product $n_{Anti,J}^{k,(4)} x_{Solv,Anti,J}^{k,(4)}$ is the amount of solvent added in combination with the antisolvent, which happens when recycling impure antisolvent. More information on the recycling of impure antisovlent is given in Section **4.4.2**.

(5): Crystallization

The crystallization step is described identically as for evaporative and cooling crystallization. Hence, total and partial molar balances and the empirical model are used. Here, the antisolvent factor from substep **(4)** $\zeta_J^{k,(5)} = \zeta_J^{k,(4)}$ has to be used in order to account for the correct liquid phase composition. Again, this substep is calculated numerically with aforementioned initial and boundary conditions for various variables.

$$n_{L,J}^{k,(4)} = n_{L,J}^{kt,(5)} + n_{S,J}^{k,(5)} \tag{4.46}$$

$$x_{i,L,J}^{k,(4)} n_{L,J}^{k,(4)} = x_{i,L,J}^{k,(5)} n_{L,J}^{k,(5)} + x_{i,S,J}^{k,(5)} n_{S,J}^{k,(5)} \quad [i = 1, \ldots, N] \tag{4.47}$$

$$\begin{pmatrix} x_{A,L,J}^{k,(5)} \\ x_{B,L,J}^{k,(5)} \\ \hat{x}_{Solv,L,J}^{k,(5)} \end{pmatrix} = \begin{pmatrix} \sum_{m=1}^{M_A} a_{m,1} \cdot \exp\left(a_{m,2} \cdot \zeta_J^{k,(5)}\right) \left(x_{A,S,J}^{k,(5)}\right)^m \\ \sum_{m=1}^{M_B} b_{m,1} \cdot \exp\left(b_{m,2} \cdot \zeta_J^{k,(5)}\right) \left(x_{B,S,J}^{k,(5)}\right)^m \\ 1 - x_{A,L,J}^{k,(5)} - x_{B,L,J}^{k,(5)} \end{pmatrix} \tag{4.48}$$

(6): Correction for Residual Moisture and Removal of Antisolvent

Besides the correction of the solid and liquid phases to regard for residual moisture on the crystals after solid-liquid separation, the removal and recycle of antisolvent is regarded in substep **(6)** as well. Analogue to evaporative and cooling crystallization, the solid phase can be described using the parameter R_M (see Eq. (4.49)) for the residual moisture.

$$n_{S,J}^{k,(6)} = (1 + R_M)\, n_{S,J}^{k,(5)} \tag{4.49}$$

$$x_{i,S,J}^{k,(6)} n_{S,J}^{k,(6)} = \left(x_{i,S,J}^{kt,(5)} + R_M x_{i,L,J}^{k,(5)}\right) n_{S,J}^{k,(5)} \quad [i = 1, \ldots, N] \tag{4.50}$$

It should be noted, that corrections for residual moisture only affect the overall amount and not the composition of the liquid phase. However, removing antisolvent from the mixture influences the liquid phase composition, as shown below. Here, $n_{Anti,J}^{k,(6)}$ describes the total amount of liquid which is removed, i.e. via evaporation during antisolvent removal. If, in addition to antisolvent, solvent is removed as well. This scenario can be described with the composition of the removal stream $x_{i,Anti,J}^{k,(6)}$.

$$n_{L,J}^{k,(6)} = n_{L,J}^{k,(5)} - R_M n_{S,J}^{k,(5)} - n_{Anti,J}^{k,(6)} \tag{4.51}$$

$$x_{i,L,J}^{k,(6)} n_{L,J}^{k,(6)} = x_{i,L,J}^{k,(5)} \left(n_{L,J}^{k,(5)} - R_M n_{S,J}^{k,(5)}\right) - x_{i,Anti,J}^{k,(6)} n_{Anti,J}^{k,(6)} \quad [i = 1, \ldots, N] \tag{4.52}$$

The antisolvent separated in this step is reused in substep **(4)** of the next cycle as part of an antisolvent recycle. Hence, the compositions of the antisolvent, in substep **(4)** and **(6)**, are the same. The amount of the removal stream $n_{Anti,J}^{k,(6)}$ is calculated by subtracting the antisolvent, which is on the crystals as residual moisture $R_M x_{Anti,L,J}^{k,(5)} n_{S,J}^{k,(5)}$ and the residual antisolvent $R_{Anti} n_{L,J}^{k,(6)}$ in the liquid from the total amount of antisolvent present in the system $x_{Anti,L,J}^{k,(5)} n_{L,J}^{k,(5)}$ and by adding the amount of solvent, which is removed with the antisolvent, $x_{Solv,Anti,J}^{k,(6)} n_{Anti,J}^{k,(6)}$.

$$n_{Anti,J}^{k,(6)} = x_{Anti,L,J}^{k,(5)} n_{L,J}^{k,(5)} - R_M x_{Anti,L,J}^{k,(5)} n_{S,J}^{k,(5)} - R_{Anti} n_{L,J}^{k,(6)} + x_{Solv,Anti,J}^{k,(6)} n_{Anti,J}^{k,(6)} \tag{4.53}$$

These assumptions allow to regard for residual antisolvent in the solid and liquid phases due to non-complete separation in substep **(3)** as well as impure antisolvent recovery and therefore impure antisolvent in the next crystallization cycles in substep **(4)**.

4.3 Application of the Model

The mathematical model, described in prior sections, requires a multitude of parameters to successfully calculate the various substeps of the process and acquire a prediction of the counter-current crystallization. Among others, such parameters include crystallization strategies, number of crystallizers and their volume, crystallization conditions and desired supersaturation defined by temperature differences or evaporative δ and antisolvent ζ factors (see Eqs. (4.25) and (2.41)) as well as thermodynamic data regarding solubilities

and tie lines. Here, the crystallization behavior is described by polynomial parameters $a_{m,i}$ and $b_{m,i}$ (see Eq. (2.42)), which are fitted to experimental data sets summarized in Section **3.3**. This sections aims to explain the global structure of the simulations as well as its utilization to determine aforementioned parameters to be used in a sensitivity study for a separation of L-valine /L-leucine solid solutions.
While simulations for various crystallization strategies are using different equations, the overarching simulation structure is identical for all variants. A flow sheet of the simulations is shown in Figure 4.10 and explained in greater detail below. For the calculations, MATLAB® was utilized during this work to accommodate the simulation framework.

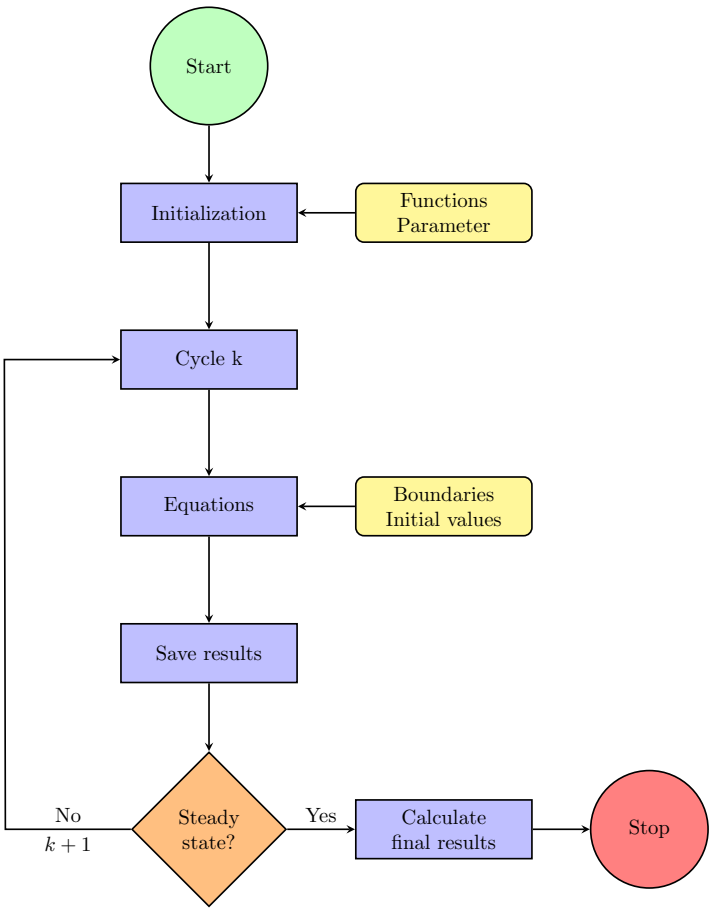

Figure 4.10: Flow sheet of the global simulation structure. Blue: main simulation step; yellow: input; orange: decision; green: starting point; red: stopping point of the simulation.

After starting a simulation, various variables were initialized. Additionally, often used function such as empirical models (see Eq. (2.42)), calculations from molar to mass fractions (see Eq. (3.5)), etc. are given to the simulation as subroutines. Further, parameters describing the process, i.e. total number of crystallizers J_{Max}, feed crystallizer J_{Feed}, empirical parameters a and b, evaporation δ_J or antisolvent factor ζ_J among others, are

defined here. In the beginning of the first crystallization cycle $k = 1$ of each simulation, all crystallizers in the counter-current cascade are empty and get successively filled with each additional cycle starting with a feed stream n_{Feed}, which all variables are normalized to. During every cycle k, the simulation calculates various substeps in each crystallizer with the mathematical model, given in Section **4.2**. Substeps **(3)** and **(5)** require iterative solving, due to their nonlinear nature. Here, the solver *lsqnonlin* is utilized for the calculations, which allows for respective boundary conditions and initial values to be supplied. As mentioned in Section **4.2**, inital values are given by the previous crystallization cycle $k - 1$, while the boundary conditions are $0 \leq x \leq 1$ and $0 \leq n \leq \infty$. The resulting values for all variables are saved in a solution structure and compared to results of previous cycles to determine if a steady state was reached. For this, it was assumed that a steady state was reached if the deviation over the last four cycles ($k - 4$ to k) are smaller then a predefined value, in this work usually $< 10^{-5}$. If a steady state is not yet reached, the calculation starts over for the next cycle $k + 1$ and the loop continuous until the maximum number of cycles k_{max} is reached. Otherwise, if the process is in steady state, the normalized variables are scaled to a predetermined value, e.g. the maximum volume of the crystallizers, to acquire more practical values. Additionally, all molar streams and composition are transformed to mass based values as well. Further, product purities and yields for components A and B, as well as the purification grades β_i', are calculated, which are saved and exported into a result matrix alongside all other variables. In this work, if not stated otherwise, the parameters for residual moisture and antisolvent were set to $R_M = 0.25$ and $R_{Anti} = 0.01$, while the purity of the recycled antisolvent were set to $w^{k,(6)}_{Anti,Anti,J} = 0.85$ for ethanol, 0.80 for isopropanol, and 0.99 for acetone based potential azeotrope formation as well as on experimental data sets acquired with the process equipment (see Section **4.4.1**). For an ideal calculation, the values for residuals can be set to 0 depending on chosen simplifications. Further, if in an experiment pure antisolvent is used during crystallization and no antisolvent recycle is performed, $w^{k,(6)}_{Anti,Anti,J} = 1$ holds.
To increase the speed of the iterative calculations during the simulation, the jacobian matrix J_f is manually provided to the solver. This reduces the amount of calculations the solver has to perform to calculate the jacobian matrix automatically and allows the simulation to yield results in a few seconds. The jacobian matrix is defined as the differential matrix of all functions f for all variables x:

$$J_f = \left(\frac{\partial f_i}{\partial x_j}\right)_{i=1,\ldots,n;\, j=1,\ldots,m} = \begin{pmatrix} \frac{\partial f_1}{\partial x_1} & \frac{\partial f_1}{\partial x_2} & \cdots & \frac{\partial f_1}{\partial x_m} \\ \frac{\partial f_2}{\partial x_1} & \frac{\partial f_2}{\partial x_2} & \cdots & \vdots \\ \vdots & \vdots & \ddots & \vdots \\ \frac{\partial f_n}{\partial x_1} & \cdots & \cdots & \frac{\partial f_n}{\partial x_m} \end{pmatrix} \tag{4.54}$$

The MATLAB® scripts of various simulations for different crystallization strategies and hybrid processes, proposed in Section **4.4.4**, are given in the digital supporting information of this work.

4.3.1 Parameter Determination

As discussed in prior sections, for a given set of parameters, such as number of crystallizers, evaporative δ or antisolvent ζ, etc., a counter-current crystallization process at steady state can be calculated. However, the counter-current crystallization for the separation of solid solutions and the determination of its parameters proposes a challenging optimization problem. After deciding about solvents, crystallization strategies, temperature levels, and for antisolvent crystallization, the antisolvents themselves, purities, yields, purification grade β_J and evaporation δ_J/antisolvent ζ_J factors need to be optimized. Thus, the problem requires a multi-objective optimization. One approach is the usage of pareto-fronts to ensure optimal results for a given set of parameters. E.g. a pareto-front can give the relation of an achievable purity as a function of the maximum yield possible for this purity. Thus, below a determined pareto-front feasible operating points are obtainable, while fictional non-reachable operating points are found above such limiting lines. Generally speaking, for this example, purity and yield of a target compound follow different trends. A higher supersaturation, e.g. due to a higher δ_J, leads to more crystal mass precipitating, however, more of the byproduct B crystallizes alongside the target product A. To determine the maximum possible value of purities $x_{i,Prod}$ and yields Y_i as a function of various process parameters $Par_{1,\dots,K}$, objective functions OF were defined to be minimized. The number of considered parameters is designated as K and can consists of parameters like evaporative factors δ, antisolvent factors ζ, energy requirements, etc.. These objective functions can be weighted, with a weighting factor $W_{i,F}$, considering specific goals for a given separation task. As an example, objective functions for purities and yields are given in Eqs. (4.55) and (4.56), respectively.

$$OF_1 = \sum_{i=A}^{B} \left[x_{i,Prod}^{real} - x_{i,Prod}^{th}(Par_{1,\dots,K}) \right]^2 \cdot W_{i,1} \tag{4.55}$$

$$OF_2 = \sum_{i=A}^{B} \left[Y_i^{real} - Y_i^{th}(Par_{1,\dots,K}) \right]^2 \cdot W_{i,2} \tag{4.56}$$

Where the *real* describes realistic/experimental values and *th* are theoretical values calculated by the simulation. For a completely predictive approach, for which no experimental data sets are available, the maximum value of purities and yields were chosen as optimal realistic values.

$$x_{i,Prod,max}^{real} = Y_{i,max}^{real} = 1 \tag{4.57}$$

This multi-objective optimization problem, described by the various objective functions, can be summarized into a single optimization equation $\overline{OF}$ as a function of considered parameters $Par_{1,\dots,K}$.

$$\overline{OF}(Par_{1,\dots,K}) = min\left(OF_1 + OF_2 + \dots + OF_F\right) \tag{4.58}$$

Where F is the total number of defined objective functions. Additional objective functions could incorporate energy balances to minimize energy requirements as well as non-quantitative decisions regarding crystallization strategies etc.. However, this work focuses on the objective functions given in Eqs. (4.55) and (4.56). To solve Eq. (4.58), the MATLAB® solver *fmincon* was utilized, since it allows for non-linear conditions to be specified. E.g. this can be used to set target purities or yields for specific separation problems.
For the calculations of the the purities $x_{i,Prod}$ the solvent-free molar fractions were used to account for the deposition of A and B from the mother liquid during drying of the products. In this case, A is purified in the solid, while B is purified in the liquid phase, respectively. Yield is defined as the amount of compound in the product phase compared to the maximum possible amount, which was supplied to the process as feed each cycle k.

$$x_{A,Prod} = \frac{x_{A,S,J=1}^{k_{end},(6)}}{x_{A,S,J=1}^{k_{end},(6)} + x_{B,S,J=1}^{k_{end},(6)}} \tag{4.59}$$

$$x_{B,Prod} = \frac{x_{B,L,J_{max}}^{k_{end},(6)}}{x_{A,L,J_{max}}^{k_{end},(6)} + x_{B,L,J_{max}}^{k_{end},(6)}} \tag{4.60}$$

$$Y_A = \frac{x_{A,S,J=1}^{k_{end},(6)} n_{S,J=1}^{k_{end},(6)}}{x_{A,S,Feed,J_{Feed}} n_{S,Feed,J_{Feed}}} \tag{4.61}$$

$$Y_B = \frac{x_{B,L,J_{max}}^{k_{end},(6)} n_{L,J_{max}}^{k_{end},(6)}}{x_{B,S,Feed,J_{Feed}} n_{S,Feed,J_{Feed}}} \tag{4.62}$$

4.3.2 Preliminary Sensitivity Study

The simulations, can be used to predict the behavior of crystallization processes and investigating the influences of different crystallization conditions, i.e. temperature, or strategies such as evaporative, cooling, antisolvent crystallization, etc.. For solid solutions, especially

continuous solid solution forming systems, the solid phase composition imposes additional influences on the efficiency of the separation. This work focuses on alyotropic continuous solid solutions of the L-valine / L-leucine system. Such systems inherently suggest the usage of different crystallization strategies/conditions, due to the shift in alyoptopic compositions as well as the change in the effective separation with changing conditions (E.g. see Figures 3.9 and 3.10). Hence, the ternary phase diagram of the L-valine /L-leucine system is divided in to two regions. Region I encompasses all compositions on the L-leucine -rich side of the alyotropic composition, while region II contains the L-valine -rich side regardless of solvent phase. A graphical depiction of this division is presented in Figure 4.11.

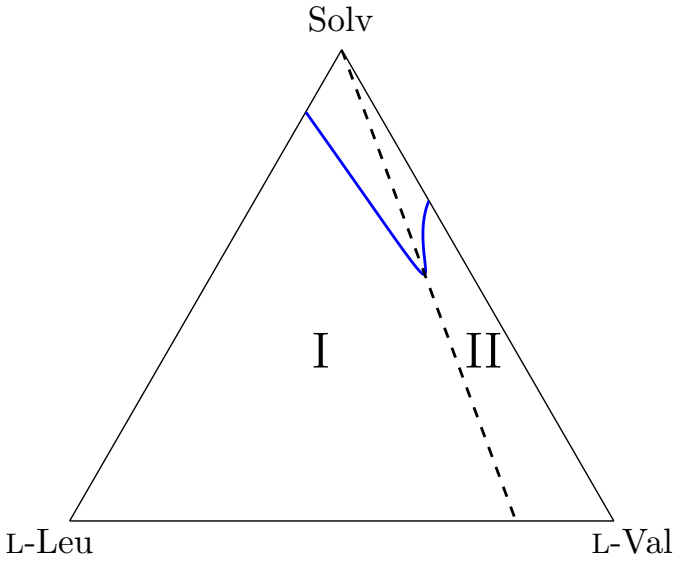

Figure 4.11: Illustration of the division of the ternary phase diagram into two regions for the L-valine /L-leucine system. Blue line: solubility line; dashed line: alyotropic composition; region I: L-leucine -rich side; region II: L-valine -rich side of the alyotrope.

Here, for each of these regions, an optimal crystallization strategy and temperature should be determined. While this is still a simplification and further division of these regions potential yields better results, this sections aims to show a heuristic approach to conceptionally design counter-current crystallization processes. For further systems or a more detailed optimization, division into more regions might be advisable.
For the two regions, defined in Figure 4.11, two initial compositions, of $w^{I}_{L-Leu,init} = 0.4$ and $w^{II}_{L-Leu,init} = 0.05$ were chosen as arbitrary feeds. These compositions were chosen since for all investigated solvent phases and conditions, they reside in their respective region regardless of the change of the alyotropic composition. To acquire acquire comparable results, a single stage crystallization with a purification of $\beta_L = 10° \mathrel{\hat{=}} \beta'_L = 0.\bar{1}$ (see Eqs. (4.13) and (4.14)) was simulated for evaporative and antisolvent crystallisation, using ethanol, isopropanol, or acetone as antisolvents, at 25 as well as 40 °C. Here, only

two temperatures were investigated, since overall temperature dependence of the system is relatively low (see Figure 3.10). Nevertheless, data sets at two different temperatures can be used to gain initial insight into possible trends. A low β'_L corresponds to a high purification and less amount which is crystallized, hence for low values of β'_L, low values of ζ are obtained. Due to the exponential decrease in effect of the antisolvent with increasing antisolvent amount, better comparison between various antisolvents is observable, since their changes in effect are more pronounced for lower ζ values. Alternatively, if just various antisolvents are compared, the ζ could be assumed to be constant and the resulting purification compared to determine the best antisolvent. This approach however, does not enable comparison to evaporation. Results of the simulation for the two regions are shown and interpreted in the following sections. Further, the model is validated for evaporative and antisolvent crystallization in Section **4.4.3** via pilot plant experiments.

Region I: $x_{L-Leu,init} > x_{L-Leu,Alyo}$

In region I, L-leucine is purified in the solid while L-valine is enriched in the liquid phase, due to the lower solubility of L-leucine when compared to the alyotrope. Figure 4.12 shows the resulting purities, yields, and effort in terms of antisolvent and evaporation factor for a crystallization of $\beta'_L = 0.\bar{1}$ at 25 °C.

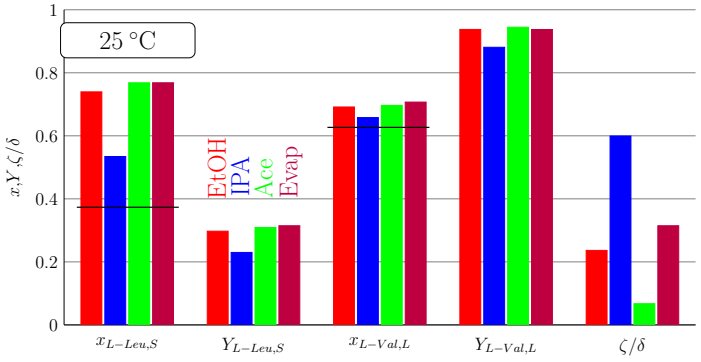

Figure 4.12: Recrystallization in region I of 0.4/0.6 wt.% L-leucine /L-valine with $\beta'_L = 0.\bar{1}$ at 25 °C for various crystallization strategies. Red: ethanol; blue: isopropanol; green: acetone as antisolvents, purple: evaporative crystallization; black line: initial composition.

At 25 °C, in terms of purity and yield, evaporative (purple) and antisolvent crystallization using acetone (green) exhibit the best separation. The worst performance is shown by using isopropanol (blue) as the antisolvent, which results in the lowest purification and lowest yields across the board, while requiring the most antisolvent as shown by the high value of ζ. This can be attributed to the lower efficiency of isopropanol as antisolvent as compared to acetone and the lower antisolvent purity after recycling, due to

lower azeotropic composition (see Section **4.4.2**). Ethanol (red) behaves comparably to acetone in resulting purities and yields, however, its values are slightly lower, while requiring an increased amount of antisolvent. Out of the antisolvents, acetone shows the best performance per amount of antisolvent added to the system. Evaporative crystallization exhibits similar performance to acetone with slightly higher purification and lower yields. The relative amount of water which needs to be evaporated is significantly higher than the amount of acetone required for a similar separation. The added antisolvent would be evaporated as well as to recycle the antisolvent which makes the values of δ and ζ comparable in this case. Here, even when the higher heat capacity and vaporization enthalpy of water is disregarded, less energy is required for the antisolvent crystallization at 25 °C. Figure 4.13 illustrates the results of the same separation efficiencies at 40 °C.

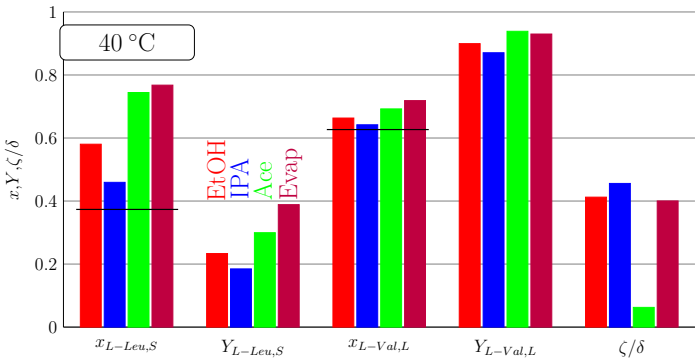

Figure 4.13: Recrystallization in region I of 0.4/0.6 wt.% L-leucine /L-valine with $\beta'_L = 0.\bar{1}$ at 40 °C for various crystallization strategies. Red: ethanol; blue: isopropanol; green: acetone as antisolvents, purple: evaporative crystallization; black line: initial composition.

Overall, a decrease of the separation efficiency of antisolvent crystallization can be observed. Additionally, more ethanol and acetone are required for said crystallization, while less isopropanol is needed. This decrease of efficiency is seen as a reasonable result since with increase in temperature the effective separation area in the distribution diagram is decreasing with increasing antisolvent and temperature content in region I (e.g. Figure 3.10). Further, separation using evaporative crystallization is slightly improved, due to the same reasoning of an increased effective separation at higher temperatures for region I as shown in Figure 3.7. However, all strategies (apart for using isopropanol) required a higher amount of antisolvent or evaporation of solvent. This can be explained with the increase of solubility with elevated temperature which requires more effort to crystallize a similar relative amount of solute from the liquid phase.
Overall, for region I, operating a crystallization at 25 °C, as opposed to 40 °C, improves the process efficiency. Additionally, a case could be made for using either antisolvent crystallization with acetone as a more energy efficient variant of the process or evaporative

crystallization, due to a simpler process design, while resulting in similar separation performance with higher energy demand. Another relevant topic, in this specific system, is the shift of the alyotropic composition towards the L-leucine-rich side during the antisolvent crystallization. If a process like the alyotrope separation, detailed in Section **4.4.4**, is desired, the alyotropic composition should remain mostly on the L-valine-rich side, which in this case would suggest using evaporative over antisolvent crystallization. It should be noted here, that in a real counter-current crystallization operating inside region I, different crystallizer could operate using either evaporative and antisolvent crystallization, thus combining the advantages of allowing for alyotrope separation while reducing energy requirement as much as possible. Nevertheless, for simplicity's sake of the proof of concept in Section **4.4.4**, only evaporative crystallization at 25 °C was chosen for region I.

Region II: $x_{L-Leu,init} < x_{L-Leu,Alyo}$

For region II, in which separation occurs between pure L-valine and the alyotropic composition, the same investigation was performed. Again, a purification of $\beta'_L = 0.\bar{1}$ was used for all crystallization strategies at all conditions. Figure 4.14 showcases the results, which were obtained by the simulation for 25 °C.

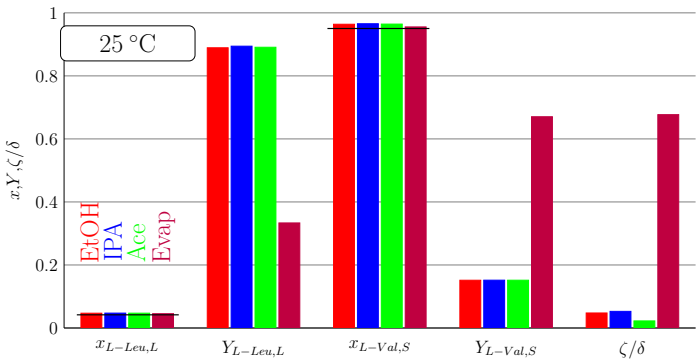

Figure 4.14: Recrystallization in region II of 0.05/0.95 wt.% L-leucine/L-valine with $\beta'_L = 0.\bar{1}$ at 25 °C for various crystallization strategies. Red: ethanol; blue: isopropanol; green: acetone as antisolvents, purple: evaporative crystallization; black line: initial composition.

Overall, only low purification is observed for all crystallization strategies when compared to region I. Since, in the L-valine/L-leucine system, the alyotropic composition is rather close the pure L-valine, roughly at 88 *wt.*% L-valine, the differences in solubility on the borders of region II are quite small. This leads to a small effective separation area between the equilibrium and 45° line in the distribution diagramm as seen in e.g. Figures 3.9 and 3.10, and therefore a low separation efficiency. Additionally, in region II, L-valine is purified in the solid phase, due to the lower solubility.

In terms of purification in this region, using different antisolvents results in comparable purities and yields, regardless of the antisolvent chosen. Again, due to the largest antisolvent effect, the least relative amount is needed when using acetone as antisolvent. Evaporative crystallization performs much worse in this region when compared to antisolvent crystallization. As shown in Figure 3.9, for the case of ethanol, adding antisolvent shifts the alyotropic composition towards the L-leucine-rich side and increases the relative solubility difference between L-valine and the alyotrope. In distribution diagrams, this leads to an increased separation area. For pure water as a solvent, this shift does not occur and thus, only a small area is obtained, which results in poor separation performance. To achieve the given separation task with $\beta'_L = 0.\bar{1}$, a large amount of the solvent needs to be evaporated, followed by low enrichment in the respective phases.
The influence of temperature can be gauged by the data set for 40 °C, depicted in Figure 4.15. Similarly, the overall separation performance is rather low and does not change significantly from 25 to 40 °C. However, for antisolvent crystallization, more antisolvent is requried to achieve similar purification. This can be attributed to the increased residual solubility of the solutes in the water/antisolvents mixtures, which requires more antisolvent to achieve comparable supersaturations when compared to lower temperatures. Interestingly, the separation performance of evaporative crystallization seems to be improved in region II for increased temperatures, since a lower amount of solvent needs to be evaporated. Due to the increase in temperature the alyotropic point is shifted towards the L-leucine-rich side, which leads to a larger solubility difference between L-valine and the alyotrope, which again leads to an increase separation area and improved separation. While the increase in residual solubility increases significantly for water/antisolvent mixtures, the temperature influence seems to be less pronounced in pure water, and thus, no additional solvent needs to be evaporated to obtain similar purification.

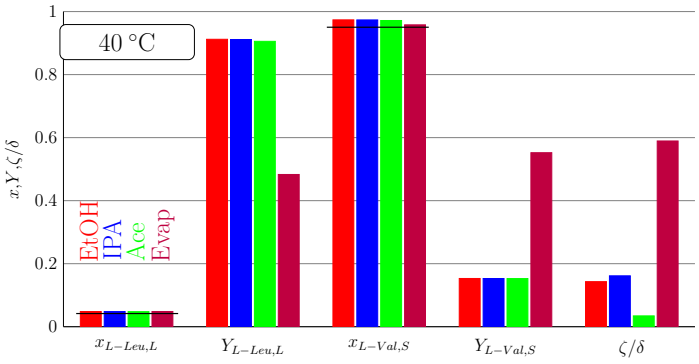

Figure 4.15: Recrystallization in region II of 0.05/0.95 wt.% L-leucine/L-valine with $\beta'_L = 0.\bar{1}$ at 40 °C for various crystallization strategies. Red: ethanol; blue: isopropanol; green: acetone as antisolvents, purple: evaporative crystallization; black line: initial composition.

Nevertheless, for region II, the most efficient crystallization strategy out of the investigated cases, is antisolvent crystallization using acetone as the antisolvent at 25 °C. While acetone was used in this work for optimal simulation results, for experiments at pilot plant scale, ethanol was used, due to better manageability. More information on this are given in Section **4.4**.

4.3.3 Conclusions of the Simulation Study

Results of process simulations, with the model described in Section **4.2**, were introduced in Section **4.3**. Section **4.3.1** explained the determination of relevant process parameters in a first optimization approach. Further, a sensitivity analysis was performed in Section **4.3.2** to gain insight into the effects of different temperatures and crystallization strategies for different compositions of L-valine /L-leucine . For this, the phase diagram was divided into two regions (see Figure 4.11), one on each side of the alyotrope. The sensitivity analysis resulted in a favorable temperature of 25 °C for both regions. This is due to the low overall temperature dependency of the model system and slightly more efficient separation at lower temperatures. Out of the investigated crystallization strategies, antisolvent crystallization with acetone as antisolvent yielded the best results. However, since in region I, evaporative crystallization is competitive and allows for the separation of alyotropic compositions (see Section **4.4.4**), it is recommended for this region.
In this study, only one crystallization strategy was investigated per region. Also, only product purities and yields were taken into account, while process complexities, energy demands, etc., were not regarded for. Thus, this work focuses on developing conceptual design heuristics of counter-current crystallization, for which only crude optimizations were utilized. More complex approaches were outside the scope of this work, but should be explored in greater detail in future works.
In the following sections, the pilot plant utilized for experimental validation runs is introduced and the experiments performed are discussed.

4.4 Experimental Part

This section explains the experimental equipment and procedure related to counter-current crystallization. Firstly, the pilot plant equipment will be described in detail in Section **4.4.1**. The process models (see Section **4.3**) are validated with experimental runs in Section **4.4.3** and an additional process variant to separate partial solid solutions as well as alyoptropic mixtures is given in Section **4.4.4**.

4.4.1 Pilot Plant

Realising a counter-current crystallization in a pilot plant scale imposes various challenges towards the process equipment. The setup needs to be able to utilize various crystallization strategies and the ability to recycle used streams. Additionally, a efficient solid-liquid separation has to be implemented. In 2013, Hapila GmbH (Gera, Germany) patented a counter-current crystallization plant design as the HAPIpur® process, which included a multistage crystallizer cascade capable of enriching compounds to high purities [98]. The proposed process, based on evaporative and cooling crystallization, allowed for simultaneous mostly automatic operation of all crystallizers. Additionally, by redirecting liquid streams in specific order, solid phase transport can be substituted. A flow scheme of this design is given in Figure 4.16.

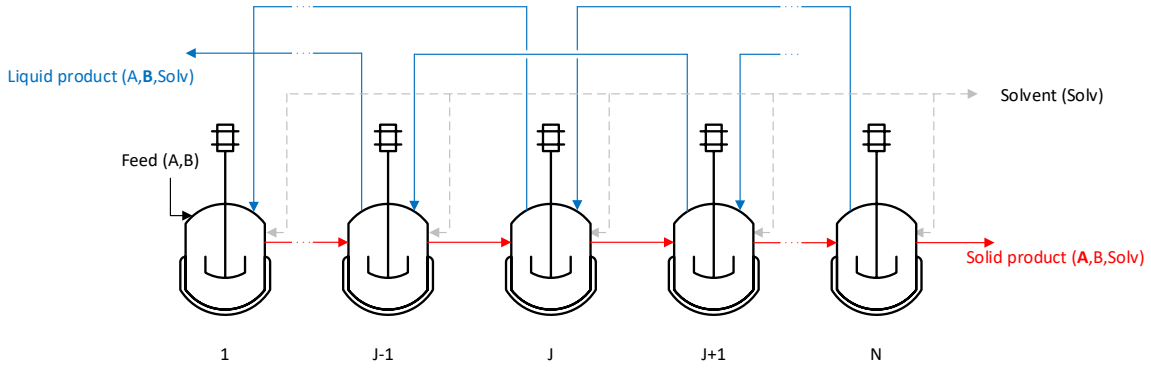

Figure 4.16: Simplified flow scheme of the HAPIpur® process. Blue lines: mother liquor streams; red lines: solid/dissolved streams; dashed gray line: solvent streams. Inspired by [98]

Figure 4.16 illustrates a N-stage counter-current crystallization for the separation of A and B. In this configuration, the solid phase transport is avoided by dissolving the solids in its corresponding liquid phase regarding the counter-current scheme. E.g. the solid phase, which needs to be transported from crystallizer $J-1$ into J is mixed with the liquid phase moving from $J+1$ inside $J-1$. Additionally, enough solvent is added to completely dissolve the remaining solid, after which, the now liquid mixture is transported into crystallizer J. Hence, the solid is transported one crystallizer forward as a dissolved mixture, while the liquid phase is subsequently pumped back two and one crystallizers forward. The target compound A is obtained in crystallizer N as a solid product, while liquid product, enriched in B, is withdrawn from the second crystallizer of the cascade. In vessel 1, no crystallization occurs, since its only purpose is complete dissolution of the feed.

For the pilot plant at the Max Planck Institute (MPI) Magdeburg, the described concept was implemented in a more flexible manner, suited for research purposes where flexible

changes to the equipment, conditions and systems are desirable. A simplified flow sheet of this pilot plant is illustrated in Figure 4.17, while a detailed piping and instrumentation diagram is given in Figure A.4, including all denotations of vessels and valves used below.

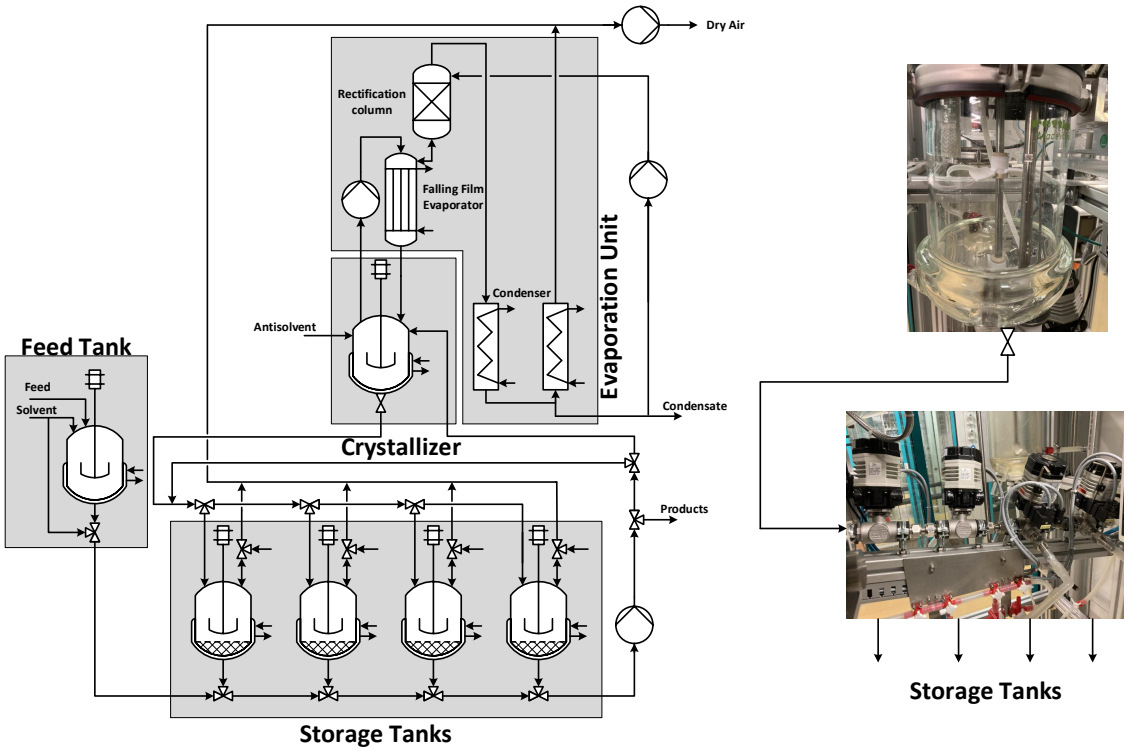

Figure 4.17: Left: simplified flow scheme of the counter-current crystallization pilot plant at the MPI Magdeburg. Right: pictures of the main crystallizer and the valve cascade.

In the the pilot plant, the various separation vessels given in Figure 4.16, are substituted by storage tanks in the lower section of the plant. All crystallizations are performed in a single central crystallizer. Since only one crystallizer is used in this more compact design, in-situ measurement equipment such as an ultrasonic probe, speed of sound and conductivity probes, etc., are only required once as well. Additionally, using a valve cascade below the crystallizer, this core vessel is connected to all storage tanks, which are themselves connected to each other. The storage tanks are equipped at their bottoms with filter plates to enable in-tank solid-liquid separation. This allows the plant to be operated in different modes, i.e. fractional, co- and counter-current crystallization. This offers more flexibility to design efficient processes for a given specific separation task. A challenging example will be described in Section **4.4.4**. Further, the main crystallizer is connected to an evaporation unit consisting of a falling film evaporator and a rectification column, which are used for evaporative crystallization and for antisolvent recycle. To aid in evaporation, the vessels can be subjected to vacuum. During this work, the pilot plant was extended with a rectification column and an automated reflux to enable the separation

and recycle of various antisolvents.
While in the HAPIpur® process (see Figure 4.16), the solid phase transport is avoided by dissolving the solids in solvent prior to transportation, the adapted pilot plant follows a similar but distinctly different strategy. Here, since the plant allows for flexible operation due to the interconnected crystallizer and storage tanks, it can be operated similar to simulated moving bed chromatography [13]. A schematic representation of simulated moving bed operation for counter-current crystallization is given in Figure 4.18.

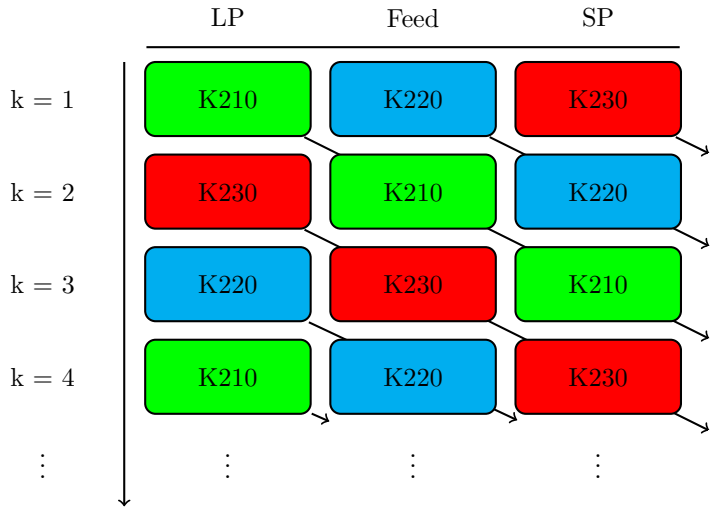

Figure 4.18: Visualization of the simulated moving bed principle for the counter-current crystallization pilot plant for an example of three stages operated at steady state. K210/K220/K230 designate several storage vessels (see Figure A.4). LP: liquid product; SP: solid product.

Figure 4.18 illustrates the roles and positions of a three stage counter-current crystallization ($J_{max} = 3$) using the simulated moving bed to avoid solid phase transport. Here, in the first crystallization cycle, $k = 1$, the three vessels $K210$, $K220$, and $K230$, have the roles of liquid product "LP", feed "$Feed$", and solid product "SP", respectively, analogue to Figure 4.4 (right). At the end of cycle $k = 1$, the solid and liquid phases need to be separated and transported according to the counter-current scheme. As an example, the cycle for vessel $K210$ will be described. The liquid phase is withdrawn from vessel $K210$ via the filter plate as the liquid product and taken out of the plant. The remaining solid phase in vessel $K210$ needs to be contacted with the liquid phase from vessel $K230$ according to the counter-current scheme. Therefore, the liquid phase of vessel $K230$ is filtered and pumped into vessel $K210$ complimented by additional solvent, enough to completely dissolve the suspension. In the HAPIpur® process, the solution is then pumped into the next crystallizer. This is not required here, since all storage tanks are interconnected and thus, just the role of vessel $K210$ can be changed in cycle $k = 2$ from "LP" to "$Feed$".

This eliminates the need for an additional pumping step. This change of roles can be simultaneously performed for all other tanks analogously, following the scheme given in Figure 4.18.

An extended description of implementing a crystallization cycle for vessel $K210$ as "LP", including operation of valves, pumps, etc., is given below. All sections shown in Figure 4.17 are shown in greater detail in Figure A.4.

To start an initially empty pilot plant, a predicted steady state is calculated using the process model described in Section **4.2**. Suitable initial masses and compositions are then prepared for the plant. For this, the specific initial amounts of L-valine , L-leucine , and water are given into the feed vessel $K300$ and homogenized until complete dissolution using stirrer $M300$. Upon dissolution, the solution is transported towards the main crystallizer $K100$ by opening valves $MV300$, $HV301$, and $HV302$ and activating pump $P300$. Valves $MV201$ to $MV231$ at the bottom of the storage vessels $K200$ to $K230$ remain closed toward the tanks. Here, the prefixes MV and HV denote hand (manual) and motorized valves, respectively. After the solution is completely transported to crystallizer $K100$, $HV302$ is closed towards the crystallizer. In crystallizer $K100$, the solution is stirred via $M100$, temperated with thermostat $HX100$ and thermocouple $TIC100$, while $PIC100$, $CI100$, and $XI100$ measure pressure, conductivity, and speed of sound, respectively. To achieve supersaturated, vessel $K100$ can be cooled via $HX100$, antisolvent can be added manually, or water is evaporated with the falling film evaporator. For this, solution from vessel $K100$ is pumped by $P310$ to the top of the evaporator, which itself is heated to ~ 80 °C and monitored with $HX300$ and $TI120$. To aid the evaporation, $P110$ is used to create vacuum at 200 $mbar$. The distillate is condensed via total condensers, cooled by $HX110$, and collected in the distillate vessel $K110$, which's weight is monitored via $WI100$ to obtain the evaporated mass and its rate. To control crystallization and avoid spontaneous nucleation, an ultrasonic probe $U100$ is activated periodically, usually for one minute every five minutes.

After the desired amount of supersaturation is reached, and the suspension is homogeneous, it is transported to its corresponding storage tank, e.g. vessel $K210$. Thus, $MV100$ and $KV210$ are opened. Due to gravity, the suspension flow towards the storage tank. To avoid, residual solids in vessel $K100$ and the connecting tubes, $MV211$, $HV301$, and $HV302$ are opened and the mother liquor is continuously filtered and pumped to vessel $K100$ with $P300$ until no remaining solid phase can be observed in vessel $K100$. Additionally, the transported mass is observed via weighting bars $WI100$ and $WI210$. Following the transport, all valves of vessel $K210$ are closed and the suspension is stirred and heated to equilibration temperature by $M210$ and $HX210$, respectively. This procedure is done for the other tanks analogously.

After equilibration the solid and liquid phases were sampled and analyzed off-line via HPLC and PXRD. If no antisolvent was used, vessel $K210$ contains the "LP", the liquid

phase is withdrawn, via the filter plate, by creating suction via pump $P300$ by opening $MV211$, $HV301$ as well as $HV213$, to avoid vacuum, and taken out of the plant. Again, the removed weight is recorded via $WI210$. The residual solid phase in vessel $K210$ is mixed with the liquid phase of vessel $K230$ (see Figure 4.18), by opening $MV231$, $HV301$, $HV302$ towards the valve cascade, and $KV210$ and starting pump $P300$. Utilizing the same connections, after $MV231$ is closed, an undersatured L-valine /L-leucine solution, for complete dissolution, is supplied to vessels $K210$ from $K300$ during which the role of vessel $K210$ switches to "$Feed$" according to Figure 4.18. After, which $KV210$ is closed, $MV211$ opened, and $HV302$ switched towards vessel $K100$ to pump the solution back into the crystallizer for the next cycle .

If it was the goal to perform antisolvent crystallization, before the liquid phases can be withdrawn or reused, the antisolvent, here ethanol, needs to be removed. For this, the liquid phases are pumped into vessel $K100$ using $P300$ and the corresponding valves as described above. In vessel $K100$, the falling film evaporator is again used to evaporate the ethanol from the water and collected in vessel $K110$. For this, $P110$ was used to create a vacuum of 300 $mbar$, the evaporator was set to 70 °C. A rectification column above the evaporator improves separation efficiency and, if needed, $P121$ can be controlled by $TIC121$, supplying a small reflux stream to control a set temperature (here: 51 °C) at the top of the column. The top and bottom temperature levels in the pilot plant for water/ethanol separation were chosen based on data sets reported in [99], and resulted in a purity of the recycled ethanol of $\sim$ 85 $wt.\%$. Its purity was determined off-line via densimetry, while HPLC was utilized to validate the assumption, that no significant amount of L-valine and L-leucine were found in the distillate. The product purity could be further optimized by investigating process parameters like temperatures and pressure. However, as a proof of concept, in this work it was assumed that 85 $wt.\%$ was sufficient. Additional information on the antisolvent recycle is given in Section **4.4.2**. The removed antisolvent can be withdrawn from the plant with $P121$ via $HV120$ and is typically reused in the next crystallization cycles.

4.4.2 Antisolvent Recycle

If antisolvent crystallization is utilized, as described in Section **4.4.1**, the antisolvent is removed from the liquid phase after equilibration via evaporation. To achieve a more sustainable process, the removed antisolvent needs to be recycled and reused in future crystallization cycles. This is evaluated in the process simulations in the parameter R_{Anti} as well as in the definition of ζ in Eq. (4.45). Practically, some issues may occur if the antisolvent cannot be easily separated. This is especially true, if the solvent/antisolvent system forms an azeotrope, as it is the case for water/ethanol, which was used in pilot plant experiments in this work. In such cases, the ethanol either has to be further purified, e.g.

via pressure swing rectification [100], or recycled and reused as an impure ethanol/water mixture. In this work, the later method was chosen, due to simpler process equipment and lower energy requirements. Even though Eq. (4.45) is able to consider recycling impure antisolvents, this approach has major influences on the separation efficiency of the counter-current crystallization process, as exemplified in Figure 4.19.

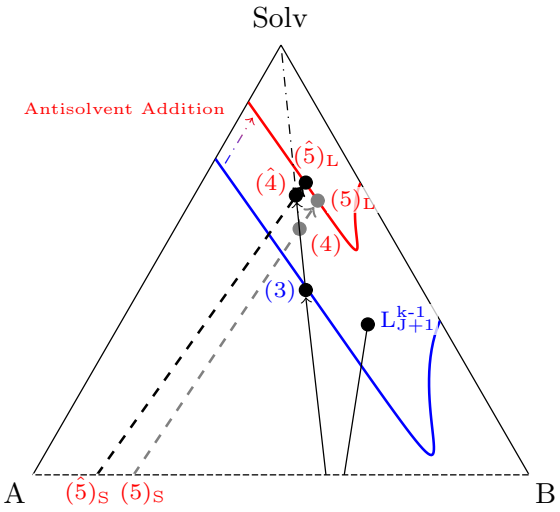

Figure 4.19: Zoomed view of the (pseudo-)ternary phase diagram of antisolvent crystallization using impure antisolvent. **(3)**: dissolution; **(4)**: antisolvent addition; **(5)**: crystallization with pure (grey) and impure antisolvent (black, ($\hat{\square}$)). Blue: solubility line of pure solvent; red: solubility line of solvent/antisolvent mixture; arrows: process pathways; dashed line/arrows: tie line/process pathways along tie line; dashdotted lines: constant A:B ratio.

Figure 4.19 shows the differences in using pure or impure recycled antisolvents for a constant value of the parameter ζ. Up to and including the complete dissolution in substep **(3)**, the substeps are not directly influenced by the purity of the antisolvent. Substeps **(4)** and **(5)** (shown by gray process pathways) illustrate the supersaturation and crystallization using pure antisolvent. Due to the solvent/antisolvent mixture in the recycled antisolvent, its effectiveness is decreased and more antisolvent mixture is required to reach a specific value of ζ when compared to pure antisolvent. Since overall, more solvent per solutes is present in the crystallizer, the overall supersaturation becomes reduced (see $\hat{\mathbf{4}}$). This results in a crystallization along the black dashed tie line of $\hat{\mathbf{5}}$. Comparing the gray and black tie lines for crystallization with pure and impure antisolvent, respectively, it is observed, that pure antisolvent leads to increased crystallization of the solid phase due to higher supersaturation. However, this is connected to a higher purification of target compound A in the solid phase for $\hat{\mathbf{5}}_\mathbf{S}$ than $\mathbf{5}_\mathbf{S}$. In terms of the introduced purification grade β_L', for impure recycled antisolvent $\hat{\beta}_L'$ possesses a smaller value as $\beta_L'^{pure}$ for pure antisolvent, while $\zeta^{pure} = \hat{\zeta}$ is constant, which results in a constant solubility line (see red line in Figure 4.19).

4.4.3 Experimental Validation of the Process Model

To validate the aforementioned predictive process simulation, given in Section **4.3**, several experimental runs have been conducted in the pilot plant. For this, only evaporative and antisolvent crystallization were considered, since only a minor temperature dependency was observed in this system (see Section **3.3**). The investigated experiments and simulations are listed in Table 4.1.

Table 4.1: Performed experimental and simulation runs. All experimental runs were performed at pilot plant scale at 25 °C. *: only simulation.

Run No.	Strategy	J_{max} (J_{Feed})	Feed [wt.%] L-Leu/L-Val	Antisolvent
Run 1	Evaporation	3 (2)	40/60	n.a.
Run 2	Antisolvent	3 (2)	40/60	Ethanol
Run 3	Evaporation	1 (1)	15/85	n.a.
	Antisolvent	1 (-)	n.a.	Ethanol
Run 4*	Evaporation	3 (3)	25/75	n.a.
	Antisolvent	2 (-)	n.a.	Acetone
Run 5*	Evaporation	3 (3)	25/75	n.a

Firstly, due to inherently low purification in region II (see Figure 4.11), the validations for both strategies were performed in region I (Runs 1 and 2). For each run, a three-stage counter-current crystallization ($J_{max} = 3$) was conducted, where feed, with a composition of 40/60 wt.% L-leucine /L-valine was supplied to stage $J_{Feed} = 2$.
Further comparison between experimental and predicted data sets in region II are given in Runs 3, 4, and 5 in Section **4.4.4** within an own chapter, due to the increased complexity of the alyotrope. Run 3 acts as a proof of concept of the proposed alyotrope separation with one stage for each strategy. The feed (15/85 wt.% L-leucine /L-valine) was chosen to be within region I and close to the alyotropic composition (13/87 wt.% L-leucine /L-valine) in water at 25 °C.
The simulated Runs 4 and 5 give insight about the improvement of the counter-current crystallization by implementing the alyotrope separation as opposed to an approach based on solely evaporative crystallization. Acetone was chosen as a more efficient antisolvent than ethanol, following Section **4.3.2**. A three-stage cascade using evaporative crystallization was combined with a two-stage version using antisolvent crystallization. For both runs, a feed of 25/75 wt.% L-leucine /L-valine was provided in stage 3.
Runs 1, 2, and 3 were experimentally conducted in the aforementioned and discussed pilot plant. For this, at least three crystallization cycles were performed for each run to ensure a

steady state was maintained. Each cycle required slightly more than one week of work due to the relatively long equilibration time of 72 h, solvent and/or antisolvent evaporation, filtration of product crystals, preparing and clearing the equipment, and off-line analysis. The validation experiments for Run 1 and 2 were performed as a three-stage counter-current crystallization run ($J_{max} = 3$) at 25 °C with feed being supplied in $J_{Feed} = 2$ (see Figure 4.16). In case of antisolvent crystallization, ethanol was used as the antisolvent, due to improved handleability and safety concerns over the more efficient acetone. For this, ethanol was recycled as impure antisolvent as described in Section **4.4.2**. To ensure complete equilibration after crystallization, the suspensions were stirred at constant temperature for at least 72 h before sampling and phase separation. As described previously, the liquid and solid phases were analyzed via HPLC, while the solid phase was additionally analyzed by PXRD measurement. Samples were taken after complete dissolution **(3)** as well as after crystallization **(5)** (e.g. see Figure 4.19).

Table 4.2: Process parameters describing the counter-current crystallization performed for evaporative and antisolvent crystallization (see Runs 1 and 2 in Table 4.1). Left column: predicted steady state parameters δ and ζ of the process model determined via Eq. (4.58); right column: corresponding experimental values. β'_L calculated via Eq. (4.14).

	Simulation			Experiments		
	Run 1: Evaporative Crystallization					
	LP	Feed	SP	LP	Feed	SP
δ	0.2319	0.5097	0.3504	0.2292	0.5092	0.3492
β'_L	0.0781	0.2780	0.2626	0.0554	0.2901	0.6348
	Run 2: Antisolvent Crystallization					
	LP	Feed	SP	LP	Feed	SP
ζ	0.2970	0.2433	0.3066	0.3648	0.2461	0.3103
β'_L	0.0272	0.1105	0.2321	0.0205	0.1816	0.6043

Both process variants (Runs 1 and 2) were optimized using Eq. (4.58) to maximize yields Y_{L-Val} and Y_{L-Leu} for $x_{L-Leu,Prod} \geq 0.98$. For this, only the objective function given in Eq. (4.56) was used without any weighting. The simulation was scaled to a maximum volume of two liters in a given crystallizer. This maximum volume is determined by the substep at which the highest liquid volume is in the crystallizers. For evaporative crystallization, this occurs after complete dissolution and before solvent evaporation **(3)**, while for antisolvent crystallization it is after the addition of antisolvent **(4)**. Table 4.2 lists the optimized values of the evaporation factor δ, the antisolvent factor ζ, and the purification grade β'_L for both strategies. Additionally, parameters resulting from performed experiments are given as well and will be discussed below, in conjunction with the respective

diagrams for the two strategies.
Based on the optimized simulation parameters given in Table 4.2, a counter-current crystallization was prepared as steady state and performed in the pilot plant. The experimental runs were conducted for three crystallization cycles to ensure no significant deviation from the calculated steady state occurred. Figure 4.20 illustrates ternary phase diagrams gathered for evaporative crystallization. Solid lines depict experimental results, while results from the simulation are shown as dashed lines. Different colors describe different stages inside the crystallizer cascade; blue: SP; grey: $Feed$; red: LP. Overall, the predicted tie lines are matched well by the experimental data sets, while SP shows the highest overestimation by the simulation. Additionally, compositions at various operating substeps are well described by the simulation. Here, the largest inaccuracy is found for the composition of the completely dissolved state (substep **(3)**) of LP.

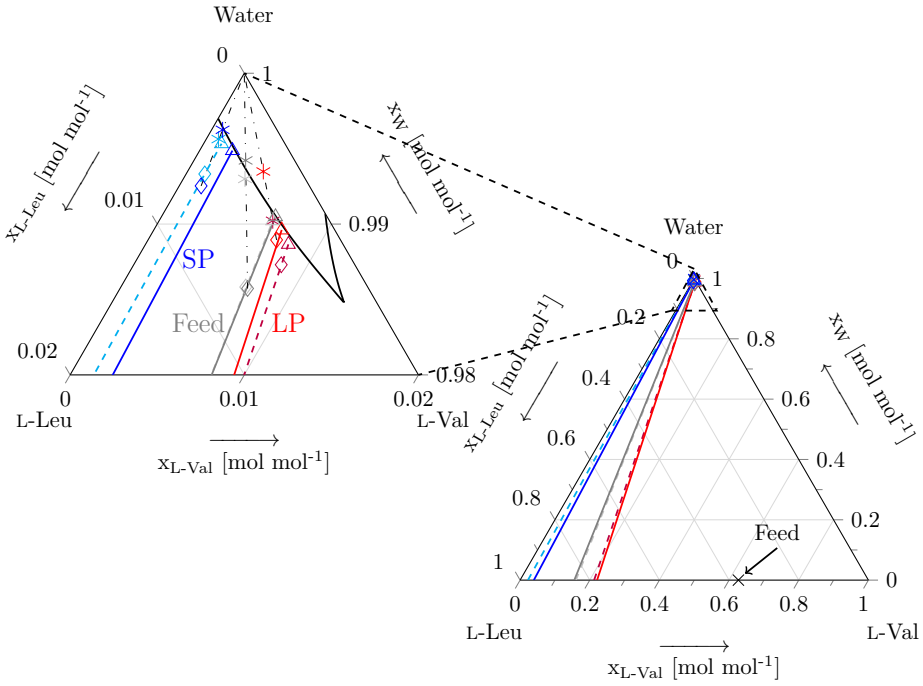

Figure 4.20: Ternary diagram of the validation evaporative crystallization (Run 1) in the pilot plant (lines) and simulation (dashed lines). Solid curved line: solubility line calculated with Eq. (2.40), dashdotted lines: isopleth lines; red: LP; gray: $Feed$; blue: SP; $*$: dissolved and $\diamond$: metastable state; $\triangle$: equilibrated liquid phase.

The deviation of substep **(3)** for all crystallizers can be explained by how the pilot plant is operated. As mentioned in Section **4.2**, the simulation calculates the exact amount of water necessary to dissolve the solutes. In real experiments however, water was added in excess to aid in the dissolution, which results in lower solute fractions in the phase diagrams. The excess water was evaporated during substep **(4)** in addition to the desired amount which was predicted by the simulation. When comparing the values of δ in

Table 4.2, the experiments were conducted to high accuracy regardless of the additional solvent.
Similarly, the effectivenesses of LP and $Feed$ are in good agreement with the predicted values, however, for SP the crystallization exhibits a large deviation. Figure 4.21 depicts the process and these purifications in the distribution diagram. Again, LP and $Feed$ are described well by the simulation, in this representation.

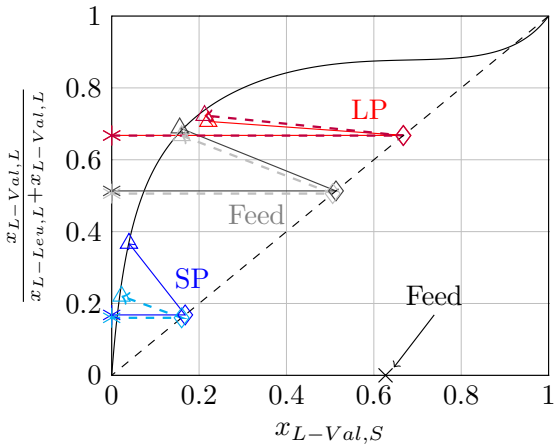

Figure 4.21: Distribution diagram of the validation evaporative crystallization (Run 1) in the pilot plant (lines) and simulation (dashed lines). Solid curved line: equilibrium line calculated with Eq. (2.40), red: LP; gray: $Feed$; blue: SP; $*$: dissolved and $\diamond$: metastable state; $\triangle$: equilibrated liquid and solid phases.

Due to the higher solid purification effectiveness of LP, the solid phase is favored in the purification, while the liquid phase composition is only enriched slightly. In $Feed$, while the solid phase is still favored, the liquid phase is enriched more substantially. In analogue, to the deviation in β', SP also shows a significant mismatch of the data sets. This results from the almost vertical equilibrium line in this region, which leads to large changes in liquid for small composition changes in the solid phase and therefore to significantly increased values of β'. Figure 4.22 depicts the ternary diagrams for an analogous process using antisolvent, in this case ethanol, crystallization.
Here, three additional solubility lines are illustrated, due to three different water/ethanol mixtures present in the various stages. SP and LP, both with a ζ value of ~ 0.3, shows similar solubilities, while in $Feed$ a higher solubility is observed for $\zeta \approx 0.24$. It should be noted, that for LP, in the experiments a higher value of ζ was obtained, however, with increasing antisolvent content, the antisolvent efficiency decreases and the deviation is less significant. This is seen as well, when comparing the simulated and experimental data sets for LP, with both resulting in low β'. Overall, the prediction for antisolvent crystallization shows comparable accuracy to evaporative crystallization.

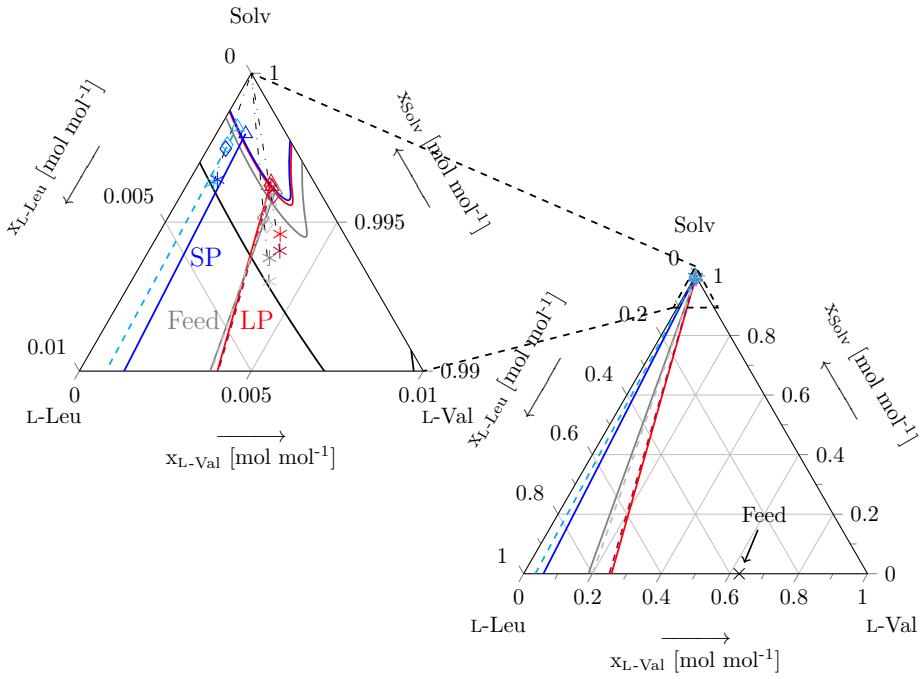

Figure 4.22: (Pseudo-)ternary diagram of the validation antisolvent crystallization (Run 2) in the pilot plant (lines) and simulation (dashed lines). Solid curved line: solubility lines calculated with Eq. (2.42); dashdotted lines: isopleth lines; black: water; red: *LP*; gray: *Feed*; blue: *SP*; ∗: dissolved and ⋄: metastable state; △: equilibrated liquid phase.

Feed and *LP* are predicted with high accuracy, while *SP* shows large deviation in β', due to the small purification in the solid phase, with a large change in solvent-free liquid phase composition. Therefore, similar trends are observed in the distribution diagram of the antisolvent process in Figure 4.23. Due to different water/ethanol mixtures, three additional equilibrium lines are observed.

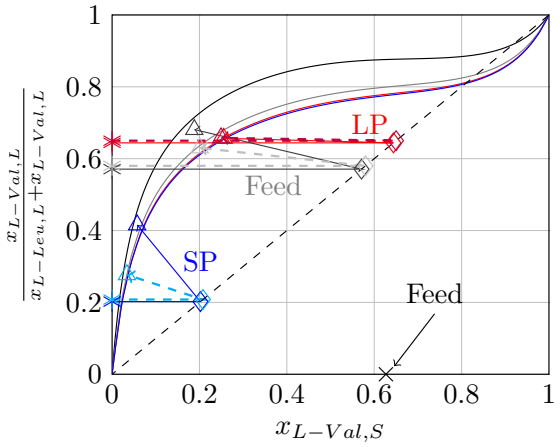

Figure 4.23: Distribution diagram of the validation antisolvent crystallization (Run 2) in the pilot plant (lines) and simulation (dashed lines). Solid curved line: equilibrium lines calculated with Eq. (2.42); black: water; red: *LP*; gray: *Feed*; blue: *SP*; ∗: dissolved and ⋄: metastable state; △: equilibrated liquid and solid phases.

In addition to the deviation of SP, the experimental data set of $Feed$ does not align well with the predicted equilibrium line (gray) and shows slightly higher purification in the solid and liquid phases than expected. The other experimental data sets align reasonably well with the predetermined equilibrium lines for their respective mixtures.
Besides the comparison between experimental and simulation data sets, a comparison between evaporative and antisolvent crystallization is possible. In Section **4.3.2**, for region I, it was predicted that, at 25 °C, either evaporation or antisolvent crystallization, using acetone, might be efficient. However, using ethanol as antisolvent, showed worse results than evaporative crystallization. Table 4.3 lists predicted and measured product purities and yields for both process variants.
The predicted and experimental values generally agree well with each other for both crystallization strategies, except for the yield of L-leucine for evaporative crystallization. Here, the experimental value of $Y_{L-Leu} = 0.7100$ is much higher than the expected 0.3604. This result is seen as unreasonably high and may result from additional solid phase which accumulates inside tubings of the plant from previous crystallizations or excessive amounts of residual moisture, which was not properly removed by filtration and washing prior to drying.

Table 4.3: Purities and yields of the counter-current crystallization performed for evaporative and antisolvent crystallization (see Runs 1 and 2 in Table 4.1). Left column: predicted steady state results of the process model based on parameters given in Table 4.2; right column: corresponding experimental values.

	Simulation		Experiments	
	Run 1: Evaporative Crystallization			
	L-Val	L-Leu	L-Val	L-Leu
$x_{i,Prod}$	0.7232	0.9775	0.7067	0.9646
Y_i	0.9951	0.3604	0.9170	0.7100
	Run 2: Antisolvent Crystallization			
	L-Val	L-Leu	L-Val	L-Leu
$x_{i,Prod}$	0.6569	0.9661	0.6563	0.9426
Y_i	0.9955	0.1240	0.9728	0.1594

Additionally, the yield of L-valine is reduced, which ultimately leads to an increased amount of solid phase in SP. For the antisolvent crystallization, the yield of L-leucine is increased as well, which could also be explained by this. However, due to smaller deviation, this value is seen as reasonable. Nevertheless, overall, the experimental results were well predicted by the simulation and therefore, the simulation is seen as validated for region I for both evaporative and antisolvent crystallization. An experimental validation of region II for antisolvent crystallization, again using ethanol, is given in Section **4.4.4**.

Further, both data sets agree with the hypothesis, that evaporative crystallization is more efficient in this region. For antisolvent crystallization, purification in LP is impacted additionally by the shifted alyotropic point (see Figure 3.9) when using ethanol. This leads to an inefficient purification stage in terms of liquid phase composition change and crystal mass precipitation, as seen in Figures 4.22 and 4.23.

4.4.4 Alyotrope Separation

Solubility data sets, given in Section **3.3**, determined for the studied system a shift of the alyotropic composition with changing temperature and changing solvent composition. A similar shift of the double saturation point, observed in partial solid solutions (see Figure 2.9), with temperature is described in [19, 20]. Here, one component was purified at a lower temperature using multistage crystallization until the liquid phase composition was close to the double saturation point. Then, the temperature was increased to change the phase behavior of these ternary systems to a point, where the given composition now lies within the solid solution region on the other side of the double saturation point. Analogue to this, shifting the alyotrope, by changing temperature or solvent composition, allows a operating point to be changed from being within region I into region II, according to their definition in Section **4.3.2**, which can be exploited to separate alyotropic solid solutions to high purites. A comparable shift in partial solid solutions was performed with temperature in literature [19, 20]. Since the continuous solid solution L-valine /L-leucine system shows low temperature dependency regarding solubility, an isothermal proof of concept at 25 °C using antisolvent crystallization was performed during this work and initially published in [1]. Using antisolvent crystallization additionally allows the process to be applicable for thermally sensitive and temperature independent systems. Figure 4.24 illustrates the process pathways for the proposed alyotrope separation process.
The process, illustrated in Figure 4.24, possesses the same substeps as the general antisolvent crystallization of solid solutions, which is shown in Figure 4.9, and is completely identical until substep **(4)**. Starting in region I, a saturated aqueous solution **(3)** is mixed with antisolvent to reach a supersaturated composition **(4)**. However, since this process operates close to the alyotrope, by adding the antisolvent, the alyoptropic composition is shifted over the current composition **(4)**, which now resides in region II on the B-rich side of the alyotrope. Therefore, during crystallization, B instead of A is enriched in the solid phase as the compound which is purified in the respective phases is switched upon changing the regions. The resulting solid phase can now be further purified by classical counter-current crystallization to acquire almost pure B.

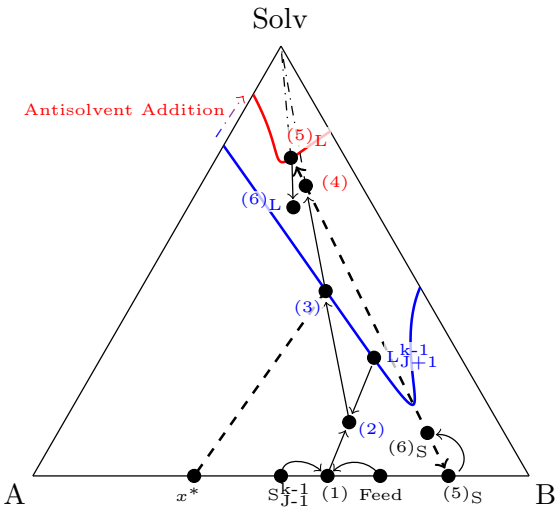

Figure 4.24: (Pseudo-)ternary phase diagram of antisolvent crystallization to bypass the alyotrope. **(1)**: mixing of solid and feed; **(2)**: mixing of solid and liquid; **(3)**: dissolution; **(4)**: antisolvent addition; **(5)**: crystallization along tie line; **(6)**: antisolvent removal and correction for residual moisture. Blue: solubility line of pure solvent; red: solubility line of solvent/antisolvent mixture; arrows: process pathways; dashed line/arrows: tie line/process pathways along tie line; dashdotted lines: constant A:B ratio. Published in [1].

If both compounds should be purified, a dual counter-current crystallization is required, which's separate cascades are connected via liquid product streams. These are close to their respective alyotropic compositions. As a simple proof of concept, a dual counter-current crystallization with, one stage each, was predicted and experimentally conducted during this work. A simplified flow scheme of this process is illustrated in Figure 4.25.

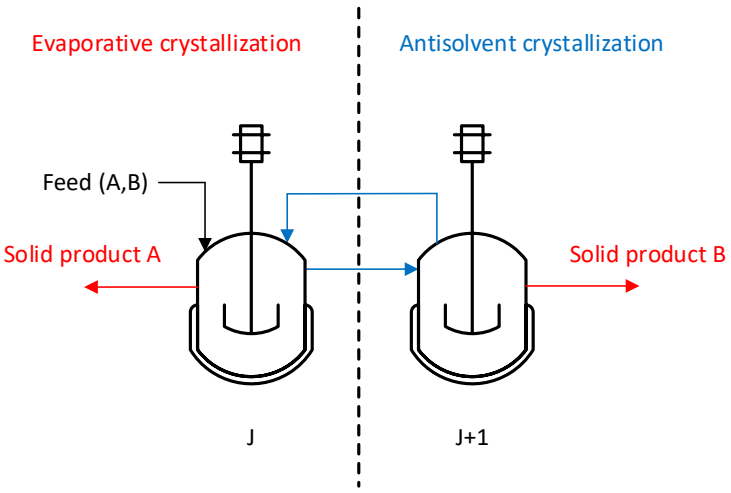

Figure 4.25: Simplified flow scheme of the alyotrope separation (Run 3). Blue: liquid streams; red: solid streams; dashed line: boundary between region I (left) and region II (right). Published in [1].

Here, crystallizer J was operated as evaporative crystallization, while in crystallizer $J+1$, antisolvent crystallization, using ethanol, was used. A feed stream consisting of 85/15 wt.% L-valine /L-leucine was supplied to crystallizer J and completely dissolved with the undersaturated liquid stream coming from $J+1$ and added solvent. After solvent evaporation, recrystallization, and solid phase separation, the liquid phase was transported to $J+1$ and subsequently mixed with ethanol. After this antisolvent crystallization, solid product was taken out of the process and the liquid phase was given back into J to be mixed with fresh feed of the next crystallization cycle. In addition to a predictive process simulation, this process was performed in the pilot plant at a scale of $m_{Feed} = 25\ g$ and their results are compare in the following. For this, Figure 4.26 depicts the (pseudo-)ternary phase diagram of the alyotrope separation process. Here, crystallizer J, in which evaporative crystallization was utilized, is pictured in red, while the antisolvent crystallizer $J+1$ is illustrated in blue. As in previous sections, solid lines describe experimental data sets and predictions are given by dashed lines. Additionally, the isopleths of the alyotropic compositions for water (black) and water/ethanol (green) are shown as dashdotted lines. The evaporation $\delta_J = 0.6653$ and antisolvent $\zeta_{J+1} = 0.2383$ were obtained by optimizing Eq. (4.58) in terms of maximum purification for both solutes, while disregarding their yields, in an attempt to achieve the largest composition difference between the products.

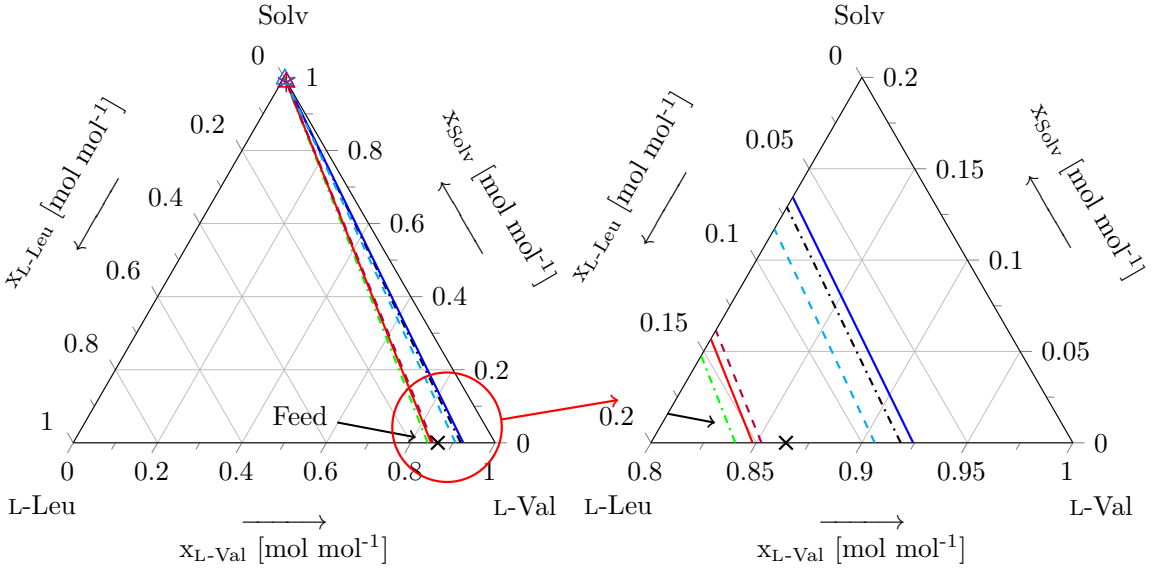

Figure 4.26: (Pseudo-)ternary phase diagram of the alyotrope separation (Run 3) performed at 25 °C. Solid lines: experimental data sets; dashed lines: predicted data sets; dashdotted lines: alyotropic compositions in water (black) and water/ethanol ($\zeta_{EtOH} = 0.2383$, green). Red: evaporative; blue: antisolvent crystallization. Published in [1].

As observable in Figure 4.26, the process simulation is able to predict the experiments well even close to the alyotrope, where small deviations in the liquid phase have a large impact on the solid phase composition. Additionally, for antisolvent crystallization, the previously

not validated region II can be described in good agreement with the experiments. Further, the diagrams show that the evaporative crystallization in J occurs completely in region I and enriches L-leucine in the solid phase, while L-valine is enriched towards the alyotrope in the liquid phase. Conversely, in vessel $J+1$, the antisolvent crystallization takes place solely in region II, on the L-valine-rich side of the alyotropic composition (green). It should be noted, that the crystallization in vessel $J+1$ only surpasses the alyotropic composition of water (black) slightly for the experiments and not at all in the simulated data sets. While this puts the composition back into region I after the removal of antisolvent, additional antisolvent crystallizations could be utilized to again shift to region II and further enrich L-valine in this solid phase. Which compound is enriched in the solid phases of each crystallizer can better be observed in the distribution diagram given in Figure 4.27. Operating points above the 45° line enrich L-leucine, while below the diagonal, L-valine is enriched in the solid phase, which again, proofs the successfully bypassing of the alyotrope in this process.

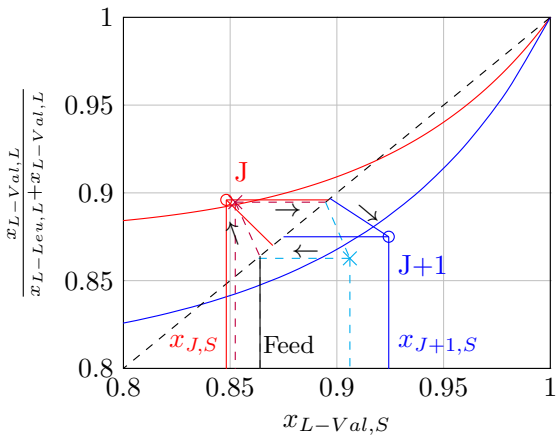

Figure 4.27: Distribution diagram of the alyotrope separation (Run 3) performed at 25 °C. Solid curved lines calculated with Eqs. (2.40) and (2.42); red: evaporative; blue: antisolvent crystallization; solid lines, o: experimental; dashed lines, ∗: simulated data sets; arrows: process pathways; black dashed line: 45° line. Published in [1].

Additionally, the deviations between experimental and predicted purifications are illustrated in Figure 4.27. The simulation predicted a $\beta'_L = 0.7\bar{3}$ for both crystallizers, since the optimization was not weighted in any way, favoring one crystallizer over the other. However, the experimental runs show purifications of $\beta'_{J,L} = 0.4\bar{7}$ and $\beta'_{J+1,L} = 0.3\bar{4}$, which results in higher solid phase purification as compared to the prediction with $J+1$ showing a larger relative disagreement. Additionally, due to $J+1$'s increased solid phase purification, its corresponding liquid phase also changes in composition. This influences the inital composition in J after the liquid is mixed with feed and thus resulting in additional

deviations in steady state operation.
The two-stage process described above solely serves as a proof of concept for the alyotrope separation. However, in a more application focused approach, an increased number of separation stage as well as optimal crystallization strategies and conditions would be applied. To exemplify, a five-stage process is simulated with more realistic parameters. Here, a 25/75 *wt.*% L-valine /L-leucine mixture is purified with a dual counter-current crystallization cascade utilizing three evaporative and two antisolvent stages. Following Section **4.3.2**, acetone is chosen as antisolvent and both cascades are operated isothermally at 25 °C. Further, the feed is supplied in stage 3 and the cascades are connected via liquid steams from stage 3 to 4 and from 4 to 2, which resulted in the best results in terms of yield out of the possible combinations. However, this was not investigated further in this work, as it was outside the scope. More information and further potential investigations regarding this are given in Section **4.5**. Figure 4.28 illustrates the five-stage process flow scheme of the process discussed in this section.

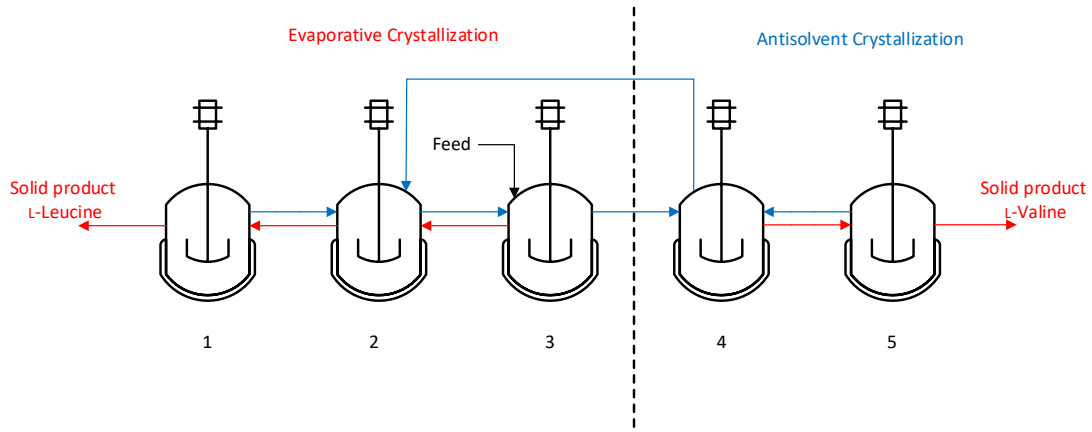

Figure 4.28: Simplified flow scheme of a five-stage alyotrope separation (Runs 4 and 5 (evaporation only)) utilizing three evaporation and two antisolvent stages. Blue: liquid streams; red: solid streams; dashed line: boundary between region I (left) and region II (right).

The process was again optimized with Eq. (4.58) unweighted regarding purities and yields, which resulted in the following δ, ζ, and β'_L values, given in Table 4.4.
Interestingly, the optimization resulted in comparably low values of β'_L for evaporative and high values for antisolvent stages. This is most likely due to the low overall separation efficiency in region II of this specific system.

Table 4.4: Optimized evaporation δ and antisolvent ζ factors as well as resulting liquid phase purification β'_L for each stage of the five-stage alyotrope separation (Runs 4 and 5 (evaporation only)) portrayed in Figure 4.28.

Run 4/5	Evaporation			Antisolvent	
Stage	1	2	3	4	5
δ, ζ	0.5406	0.4371	0.4918	0.1489	0.1670
β'_L	0.3544	0.1833	0.3478	0.6189	0.6989

This behavior is illustrated in the various distribution diagrams for different antisolvent/solvent mixtures in Section **3.3**. In stages 4 and 5, higher β'_L values result in a relative increase in precipitated crystal mass, which is required to obtain similar scales to stages 1 to 3. In which, due to better overall purification , similar crystal masses with higher purification can be produced. In the (pseudo)-ternary phase diagram in Figure 4.29, the changes is overall purification between the stages can be observed.

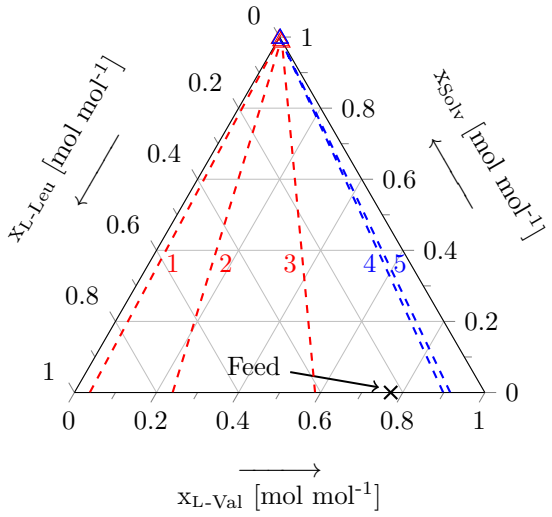

Figure 4.29: (Pseudo-)ternary phase diagram of the five-stage alyotrope separation (Run 4) predicted for 25 °C. Dashed lines: predicted data sets; red: evaporative; blue: antisolvent crystallization.

Additionally, for both regions, the solid purification effectiveness is not constant over the crystallizer cascade. Similar behavior was found in Section **4.4.3**, however, since here, the process was optimized to favor both products, the effect is more pronounced. Some crystallizers seem to favor crystal amounts over purity and vise versa, underlining the importance of varying purification in different stages to improve process efficiency, which usually is not utilized in classical rectification processes.
Using the optimized parameters, listed in Table 4.4, to predict a steady state of the five-stage process results in the yields and product purities given in Table 4.5. Additionally,

yields and purities of a three-stage process, using the same δ values for stages 1 to 3, are calculated and compared.

Table 4.5: Predicted purities and yields of the five-stage alyotrope separation (Run 4) and a comparable three-stage evaporative crystallization (Run 5) for the parameters given in Table 4.4.

Run 4	Five-Stage	
	L-Val	L-Leu
$x_{i,Prod}$	0.9156	0.9621
Y_i	0.9635	0.7911
Run 5	Three-Stage	
	L-Val	L-Leu
$x_{i,Prod}$	0.8767	0.9788
Y_i	0.9813	0.5290

The optimized five-stage process results in high purities of 0.9621 for L-leucine with a relatively high yield of 0.7911. For L-valine , the process exhibits a lower purity of 0.9156 and a higher yield of 0.9635. To compare the improvement of the process, due to the alyotrope separation, a three-stage process based solely on evaporative crystallization was calculated using the same purification strategy. The three-stage process resulted in purities of 0.9788 and 0.8767 for L-leucine and L-valine , respectively. While the purity of L-leucine is slightly higher for the three-stage process, the purification of L-valine is limited by the alyotrope and therefore results in a lower purity. Additionally, the lower purity results in a higher yield for L-valine with a value of 0.9813.
However, since more L-leucine is found in the liquid product in stage 3, its yield is significantly decreased to 0.5290. It could be argued, that the improved yield of the five-stage process is due to two additional separation stages, however, as mentioned previously, stages 4 and 5 have a low overall separation efficiency and comparing the five-stage alyotrope separation to a five-stage evaporative crystallization does not result in a just comparaison. Nevertheless, regardless of the reduced separation efficiency in region II, the alyotrope separation significantly improves the process's L-leucine yield by roughly 26 % with only slight in- and decreases in L-valine and L-leucine purities, respectively. The yield of L-valine is only slightly lowered. Further, the investigation of such separation problems, illustrates the complex optimization, quantification, and comparaison to similar processes. A more in-depth discussion about this and additional potential process variants are given in Section **4.5**.

4.5 Identified further Potential

This section gives concluding remarks about the utilization of counter-current crystallization processes to separate solid solutions, highlights its challenges, and proposes approaches and process variants to further improve the competitiveness of the process. This work showcased conceptual approaches to design counter-current crystallization processes in terms of conditions and crystallization strategies. For the case of separating an alyotropic system, the phase diagram was separated into two distinct regions I and II (see Section **4.3.2**) and one strategy and condition was chosen in this study for each of these regions. However, it might be adventageous to investigate each crystallizer individually regarding its optimal crystallization strategy. For the system investigated in this work, evaporative crystallization was determined for region I, while acetone was was utilized as an antisolvent in region II (see Figure 4.28). It could be reasoned, that for antisolvent crystallization using acetone could be more efficient than evaporative crystallization according to Section **4.3.2** in region I. Therefore, an alternative setup shown in Figure 4.28 would be to use antisolvent crystallization, with acetone, in stages 1, 2, 4, and 5, while only operating stage 3 as evaporative crystallization to still enable the alyotrope separation by shifting the alyotropic composition. Results given in Section **4.3.2** are based on heuristic approaches focusing on the best separation efficiency, while largely disregarding process productivity. Here, elevated temperatures, which increases solubilities might lead to increased productivity even though lower separation efficiencies are reached. Similarly, variations in the solution's pH, especially for amino acids, might improve productivity by significantly increasing their solubility [101, 102]. However, due to the introduction of additional compounds into the system, process complexity increases as well.
Another possibility to improve productivity is to decrease the time for each process cycle. This can be achieved by optimizing the process equipment and its operation, as shown in Section **4.4.1**, to minimize the time requirement for step such as evaporation of solvent or antisolvent as well as filtration of the equilibrated phases. E.g. improved evaporation rates could be achieved by substituting the falling film evaporator with forced circulation evaporation, commonly found in continuous crystallization [103]. In falling film evaporators, partial evaporation occurs within the evaporator itself, which may lead to unwanted heterogeneous nucleation on the walls of the evaporator. In forced circulation evaporation, the solution is superheated and partially evaporated via flash evaporation at the inlet to the crystallizer, therefore reducing the possibility of nucleation within the evaporator itself. Among other possibilities, the filteration step can be shortened by using larger filter pore sizes, which leads to an easier, and therefore faster, filtration. However, more fine crystals might be able to penetrate the filter and remain in the liquid phase after the filtration, reducing the solid phase product mass and overall separation efficiency of the separation

stage. Alternatively, to improve the process equipment, the cycle time can be reduced by shortening the equilibration time of the phases after crystallization. This work focuses solely on equilibrated phases and therefore at least 72 h were given for complete equilibration (disregarding the metastable co-crystal V_3L described in Section **3.5**). By operating the process at non-equilibrium conditions, this time can be reduced, which would significantly improve productivity. However, to obtain an accurate prediction, which in turn can be utilized to design and operate the counter-current crystallization, reliable kinetic models for the nucleation and growth of solid solutions have to be derived. Population balance models able to portray this behavior, may be highly complex since not a single solid phase nor a non-miscible solid mixture is obtained and its kinetics might change with solid phase composition.

Apart from improving the existing process strategies, in upcoming works, more complex separation problems might be addressed. In this work, the formation of co-crystals in solid solutions exhibiting systems is only covered auxiliarly, since V_3L did not impose further challenges on separation tasks, due to its metastablility as investigated in Section **3.5**. However, stable distinct and partially miscible co-crystals (see Figures 2.10 and 2.11) will lead to increased system complexity. Miscible co-crystals may be separated similarly to alyotropes, since all limiting local solubility mini- and maxima can be shifted with changing temperature and solvent composition. For miscible co-crystals, three limitations occur in such systems which might require more regions with changing conditions to achieve a successful separation. On the other hand, distinct co-crystals impose a set limitation at their composition, which cannot be shifted under any conditions and therefore, make separation, in analogue to alyotropes, impossible.

In some cases, distinct co-crystals show miscibility at elevated temperatures, such as the salicylic acid/anthranilic acid system [51], which allows for separation as a miscible co-crystal at specific conditions. In cases of strictly distinct co-crystals, one possible solution to achieve crystallization-based separation is to introduce one- or two-sided product refluxes into the process. Figure 4.30 illustrates the flow-scheme of such a counter-current crystallization capable of separating distinct co-crystals with a one-sided reflux.

In the illustrated counter-current crystallization, a feed is introduced and purified until the co-crystal composition, dashed line in Figure 4.30, in the liquid and a pure product A in the solid phase is reached. Then, the liquid phase, at co-crystal composition, is mixed with a reflux stream from solid product B to shift the composition of this stream over the co-crystal composition, which then can be further purified in to pure product B and a smaller liquid stream at co-crystal composition. The liquid phase is given back into the first part of the column to be mixed with the feed of the next cycle. To potentially increase efficiency, a reflux can be employed in each counter-current cascade to obtain a two-sided reflux. Apart from separating co-crystals, exploiting such refluxes might be beneficial in alyotrope and partial solid solution separation as well, to shift the composition inside the

crystallizers further away from the alyotropic and double saturation point, respectively. This results in better separation efficiency of the subsequent crystallization as seen in various distribution diagrams within this work i.e. in Figure 3.9 etc..

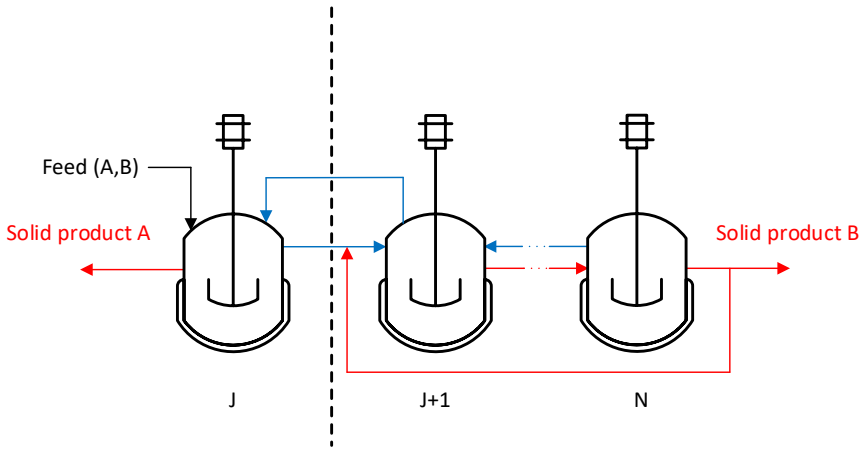

Figure 4.30: Principle of counter-current crystallization proposed to separate distinct co-crystals with one-sided reflux. Blue: liquid streams; red: solid streams; dashed line: distinct co-crystal composition.

Another relevant separation challenge is the purification of solid solutions formed by more than two compounds. This might especially be applicable for the purification of plant extracts or bio-refineries, in which a large variety of compounds are present in any given educt. In solutions containing multiple amino acids, ternary or even more complex solid solutions might be observed. Inspiration for potential separation approaches can again be drawn from rectification, where, to separate three or more components, dividing wall columns are utilized [104]. Recently, the dividing wall principle was sucessfully integrated into simulated moving bed chromatography to separate ternary mixtures [105]. Similarly, this principle might be adapted for counter-current crystallization by a configuration illustrated in Figure 4.31.

For the simplest example of a ternary lyotropic continuous solid solution consisting of compounds A, B, and C, compound A exhibits the lowest solubility, while C shows the highest solubility in a given solvent. Thus, they are purified at the edges of the cascade as solid and liquid product, respectively, in analogue to a classical counter-current crystallization. Compound B, which shows medium relative solubility, is enriched around the dividing wall (dashed line) and can be gathered as solid product as well.

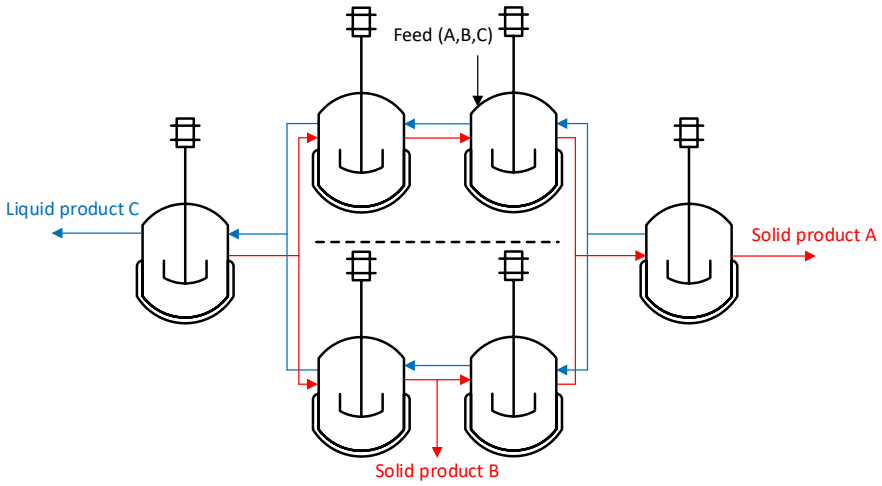

Figure 4.31: Adapting the principle of dividing wall distillation to counter-current crystallization capable to separate ternary solid solutions. Blue: liquid streams; red: solid streams; dashed line: graphical representation of the dividing wall.

The respective purities of all compounds heavily depend on the chosen purification grade β'_L and the number of separation stages in each section of the cascade. By introducing additional product withdrawls, given sufficient separation stages, solid solution systems with four or more compounds should theoretically be purifiable. It should be noted, that the process ideas proposed in Figures 4.30 and 4.31 are not investigated further in this work and should therefore be treated as unvalidated process concepts.
Lastly, for the classical counter-current crystallization and its more complex process variants, a rigorous in-depth optimization should be performed, which aside from quantitative measures such as yields, purities, number of separation stages, etc., also should take qualitative decisions of crystallization strategies, conditions, and more into account.

5. Conclusions and Outlook

The conceptual design of crystallization-based separations of solid solutions was investigated in this work. Previously researched counter-current crystallization processes were extended developing a new approach to quantify solid solution separation and its combination with antisolvent crystallization to enable new process concepts and improve process efficiencies. To design such processes extensive knowledge of the solid-liquid equilibrium behavior of solid solution forming systems is required. This work describes how these equilibria can be determined experimentally, which type of behaviors can be expected and how to differentiate between various cases. Observed behaviors range from simple lyotropic complete solid solutions, which show steady solubility changes and miscibility of the solid phase over the complete composition range, up to partial solid solution including distinct or miscible co-crystal formation. Experimental equilibria investigations of the model system L-valine /L-leucine in water and various water/antisolvent mixtures focused on slurry solubility experiments, analyzed via HPLC and PXRD measurements. DSC measurements could not be utilized due to thermal decomposition of amino acids prior to melting.

This work introduces empirical and semi-predictive models for continuous solid solutions, capable of describing solid-liquid equilibria in good agreement with experimental data sets. The semi-predictive thermodynamic model is based on a combination of semi-empirical NRTL and predictive PC-SAFT models to describe the solid and liquid phases, respectively. The purely empirical model based on polynomial and exponential equations was able to describe solid solutions in good agreement with experimental data.

With respect to the L-valine (V)/L-leucine (L) system, a co-crystal V_3L was reported in literature prior to this work. However, its stability and influence on the system's solid-liquid equilibria was not further investigated. This work extended the available research by confirming the metastability, slurry and sublimation behavior of V_3L. From the results it can be concluded, that for a counter-current crystallization separation process, the co-crystal's influence can be neglected.

Utilizing the knowledge about the solid-liquid equilibria acquired in lab scale experiments and theoretical calculations, a counter-current crystallization process was designed. For this, an empirical process simulation for evaporative crystallization was extended and optimized to quantify various complex influences on the processes of cooling and antisolvent crystallization, as well as for the prediction of more complex process variants. Predictions were successfully validated using a pilot plant setup of the counter-current crystallization process at a scale of 3 L per crystallizer.

In addition to process simulations and conducting experiments, a new approach to quantify solid solution purification was developed. In analogue to the catalyst effectivity η_{cat} applied in chemical reaction engineering, the ratio of the purification in the liquid and solid phases can be used to obtain a comparison for different crystallizer conditions, strategies, and supersaturations. This approach has successfully been utilized in this work to identify optimal crystallization strategies and conditions to be applied in different sections within the counter-current cascade. Using these strategies, a novel process concept was proposed to enable separation of components forming alyotropic solid solutions. The process is based on shifting the alyotropic composition with changes in temperature or solvent composition. This shift allows bypassing this limitation similar to bypassing an azeotrope in pressure swing rectification. Further, utilizing antisolvent crystallization can substantially improve the process efficiency, especially for thermally sensitive compounds or systems exhibiting low temperature dependence of the solubility.

Outlook

This thesis provides a basis for potential future projects. Key directions are seen especially regarding improvements and new variants of counter-current crystallization. This includes the development of process concepts to solve more challenging separation tasks like co-crystals and ternary solid solutions as well as ideas to improve the present process by employing more efficient equipment or operating the process at non-equilibrium conditions. While solid solutions are not very well know in organic systems, prior investigations from inorganic systems should be utilized to broaden knowledge in this field. As a part of this work, preliminary solid-liquid equilibria determination of the L-glutamic acid/L-aspartic partial solid solution system were conducted. Such systems and their influence on the separation using counter-current crystallization should be investigated further.
Future works regarding solid solutions and their separation might focus on developing thermodynamic models to increase their accuracy and enable the prediction of more complex phase behaviors like partial solid solution and co-crystal formation. A starting point could be to take charges of dissociated amino acids depending on the solvent polarity into account within the calculations, which would also enable predictions of pH dependent solubilities. Further, the thermodynamic model, proposed in Section **3.4**, can be utilized to conduct more extensive antisolvent screening to potentially acquire a more potent alternative to acetone or ethanol for the L-valine /L-leucine system.
All in all, counter-current crystallization is a complex but powerful process capable to separate solid solutions. Its analogies to rectification can be exploited more to derive advanced process schemes and deal with complex phase behaviors. Its inherently high flexibility allows for an in-depth tailoring of the counter-current crystallization to match specific problems and separation tasks.

References

[1] V. Tenberg, M. Sadeghi, A. Seidel-Morgenstern, and H. Lorenz, "Bypassing thermodynamic limitations in the Crystallization-based separation of solid solutions," *Sep. Purif. Technol.*, vol. 283, p. 120 169, 2022.

[2] V. Tenberg, M. Hokmabadi, A. Seidel-Morgenstern, H. Lorenz, and M. Sadeghi, "Investigation of the Antisolvent Effect on the Phase Behavior of Amino Acid Solid Solutions," *Ind. Eng. Chem. Res.*, vol. 62, no. 1, pp. 753–761, 2023.

[3] M. Sadeghi, V. Tenberg, S. Münzberg, A. Seidel-Morgenstern, and H. Lorenz, "Phase equilibria of L-Valine/L-Leucine solid solutions," *J. Mol. Liq.*, vol. 340, p. 117 315, 2021.

[4] M. Sadeghi, F. Cascella, V. Tenberg, A. Seidel-Morgenstern, and H. Lorenz, "Solubility analysis of pharmaceuticals guaifenesin, ketoprofen, and artemisinin in different solvents," *J. Mol. Liq.*, vol. 343, p. 117 503, 2021.

[5] A. S. Myerson, *Handbook of Industrial Crystallization, 2nd ed.* Butterworth-Heinemann, 2002.

[6] W. Beckmann, *Crystallization: Basic Concepts and Industrial Applications, 3rd ed.* Wiley-VCH Verlag GmbH & Co. KGaA, 2013.

[7] H. Lorenz and A. Seidel-Morgenstern, "Processes To Separate Enantiomers," *Angew. Chem. Int.*, vol. 53, no. 5, pp. 1218–1250, 2014.

[8] A. Zaykovskaya and M. Louhi-Kultanen, "Batch Crystallization of Xylitol by Cooling, Evaporative, and Antisolvent Crystallization," *Cryst. Growth Des.*, 2023, in press, available online.

[9] Y. C. Liu, D. Dunn, M. Lipari, A. Barton, P. Firth, J. Speed, J. Wood, and Z. K. Nagy, "A comparative study of continuous operation between a dynamic baffle crystallizer and a stirred tank crystallizer," *Chem. Eng. J.*, vol. 367, pp. 278–294, 2019.

[10] J. M. Prausnitz, R. N. Lichtenthaler, and E. G. de Azevedo, *Molecular Thermodynamics of Fluid Phase Equilibria, 3rd ed.* Prentice-Hall, 1999.

[11] B. Predel, M. Hoch, and M. Pool, *Phase Diagrams and Heterogeneous Equilibria - A Practical Introduction, 1st ed.* Springer-Verlag, 2004, Berlin Heidelberg New York.

[12] G. Matz, "Fraktionierte Kristallisation," *Chem.-Ing.-Tech.*, vol. 52, no. 7, pp. 562–570, 1980.

[13] S. Münzberg, T. G. Vu, and A. Seidel-Morgenstern, "Generalizing Countercurrent Processes: Distillation and Beyond," *Chem.-Ing.-Tech.*, vol. 90, no. 11, pp. 1769–1781, 2018.

[14] A. I. Kitaigorodsky, *Mixed Crystals*. Springer-Verlag, 1984, Berlin Heidelberg New York Tokyo.

[15] M. À. Cuevas-Diarte and H. A. J. Oonk, *Molecular Mixed Crystals*. Springer Nature Switzerland, 2021, Cham.

[16] M. Matsuoka, "Developent in Melt Crystallization," in J. Garside, R. Davey, and A. G. Jones, Eds. Butterworth-HeineMann, Oxford, 1991, Advances in Industrial Crystallization.

[17] A. Poulos, J. W. Greiner, and G. A. Fevig, "Separation of Sterols by Countercurrent Crystallization," *Ind. Eng. Chem.*, vol. 53, no. 12, pp. 949–962, 1961.

[18] S. W. Lin, K. M. Ng, and C. Wibowo, "Synthesis of crystallization processes for systems involving solid solutions," *Comput. Chem. Eng.*, vol. 32, pp. 956–970, 2008.

[19] K. F. Luk, K. M. Ko, and K. M. Ng, "Separation and purification of (-)schisandrin B from schisandrin B stereoisomers," *Biochem. Eng. J.*, vol. 42, pp. 55–60, 2008.

[20] K. S. Kwok, Y. C. Chan, K. M. Ng, and C. Wibowo, "Separation of Fullerenes C_{60} and C_{70} Using a Crystallization-Based Process," *AIChE J.*, vol. 56, no. 7, pp. 1801–1812, 2010.

[21] N. A. Aumock, *A Process for Separation by Semi-Continuous Counter-Current Crystallization - Dissertation*. Massachusetts Institute of Technology, 2011.

[22] M. Balawedjder, K. Galan, M. P. Elsner, A. Seidel-Morgenstern, W. Piatkowski, and D. Antos, "Multi-stage crystallization for resolution of enantiomeric mixtures in a solid solution forming system," *Chem. Eng. Sci.*, vol. 66, pp. 5638–5647, 2011.

[23] E. Temmel, U. Müller, D. Grawe, R. Eilers, H. Lorenz, and A. Seidel-Morgenstern, "Equilibrium model of a continuous crystallization process for separation of substances exhibiting solid solutions.," *Chem. Eng. Technol.*, vol. 35, pp. 980–985, 2012.

[24] E. Temmel, S. Wloch, U. Müller, D. Grawe, R. Eilers, H. Lorenz, and A. Seidel-Morgenstern, "Aufreinigung durch mehrstufige Gegenstromkristallisation zur Herstellung hochreiner Pharmazeutica," *Chem.-Ing.-Tech.*, vol. 85, no. 10, pp. 1581–1588, 2013.

[25] E. Temmel, S. Wloch, U. Müller, D. Grawe, R. Eilers, H. Lorenz, and A. Seidel-Morgenstern, "Separation of systems forming solid solutions using counter-current crystallization," *Chem. Eng. Sci.*, vol. 104, pp. 662–673, 2013.

[26] S. Münzberg, H. Lorenz, and A. Seidel-Morgenstern, "Multistage Countercurrent Crystallization for the Separation of Solid Solutions," *Chem. Eng. Technol.*, vol. 39, no. 7, pp. 1242–1250, 2016.

[27] V. A. Kiva, E. K. Hilmen, and S. Skogestad, "Azeotropic phase equilibrium diagrams: a survey," *Chem. Eng. Sci.*, vol. 58, pp. 1903–1953, 2003.

[28] I. Kurosawa, A. S. Teja, and R. W. Rousseau, "Solid-liquid equilibria in L-leucine + L-valine + water," *Fluid Ph. Equilibr.*, vol. 228-229, pp. 83–87, 2005.

[29] H. Schuberth, "Vorhersage alyotroper Effekte in ternären flüssigen Systemen," *Monatsh. Chem.*, vol. 120, pp. 955–966, 1989.

[30] M. Prieto, "Thermodynamics of Solid Solution-Aqueous Solution Systems," *Rev. Mineral. Geochem.*, vol. 70, pp. 47–85, 2009.

[31] A. I. Isakov, H. Lorenz, A. A. Zolotarev Jr, and E. N. Kotelnikova, "Heteromolecular compounds in binary systems of amino acids with opposite and same chiralities," *Cryst. Eng. Comm.*, vol. 22, no. 5, pp. 986–997, 2020.

[32] E. W. Thiele, "Relation between Catalytic Activity and Size of Particle," *Ind. Eng. Chem.*, vol. 31, no. 7, pp. 916–920, 1939.

[33] K. J. Roberts, R. Docherty, and R. Tamura, *Engineering Crystallography: From Molecule to Crystal to Functional Form*. Springer, 2017.

[34] J. Rosen, O. Warschkow, and D. R. McKenzie, "Amorphous and crystalline phases in thermal quench simulations of alumina," *J. Chem. Phys.*, vol. 126, p. 204 709, 2007.

[35] K. Srinivasan and P. Dhanasekaran, "Nucleation control and crystallization of L-glutamic acid polymorphs by swift cooling process and their characterization," *J. Cryst. Growth*, vol. 318, pp. 1080–1084, 2011.

[36] H. Lorenz, "Solubility and Solution Equilibria in Crystallization," in W. Beckmann, Ed. Wiley-VCH Verlag GmbH & Co. KGaA, 2013, Crystallization: Basic Concepts and Industrial Applications.

[37] W. Kaialy and A. Nokhodchi, "Antisolvent crystallisation is a potential technique to prepare engineered lactose with promising aerosolisation properties: Effect of saturation degree," *Int. J. Pharm.*, vol. 437, pp. 57–69, 2012.

[38] J. W. Gibbs, "On the Equilibrium of Heterogeneous Substances," *Transactions of the Connecticut Academy of Arts and Sciences*, vol. III, 108-248 and 343–524, 1876-1878.

[39] M. Lusi, "A rough guide to molecular solid solutions: design, synthesis and characterization of mixed crystals," *CrystEngComm*, vol. 20, pp. 7042–7052, 2018.

[40] J. H. Tregilgas and J. M. Galligan, "Dislocations, superconductors, and solid solutions," *Scripta Metallurgica*, vol. 9, pp. 199–206, 1975.

[41] L. B. Dubrovskaya, S. Z. Nazarova, and A. F. Prekul, "Superconducting and Normal Properties of Solid Solutions $Nb_{1-x}Ta_xC_y$," *Phys. Stat. Sol.*, vol. 69, pp. 167–172, 1982.

[42] H. Zhang, Y. Liu, H. L. Li, J. F. Qu, X. G. Li, and Y. Feng, "Effects of solid solutions on the superconducting properties of Gd-Ba-Cu-O superconductors," *Supercond. Sci. Technol.*, vol. 18, pp. 1317–1322, 2005.

[43] K. Ren, J. Wu, Q. Yang, Y. Fu, G. Nian, and Z. Xie, "Solid solution effect boosts the photovoltaic performance of PCDTBT-based organic solar cells," *Org. Electron.*, vol. 104, p. 106 489, 2022.

[44] K. Saršūns, M. Kemere, A. Karziņins, I. Kļimenkovs, A. Bērziņš, A. Sarakovskis, and T. Rekis, "Fine-Tuning Solid State Luminescence Properties of Organic Crystals via Solid Solution Formation: The Example of 4-Iodothioxanthone-4-Chlorothioxanthone System," *Cryst. Growth Des.*, vol. 22, pp. 4838–4844, 2022.

[45] S. A. Raza, U. Schacht, V. Svoboda, D. P. Edwards, A. J. Florence, C. R. Pulham, J. Sefcik, and I. D. H. Oswald, "Rapid Continuous Antisolvent Crystallization of Multicomponent Systems," *Cryst. Growth Des.*, vol. 18, pp. 210–218, 2018.

[46] W. L. McCabe and E. W. Thiele, "Graphical Design of Fractionating Columns," *Ind. Eng. Chem.*, vol. 17, no. 6, pp. 605–611, 1925.

[47] W. Beckmann and H. Lorenz, "Partial Miscibility of Organic Compounds in the Solid State - The Case of Two Epimers of a Diastereoisomer," *Chem. Eng. Technol.*, vol. 29, no. 2, pp. 226–232, 2006.

[48] N. V. Taratin, H. Lorenz, E. N. Kotelnikova, A. E. Glikin, A. Galland, V. Dupray, G. Coquerel, and A. Seidel-Morgenstern, "Mixed Crystals in Chiral Organic Systems: A Case Study on (R)- and (S)-Ethanolammonium 3-Chloromandelate," *Cryst. Growth Des.*, vol. 12, pp. 5882–5888, 2012.

[49] I. Kurosawa, A. S. Teja, and R. W. Rousseau, "Solubility Measurements in the L-Isoleucine + L-Valine + Water System at 298 K," *Ind. Eng. Chem. Res.*, vol. 44, pp. 3284–3288, 2005.

[50] A. I. Isakov, E. N. Kotelnikova, S. Münzberg, S. N. Bocharov, and H. Lorenz, "Solid phases in the system L-valine - L-isoleucine," *Cryst. Growth Des.*, vol. 16, pp. 2653–2661, 2016.

[51] F. L. Nordstrom, S. S. Mohajerani, B. Linehan, and F. Ricci, "Enantiotropic inconstancy, crystalline solid solutions and co-crystal in the salicylic acid-anthranilic acid system," *Phys. Chem. Chem. Phys.*, vol. 24, pp. 26 485–26 498, 2022.

[52] C. Wibowo and K. M. Ng, *Conceptual Design of Crystallization Processes*. Walter de Gruyter GmbH, 2021, Berlin/Boston.

[53] J. Smith, H. Van Ness, M. Abbott, and M. Swihart, *Introduction to Chemical Engineering Thermodynamics*. McGraw-Hill, 2018, 8th ed.

[54] G. N. Lewis, "Outlines of a New System of Thermodynamic Chemistry," *Proceeding of the American Academy of Arts and Sciences*, vol. 43, no. 7, pp. 259–293, 1907.

[55] J. Gmehling, M. Kleiber, B. Kolbe, and J. Rarey, *Chemical Thermodynamics for Process Simulation, 2nd ed.* Wiley-VCH, 2019, Weinheim.

[56] H. Renon and J. M. Prausnitz, "Local compositions in thermodynamic excess functions for liquid mixtures," *AIChE J.*, vol. 14, no. 1, pp. 135–144, 1968.

[57] D. S. Abrams and J. M. Prausnitz, "Statistical thermodynamics of liquid mixtures: A new expression for the excess Gibbs energy of partly or completely miscible systems," *AIChE J.*, vol. 21, no. 1, pp. 116–128, 1975.

[58] A. Fredenslund, R. L. Jones, and J. M. Prausnitz, "Group-contribution estimation of activity coefficients in nonideal liquid mixtures," *AIChE J.*, vol. 21, no. 6, pp. 1086–1099, 1975.

[59] W. G. Chapman, K. E. Gubbins, G. Jackson, and M. Radosz, "New Reference Equation of State for Associating Liquids," *Ind. Eng. Chem. Res.*, vol. 29, pp. 1709–1721, 1990.

[60] J. Gross and G. Sadowski, "Perturbed-chain SAFT: An equation of state based on a perturbation theory for chain molecules," *Ind. Eng. Chem. Res.*, vol. 40, pp. 1244–1260, 2001.

[61] J. Gross and G. Sadowski, "Application of the perturbed-chain SAFT equation of state to associating systems," *Ind. Eng. Chem. Res.*, vol. 41, no. 22, pp. 5510–5515, 2002.

[62] J. A. Barker and D. Henderson, "Perturbation Theory and Equation of State for Fluids: The Square-Well Potential," *J. Chem. Phys.*, vol. 47, p. 2856, 1967.

[63] J. A. Barker and D. Henderson, "Perturbation Theory and Equation of State for Fluids. II. A Successful Theory of Liquids," *J. Chem. Phys.*, vol. 47, p. 4714, 1967.

[64] H. T. Do, Y. Z. Chua, A. Kumar, D. Pabsch, M. Hallermann, D. Zaitsau, C. Schick, and C. Held, "Melting properties of amino acids and their solubility in water," *RSC Adv.*, vol. 10, pp. 44 205–44 215, 2020.

[65] J. Sen, N. Kokubun, T. Kamei, K. Ohmori, M. Kishino, T. Kashiwagi, M. Yokota, and N. Doki, "Study of the Incorporation Behavior of L-Leu and D-Leu in L-Val Crystallization," *ACES*, vol. 6, pp. 262–268, 2016.

[66] M. S. Dunn, F. J. Ross, and L. S. Read, "The Solubility of the Amino Acids in Water," *JBC*, vol. 103, no. 2, pp. 579–595, 1933.

[67] C. E. Messer, G. Malakoff, J. Well, and S. Labib, "Phase Equilibrium Behavior of Certain Pairs of Amino Acids in Aqueous Solution," *J. Phys. Chem.*, vol. 85, pp. 3533–3540, 1981.

[68] R. Carta, "Solubilities of L-Cystine, L-Tyrosine, L-Leucine, and Glycine in Their Water Solutions," *J. Chem. Eng. Data*, vol. 44, pp. 563–567, 1999.

[69] H. C. Koolman and R. W. Rousseau, "Effects of Isomorphic Compounds on the Purity and Morphology of L-Isoleucine Crystals," *AIChE J.*, vol. 42, no. 1, pp. 147–153, 1996.

[70] C. Zhang, B. Liu, X. Wang, and H. Wang, "Measurement and Correlation of the Solubilities of L-Valine in Water, Ethanol, N,N-Dimethylformamide, Acetone, and Isopropyl Alcohol between (293.15 and 343.15) K," *J. Chem. Eng. Data*, vol. 59, pp. 2704–2708, 2014.

[71] C. Zhang, B. Liu, X. Wang, H. Wang, and H. Zhang, "Measurement and Correlation of the Solubilities of L-Valine in Water + (Ethanol, N,N-Dimethylformamide, Acetone, and Isopropyl Alcohol) between 293.15 to 434.15 K," *J. Chem. Eng. Data*, vol. 59, pp. 2732–2740, 2014.

[72] N. A. Bowden, J. P. M. Sanders, and M. E. Bruins, "Solubility of the Proteinogenic α-Amino Acids in Water, Ethanol, and Ethanol-Water Mixtures," *J. Chem. Eng. Data*, vol. 63, pp. 488–497, 2018.

[73] J. C. Givand, A. S. Teja, and R. W. Rousseau, "Effect of Relative Solubility on Amino Acids Crystal Purity," *AIChE J.*, vol. 47, no. 12, pp. 2705–2712, 2001.

[74] J. Givand, B.-K. Chang, A. S. Teja, and R. W. Rousseau, "Distribution of Isomorphic Amino Acids between a Crystal Phase and an Aqueous Solution," *Ind. Eng. Chem. Res.*, vol. 41, pp. 1873–1876, 2002.

[75] A. S. Teja, J. C. Givand, and R. W. Rousseau, "Correlation and Prediction of Crystal Solubility and Purity," *AIChE J.*, vol. 27, no. 11, pp. 2629–2634, 2002.

[76] C. Held, L. F. Cameretti, and G. Sadowski, "Measuring and Modeling Activity Coefficients in Aqueous Amino-Acid Solutions," *Ind. Eng. Chem. Res.*, vol. 50, pp. 131–141, 2011.

[77] P. Ji, J. Zou, and W. Feng, "Effect of alcohol on the solubility of amino acid in water," *J. Mol. Cat. B*, vol. 56, pp. 185–188, 2009.

[78] B. P. Dey and S. C. Lahiri, "Solubilities of Amino Acids in Different Mixed Solvents," *Indian J. Chem.*, vol. 25A, pp. 136–140, 1986.

[79] G. R. Santos, D. C. Souza, and M. Aznar, "Liquid-Liquid Equilibria of Water + 1-Butanol + Amino Acid (Glycine or DL-Alanine or L-Leucine) at 313.15 K," *J. Solution Chem.*, vol. 43, pp. 2101–2116, 2014.

[80] J.-B. G. Daldrup, C. Held, F. Ruether, G. Schembecker, and G. Sadowski, "Measurement and Modeling Solubility of Aqueous Multisolute Amino-Acid Solutions," *Ind. Eng. Chem. Res.*, vol. 49, pp. 1395–1401, 2010.

[81] I. Mills, T. Cvitaš, K. Homann, N. Kallay, and K. Kuchitsu, *Quantities, Units and Symbols in Physical Chemistry*. Blackwell Science, Oxford, 1993, 2nd ed.

[82] J. N. Miller and J. C. Miller, *Statistics and Chemometrics for Analytical Chemistry*. Pearson Education Limited, Edinburgh Gate, 2005, 5th ed.

[83] R. Hilfiker, "Characterization of Crystalline Products," in W. Beckmann, Ed. Wiley-VCH Verlag GmbH & Co. KGaA, 2013, Crystallization: Basic Concepts and Industrial Applications.

[84] M. Balawedjder, B. Mossety-Leszczak, I. Poplewska, H. Lorenz, A. Seidel-Morgenstern, W. Piatkowski, and D. Antos, "Modeling and predictions of solid–liquid equilibria for citalopram oxalate as a representative of a solid solution forming system," *Fluid Ph. Equilibr.*, vol. 346, pp. 8–19, 2013.

[85] D. P. Glavin and J. L. Bada, "Isolation of Amino Acids from Natural Samples Using Sublimation," *Anal. Chem.*, vol. 70, pp. 3119–3122, 1998.

[86] J. S. Chickos and W. E. Acree Jr., "Enthalpies of Sublimation of Organic and Organometallic Compounds. 1910-2001," *J. Phys. Chem. Ref. Data*, vol. 31, no. 2, pp. 537–698, 2002.

[87] A. Lähde, J. Raula, J. Malm, E. I. Kauppinen, and M. Karpinen, "Sublimation and vapour pressure estimation of L-leucine using thermogravimetric analysis," *Thermochim. Acta*, vol. 482, pp. 17–20, 2009.

[88] C. Viedma, W. L. Noorduin, J. E. Ortiz, T. de Torres, and P. Cintas, "Asymmetric amplification in amino acid sublimation involving racemic compound to conglomerate conversion," *Chem. Commun.*, vol. 47, pp. 671–673, 2010.

[89] C. Viedma, J. E. Ortiz, T. de Torres, and P. Cintas, "Enantioenrichment in sublimed amino acids mixtures," *Chem. Commun.*, vol. 48, pp. 3623–3625, 2012.

[90] D. W. Green and M. Z. Southard, *Perry's Chemical Engineers' Handbook, 9th ed.* McGraw-Hill Education, 2019.

[91] P. von Böckh and T. Wetzel, *Heat Transfer - Basics and Practice*. Springer-Verlag, 2012, Berlin/Heidelberg.

[92] J. Stichlmair, H. Klein, and S. Rehfeldt, *Distillation - Principles and Practice*. AIChE Inc. and Wiley-VCH, 2021, 2nd ed.

[93] Takegami, K. and Morita, M. and Nakamaru, K. and Miwa, K., "Patent US4588414A," 1986.

[94] M. Matsuoka, H. Takiyama, and O. Soutome, "Separation Characteristics of an Inclined Column Crystallizer," *Trans IChemE*, vol. 75, no. A, pp. 206–212, 1997.

[95] L. Chen, J. Li, and M. Matsuoka, "Experimental and Theoretical Investigation of the Purification Process of Organic Materials in a Continuous Inclined Column Crystallizer," *Ind. Eng. Chem. Res.*, vol. 48, no. 8, pp. 2818–2823, 2006.

[96] W. Xiao, B. Huang, Y. Li, and Z. Yi, "Experimental investigation of continuous multistage countercurrent crystallizer for separation P-nitrochlorobenzene and O-nitrochlorobenzene," *Sep. Purif. Technol.*, vol. 267, p. 118 648, 2021.

[97] G. F. Froment, K. B. Bischoff, and J. De Wilde, *Chemical Reactor Analysis and Design, 3rd ed.* Wiley, 2011, Hoboken.

[98] HAPILA GmbH, "Patent DE102008023833 (B4)," 2013.

[99] E. C. Voutsas, C. Pamouktsis, D. Argyris, and G. D. Pappa, "Measurements and thermodynamic modeling of the ethanol-water system with emphasis to the azeotropic region," *Fluid Ph. Equilibr.*, vol. 308, pp. 135–141, 2011.

[100] R. Battisti, C. A. Claumann, C. Marangoni, and R. A. Machado, "Optimization for pressure swing distillation for anhydrous ethanol purification by the simulated annealing algorithm," *Braz. J. Chem. Eng.*, vol. 36, no. 1, pp. 453–469, 2019.

[101] J.-B. G. Daldrup, C. Held, G. Sadowski, and G. Schembecker, "Modeling pH and Solubilities in Aqueous Multisolute Amino Acid Solutions.," *Ind. Eng. Chem. Res.*, vol. 50, pp. 3503–3509, 2011.

[102] C.-Y. Lee, J.-T. Chen, W.-T. Chang, and I.-M. Shiah, "Effect of pH on the solubilities of divalent and trivalent amino acids in water at 298.15 K," *Fluid Ph. Equilibr.*, vol. 343, pp. 30–35, 2013.

[103] G. Hofmann and C. Melches, "Continuous Crystallization," in W. Beckmann, Ed. Wiley-VCH Verlag GmbH & Co. KGaA, 2013, Crystallization: Basic Concepts and Industrial Applications.

[104] I. Dejanović, L. Matijašević, and Ž. Olujić, "Dividing wall column - A breakthrough towards sustainable distilling," *Chem. Eng. Process.*, vol. 49, pp. 559–580, 2010.

[105] J. W. Lee, "Expanding Simulated Moving Bed Chromatography into Ternary Separations in Analogy to Dividing Wall Column Distillation," *Ind. Eng. Chem. Res.*, vol. 59, pp. 9619–9628, 2020.

[106] H. Veith, C. Luebbert, and G. Sadowski, "Correctly measuring and predicting solubilities of solvates, hydrates, and polymorphs," *Cryst. Growth Des.*, vol. 20, pp. 723–735, 2020.

[107] M. Voges, F. Fischer, M. Neuhaus, G. Sadowski, and C. Held, "Measuring and Predicting Thermodynamic Limitation of an Alcohol Dehydrogenase Reaction," *Ind. Eng. Chem. Res.*, vol. 56, pp. 5535–5546, 2017.

Lists of Symbols

Abbreviations:

Abbreviation	Designation
API	Active pharmaceutical ingredient
$CuSO_4 \cdot 5H_2O$	Copper(II) sulfate pentahydrate
const.	Constant
DAD	Diode array detector
DSC	Differential scanning calorimetry
EoS	Equation of state
Eq.	Equation
e.g.	Exempli gratia
etc.	Et cetera
FSC	Fast scanning calorimetry
HPLC	High-performance liquid chromatography
IR	Infrared
i.e.	Id est
LP	Liquid product
MPI	Max Planck Institute
MS	Mass spectrometry
No.	Number
NRTL	Non-random two-liquid
n.a.	Not applicable
PC-SAFT	Perturbed-chain statistical associating fluid theory
PXRD	Powder X-ray diffraction
SAFT	Statistical associating fluid theory
SP	Solid product
TOC	Total organic carbon
UNIFAC	Universal quasichemical functional-group activity coefficients
UNIQUAC	Universal quasichemical
UV	Ultraviolet
var.	Varying

Greek letters:

Symbol	Designation	Unit
α	Non-randomness parameter	$[-]$
α, β	A- and B-rich solid solutions	$[-]$
β	Purification angle	$[^\circ]$
γ	Activity coefficient	$[-]$
Δ	Difference	$[var.]$
$\Delta^{A_iB_j}$	Strength of interaction between sites A_i and B_j	$[\text{Å}^3]$
δ	Evaporation factor	$[mol\,mol^{-1}]$
$\frac{\varepsilon^{A_iB_i}}{k}$	Association energy between sites A and B	$[K]$
ζ	Antisolvent factor	$[mol\,mol^{-1}]$
$\zeta_{0,\ldots,3}$	Parameter defined in Eq. (A.4)	$[\text{Å}^{-3,\ldots,0}]$
η	Packing fraction $\eta = \zeta_3$	$[-]$
η	Effectiveness	$[-]$
Θ	Angle of interference	$[^\circ]$
$\kappa^{A_iB_i}$	Association volume between sites A and B	$[-]$
λ	Wavelength	$[m]$
μ	Chemical potential	$[J\,mol^{-1}]$
ρ	Number density of molecules	$[\text{Å}^{-3}]$
ρ_i	Molar density of i	$[mol\,\text{Å}^{-3}]$
σ	Population standard deviation	$[var.]$
σ_i	Temperature-independent sphere diameter	[Å]
τ	Parameter defined in Eqs. (2.33) and (2.34)	$[-]$
Φ	Thiele modulus	$[-]$
φ	Fugacity coefficient	$[-]$

Latin letters:

Symbol	Designation	Unit
A	Absorbance	$[AU]$
A_P	Absorbance peak area	$[AU\,s]$
$\tilde{a}$	Molar Helmholtz energy	$[J\,mol^{-1}]$
a	Activity	$[-]$
a, b	Polynomial parameter	$[-]$
a_i	Parameter defined in Eq. (A.9)	$[-]$
$a_{p,m}$	Heat capacity slope parameter	$[J\,mol^{-1}\,K^{-2}]$
b_{AB}, b_{BA}	Interaction parameters in NRTL	$[J\,mol^{-1}]$
b_i	Parameter defined in Eq. (A.10)	$[-]$
$b_{p,m}$	Heat capacity intercept parameter	$[J\,mol^{-1}\,K^{-1}]$

Continued on next page ⟶

Symbol	Designation	Unit
C	Parameter defined in Eq. (A.13)	$[-]$
C_p	Molar heat capacity	$[J\,mol^{-1}\,K^{-1}]$
c	Concentration	$[kg\,L^{-1}]$
d_i	Temperature-dependent sphere diameter	[Å]
d	Layer spacing	[Å]
F	Degrees of freedom	$[-]$
F_c	Calibration factor	$[AU\,s]$
F_d	Dilution factor	$[kg\,kg^{-1}]$
f	Fugacity	$[Pa]$
G	Gibbs free energy	$[J]$
G	Parameter defined in Eqs. (2.31) and (2.32)	$[-]$
g_{ii}	Radial distribution function	$[-]$
H_m	Molar enthalpy	$[J\,mol^{-1}]$
I	Parameter defined in Eqs. (A.7) and (A.8)	$[-]$
I	Intensity	$[s^{-1}]$
K	Number of considered data points	$[-]$
k	Boltzmann constant	$[J\,K^{-1}]$
k_{ij}	Dispersion energy correction parameter between i and j	$[-]$
$LMTD$	Logarithmic mean temperature difference	$[K]$
M_A, M_B	Polynomial degree	$[-]$
M_i	Molar mass of component i	$[kg\,mol^{-1}]$
m	Mass	$[kg]$
m_i	Number of hard sphere segments	$[-]$
N	Number of components	$[-]$
N_{Av}	Avogadro's number	$[mol^{-1}]$
n	Molar amount	$[mol]$
n_I	Order of interference	$[-]$
OF	Objective function	$[-]$
P	Number of phases	$[-]$
Par	Parameter	$[var.]$
P, Q	Liquidus and solidus line	$[mol\,mol^{-1}]$
p	Pressure	$[Pa]$
p_i	Partial pressure	$[Pa]$
q_F	Caloric factor	$[-]$
R	Universal gas constant	$[J\,K^{-1}\,mol^{-1}]$
R_B, R_D	Reboiling and reflux ratio	$[-]$
R_{Anti}	Residual antisolvent	$[-]$
R_M	Residual moisture	$[-]$
T	Temperature	$[K]$
t	Time	$[s]$
U	Standard uncertainty	$[var.]$
$\frac{u}{k}$	Dispersion interaction energy	$[K]$
v	Molar volume	$[m^3\,mol^{-1}]$

Continued on next page ⟶

Symbol	Designation	Unit
W	Weighting factor	$[-]$
w	Weight fraction	$[kg\,kg^{-1}]$
x, y	Molar fractions	$[mol\,mol^{-1}]$
x^{A_i}	Molar fraction not bonded at site A of component i	$[mol\,mol^{-1}]$
Y	Yield	$[mol\,mol^{-1}]$
Z	Compressibility factor	$[-]$

Sub- and Superscripts

Symbol	Designation
0	Reference state
$(1)-(6)$	Crystallization substeps
Ace	Acetone
$Alyo$	Alyotrope
$Anti$	Antisolvent
$assoc$	Association
B	Bottoms
bin	Binary
cat	Catalyst
D	Distillate
$disp$	Perturbation
Elu	Eluent
$EtOH$	Ethanol
$Evap$	Evaporation
end	Last step
$Feed$	Feed
hc	Hard-chain
hs	Hard sphere
IPA	Isopropanol
i, j	Component i and j
id	Ideal
$init$	Initial
J	Number of crystallizer
k	Crystallization cycle
L	Liquid
$L-Leu$	L-Leucine
m	Melt
max	Maximum
min	Minimum
$Prod$	Product

Continued on next page ⟶

Symbol	Designation
$pure$	Pure component
qua	Quaternary
$real$	Real
res	Residual
S	Solid
SL	Suspension
$Solv$	Solvent
Spl	Sample
seg	Segment
ter	Ternary
th	Theoretical
V	Vapor
$L-Val$	L-Valine
W	Water
$*$	Saturation
$\overline{\square}$	Mean
$\hat{\square}$	Mixture
$\square'$	Normalized/solvent-free

List of Figures

Page

Solid-Liquid Equilibria Investigation of Solid Solutions

Counter-Current Crystallization

Appendix

List of Tables

Page

Appendix

A.1 Various Contributions in PC-SAFT

In PC-SAFT, the compressibility factor Z is calculated as the sum of various contributions (see Eq. (2.26)). In this section, the calculation for the hard-chain Z^{hc}, perturbation Z^{disp}, and association Z^{assoc} contributions are given. Additionally, the calculation of the residual chemical potential is listed below.

A.1.1 Hard-Chain Contribution

Here, the equations for the hard-chain contribution Z^{hc} is given, which are a function of the hard-sphere contribution Z^{hs} and the radial distribution function of the hard-sphere g_{ii}^{hs}. It describes the influence of the interconnected spheres, which describe a given molecule i in a system. A complete derivation can be found in literature [60].

$$Z^{hc} = \overline{m} Z^{hs} - \sum_i x_i \left(m_i - 1\right) \left(g_{ii}^{hs}\right)^{-1} \rho \frac{\partial g_{ii}^{hs}}{\partial \rho} \tag{A.1}$$

$$Z^{hs} = \frac{\zeta_3}{\left(1-\zeta_3\right)} + \frac{3\zeta_1\zeta_2}{\zeta_0\left(1-\zeta_3\right)^2} + \frac{3\zeta_2^3 - \zeta_3\zeta_2^3}{\zeta_0\left(1-\zeta_3\right)^3} \tag{A.2}$$

$$g_{ij}^{hs} = \frac{1}{\left(1-\zeta_3\right)} + \left(\frac{d_i d_j}{d_i + d_j}\right) \frac{3\zeta_2}{\left(1-\zeta_3\right)^2} + \left(\frac{d_i d_j}{d_i + d_j}\right)^2 \frac{2\zeta_2^2}{\left(1-\zeta_3\right)^3} \tag{A.3}$$

$$\zeta_{0,\ldots,3} = \frac{\pi}{6} \rho \sum_i x_i m_i d_i^{0,\ldots,3} \tag{A.4}$$

$$d_i = \sigma_i \left[1 - 0.12 \exp\left(-3\frac{u_i}{kT}\right)\right] \tag{A.5}$$

A.1.2 Perturbation Contribution

The perturbation contribution Z^{disp} describes the attractive part of the interacting chains within PC-SAFT. Its derivation is given in [60]. It is a function of the packing fraction $\eta = \zeta_3$, which describes a reduced segment density for a given segment diameter σ. η is calculated iteratively and the following initial and boundary values are recommended: $\eta_0 = 0.5$ for liquid, $\eta_0 = 10^{-10}$ for gas phase, and $\eta \leq 0.7405$. Additionally, for the calculation, universal model constants are given in Table A.1.

$$Z^{disp} = -2\pi\rho\frac{\partial\left(\eta I_1\right)}{\partial\eta}\overline{m^2u\sigma^3} - \pi\rho\overline{m}\left[C\frac{\partial\left(\eta I_2\right)}{\partial\eta} + \eta I_2\frac{\partial C}{\partial\eta}\right]\overline{m^2u^2\sigma^3} \tag{A.6}$$

$$I_1 = \sum_{i=0}^{6} a_i\eta^i \tag{A.7}$$

$$I_2 = \sum_{i=0}^{6} b_i\eta^i \tag{A.8}$$

$$a_i = a_{0i} + \frac{\overline{m}-1}{\overline{m}}a_{1i} + \frac{\overline{m}-1}{\overline{m}}\frac{\overline{m}-2}{\overline{m}}a_{2i} \tag{A.9}$$

$$b_i = b_{0i} + \frac{\overline{m}-1}{\overline{m}}b_{1i} + \frac{\overline{m}-1}{\overline{m}}\frac{\overline{m}-2}{\overline{m}}b_{2i} \tag{A.10}$$

$$\overline{m^2u\sigma^3} = \sum_i\sum_j x_ix_jm_im_j\left(\frac{u_{ij}}{kT}\right)\sigma_{ij}^3 \tag{A.11}$$

$$\overline{m^2u^2\sigma^3} = \sum_i\sum_j x_ix_jm_im_j\left(\frac{u_{ij}}{kT}\right)^2\sigma_{ij}^3 \tag{A.12}$$

$$C = \left(1 + \overline{m}\frac{8\eta - 2\eta^2}{(1-\eta)^4} + (1-\overline{m})\frac{20\eta - 27\eta^2 + 12\eta^3 - 2\eta^4}{\left[(1-\eta)(2-\eta)\right]^2}\right) \tag{A.13}$$

Table A.1: Universal model constants, acquired from [60], used in Eqs. (A.9) and (A.10).

i	a_{0i}	a_{1i}	a_{2i}	b_{0i}	b_{1i}	b_{2i}
0	0.9105631445	-0.3084016918	-0.0906148351	0.7240946941	-0.5755498075	0.0976883116
1	0.6361281449	0.1860531159	0.4527842806	2.2382791861	0.6995095521	-0.2557574982
2	2.6861347891	-2.5030047259	0.5962700728	-4.0025849485	3.8925673390	-9.1558561530
3	-26.547362491	21.419793629	-1.7241829131	-21.003576815	-17.215471648	20.642075974
4	97.759208784	-65.255885330	-4.1302112531	26.855641363	192.67226447	-38.804430052
5	-159.59154087	83.318680481	13.776631870	206.55133841	-161.82646165	93.626774077
6	91.297774084	-33.746922930	-8.6728470368	-355.60235612	-165.20769346	-29.666905585

A.1.3 Association Contribution

In PC-SAFT, the association contribution Z^{assoc} describes the influences imposed by hydrogen bonds onto the interacting chains. In the calculations, the fraction x^{A_i} not bonded at a specific site A of a molecule i is considered as well as the strength of interaction $\Delta^{A_iB_j}$ between sites A_i and B_j. Its calculation is given in greater detail in [59].

$$Z^{assoc} = \sum_i x_i \frac{\mu_i^{assoc}}{RT} - \frac{\tilde{a}^{assoc}}{RT} \tag{A.14}$$

$$\frac{\mu_i^{assoc}}{RT} = \sum_{A_i} \left[\ln\left(x^{A_i}\right) - \frac{x^{A_i}}{2} \right] + \frac{M_i}{2} + \sum_j \rho_j \sum_{A_j} \left[\left(\frac{\partial x^{A_j}}{\partial \rho_j} \right)_{T,\rho_{k\neq i}} \left[\frac{1}{x^{A_j}} - \frac{1}{2} \right] \right] \tag{A.15}$$

$$\frac{\tilde{a}^{assoc}}{RT} = \sum_i x_i \left[\sum_{A_i} \left[\ln\left(x^{A_i}\right) - \frac{x^{A_i}}{2} \right] + \frac{M_i}{2} \right] \tag{A.16}$$

$$x^{A_i} = \left[1 + N_{Av} \sum_j \sum_{B_j} \rho_j x^{B_j} \Delta^{A_iB_j} \right]^{-1} \tag{A.17}$$

$$\Delta^{A_iB_j} = d_{ij}^3 g_{ij}^{seg} \kappa^{A_iB_j} \left[\exp \frac{\varepsilon^{A_iB_j}}{kT} - 1 \right] \tag{A.18}$$

$$d_{ij} = \frac{1}{2}\left(d_i + d_j\right) \tag{A.19}$$

$$g_{ij}^{seg} \approx g_{ij}^{hs} \tag{A.20}$$

A.1.4 Calculation of Residual Chemical Potential

To calculate the fugacity coefficient φ using Eq. (2.27), the residual chemical potential has to be determined. Its calculation is based on various contributions of the molar Helmholtz energy $\tilde{a}$, which are calculated analogue to the compressibility contribution given previously in this chapter. Their calculations are given in [60] and are listed below.

$$\frac{\mu_k^{res}}{kT} = \tilde{a}^{res} + (Z-1) + \left(\frac{\partial \tilde{a}^{res}}{\partial x_k}\right)_{T,v,x_{j\neq k}} - \sum_{j=1}^{N}\left[x_j\left(\frac{\partial \tilde{a}^{res}}{\partial x_j}\right)_{T,v,x_{i\neq j}}\right] \tag{A.21}$$

$$\tilde{a}^{res} = \tilde{a}^{hc} + \tilde{a}^{disp} + \tilde{a}^{assoc} \tag{A.22}$$

$$\tilde{a}^{hc} = \overline{m}\tilde{a}^{hs} - \sum_i x_i\left(m_i - 1\right)\ln\left(g_{ii}^{hs}\right) \tag{A.23}$$

$$\tilde{a}^{hs} = \frac{1}{\zeta_0}\left[\frac{3\zeta_1\zeta_2}{(1-\zeta 3)} + \frac{\zeta_2^3}{\zeta_3\left(1-\zeta_3\right)^2} + \left(\frac{\zeta_2^3}{\zeta_3^2} - \zeta_0\right)\ln\left(1-\zeta_3\right)\right] \tag{A.24}$$

$$\tilde{a}^{disp} = -2\pi\rho I_1\overline{m^2u\sigma^3} - \pi\rho\overline{m}CI_2\overline{m^2u^2\sigma^3} \tag{A.25}$$

A.2 Solid-Liquid Equilibrium Data Sets

In this section, various experimental solid-liquid equilibrium data sets are listed. Additionally, for these data sets, standard uncertainties in terms of composition and temperature are given, determined via triplicate measurement. Their calculation is explained in Section **3.2.2**. Further, the solid-liquid equilibria were used to fit model parameters of Eqs. (2.40) and (2.42) to experimental data sets. The resulting parameters are given in this section as well. For data sets containing measurements of solid solutions in water/anti-solvent mixtures, representative PXRD patterns to validate solid solution formations are additionally shown below.

Table A.2: Liquid and solid molar fractions of L-valine /L-leucine in water determined at 25°C. Measured by M.Sc. S. Münzberg, published in [3].

$x_{L-Val,L}$	$x_{L-Leu,L}$	$x_{L-Val,S}$	$x_{L-Leu,S}$
0.0093	0.0000	1.0000	0.0000
0.0119	0.0012	0.8922	0.1078
0.0128	0.0018	0.7125	0.2875
0.0113	0.0023	0.3664	0.6336
0.0087	0.0028	0.2346	0.7654
0.0057	0.0031	0.1170	0.8830
0.0042	0.0031	0.1052	0.8948
0.0009	0.0031	0.0163	0.9837
0.0000	0.0031	0.0000	1.0000

Table A.3: Polynomial parameters fitted to Eq. (2.40), with $M_A = M_B = 4$ for L-valine /L-leucine solubilities in water at 25 °C. Published in [1].

$a_{m,i}/b_{m,i}$	L-Valine	L-Leucine
1,1	-0.013	-0.029
2,1	0.033	0.065
3,1	-0.058	-0.048
4,1	0.048	0.015

Table A.4: Liquid and solid molar fractions of L-valine /L-leucine in water determined at 40°C. Measured by M.Sc. S. Münzberg, unpublished.

$x_{L-Val,L}$	$x_{L-Leu,L}$	$x_{L-Val,S}$	$x_{L-Leu,S}$
0.0103	0.0000	1.0000	0.0000
0.0121	0.0015	0.9046	0.0954
0.0125	0.0020	0.7695	0.2305
0.0125	0.0024	0.4802	0.5198
0.0085	0.0031	0.2398	0.7602
0.0063	0.0034	0.1276	0.8724
0.0044	0.0035	0.0777	0.9223
0.0029	0.0035	0.0455	0.9545
0.0013	0.0036	0.0157	0.9843
0.0004	0.0037	0.0059	0.9941

Table A.5: Polynomial parameters fitted to Eq. (2.40), with $M_A = M_B = 4$ for L-valine /L-leucine solubilities in water at 40 °C.

$a_{m,i}/b_{m,i}$	L-Valine	L-Leucine
1,1	-0.059	-0.028
2,1	0.136	0.067
3,1	-0.130	-0.053
4,1	0.062	0.018

Table A.6: Solubilities of L-leucine in various solvents from 298.35 to 337.95 K. Published in [2].

T [K]	$x_{L-Leu,L} \cdot 10^{-4}$		
	Ethanol	Isopropanol	Acetone
298.35	0.7484	0.1362	0.7567
308.35	0.8771	0.1779	1.1912
318.35	1.0864	0.2203	1.8479
327.95	1.3456	0.2905	-
337.95	1.6174	0.3485	-

Standard uncertainties are $\sigma(T) = 0.2\,K$, $U(x_L) \leq 1.45 \cdot 10^{-6}$ for ethanol, $U(x_L) \leq 7.07 \cdot 10^{-7}$ for isopropanol, and $U(x_L) \leq 2.55 \cdot 10^{-6}$ for acetone (for a 95 % level of confidence).

Table A.7: Liquid and solid molar fractions of L-valine /L-leucine in various water/ethanol mixtures determined at 25 °C. Partly published in [1].

$x_{L-Val,L}$	$x_{L-Leu,L}$	$x_{EtOH,L}$	$x_{L-Val,S}$	$x_{L-Leu,S}$
0.0035	0.0000	0.1585	1.0000	0.0000
0.0043	0.0005	0.1617	0.9214	0.0786
0.0043	0.0006	0.1619	0.8985	0.1015
0.0043	0.0007	0.1619	0.8332	0.1668
0.0048	0.0011	0.1613	0.6053	0.3947
0.0045	0.0015	0.1620	0.3043	0.6957
0.0019	0.0014	0.1537	0.1054	0.8946
0.0007	0.0014	0.1621	0.0308	0.9692
0.0000	0.0014	0.1628	0.0000	1.0000
0.0026	0.0000	0.2323	1.0000	0.0000
0.0031	0.0004	0.2265	0.9244	0.0756
0.0033	0.0006	0.2298	0.8884	0.1116
0.0035	0.0007	0.2300	0.8247	0.1753
0.0037	0.0010	0.2297	0.6891	0.3109
0.0034	0.0012	0.2293	0.3830	0.6170
0.0016	0.0015	0.2308	0.1475	0.8525
0.0006	0.0014	0.2314	0.0431	0.9569
0.0000	0.0014	0.2323	0.0000	1.0000
0.0022	0.0000	0.2750	1.0000	0.0000
0.0027	0.0003	0.2768	0.9266	0.0734
0.0029	0.0004	0.2769	0.8994	0.1006
0.0031	0.0006	0.2774	0.8323	0.1677
0.0032	0.0008	0.2774	0.7083	0.2917
0.0026	0.0012	0.2772	0.3213	0.6787
0.0014	0.0012	0.2774	0.0834	0.9166
0.0006	0.0014	0.2788	0.0406	0.9594
0.0000	0.0013	0.2781	0.0000	1.0000

Standard uncertainties are $\sigma(T) = 0.2\,K$, $U(x_L) \leq 0.0002$ and $U(x_S) \leq 0.0097$ (for a 95 % level of confidence).

Table A.8: Polynomial parameters fitted to Eq. (2.42), with $M_A = M_B = 4$ for L-valine /L-leucine solubilities in water/ethanol mixtures at 25 °C. Published in [1].

$a_{m,i}/b_{m,i}$	L-Valine	L-Leucine
1,2	-3.393	-3.765
2,2	-2.588	-3.913
3,2	-3.128	-3.823
4,2	-3.916	-3.190

Table A.9: Liquid and solid molar fractions of L-valine /L-leucine in various water/ethanol mixtures determined at $40°C$.

$x_{L-Val,L}$	$x_{L-Leu,L}$	$x_{EtOH,L}$	$x_{L-Val,S}$	$x_{L-Leu,S}$
0.0042	0.0000	0.1641	1.0000	0.0000
0.0054	0.0007	0.1650	0.9094	0.0906
0.0055	0.0009	0.1662	0.8842	0.1158
0.0059	0.0011	0.1657	0.8397	0.1603
0.0052	0.0017	0.1624	0.4993	0.5007
0.0039	0.0020	0.1669	0.2993	0.7007
0.0029	0.0021	0.1652	0.1676	0.8324
0.0008	0.0019	0.1658	0.0177	0.9823
0.0000	0.0019	0.1661	0.0000	1.0000
0.0034	0.0000	0.2299	1.0000	0.0000
0.0047	0.0007	0.2302	0.9230	0.0770
0.0049	0.0009	0.2299	0.8978	0.1022
0.0051	0.0010	0.2295	0.8710	0.1290
0.0052	0.0017	0.2291	0.5026	0.4974
0.0041	0.0020	0.2314	0.3240	0.6760
0.0029	0.0022	0.2291	0.2161	0.7839
0.0009	0.0022	0.2295	0.0497	0.9503
0.0000	0.0021	0.2303	0.0000	1.0000
0.0028	0.0000	0.2850	1.0000	0.0000
0.0037	0.0005	0.2846	0.9347	0.0653
0.0039	0.0006	0.2837	0.8995	0.1005
0.0039	0.0008	0.2839	0.8958	0.1042
0.0041	0.0013	0.2843	0.6376	0.3624
0.0033	0.0016	0.2846	0.4425	0.5575
0.0024	0.0017	0.2839	0.2487	0.7513
0.0007	0.0017	0.2844	0.0753	0.9247
0.0000	0.0017	0.2846	0.0000	1.0000

Standard uncertainties are $\sigma(T) = 0.2\,K$, $U(x_L) \leq 0.0001$ and $U(x_S) \leq 0.0282$ (for a 95 % level of confidence).

Table A.10: Polynomial parameters fitted to Eq. (2.42), with $M_A = M_B = 4$ for L-valine /L-leucine solubilities in water/ethanol mixtures at 40 °C.

$a_{m,i}/b_{m,i}$	L-Valine	L-Leucine
1,2	-3.228	-2.055
2,2	-4.340	-2.228
3,2	-4.847	-2.193
4,2	-3.959	-1.800

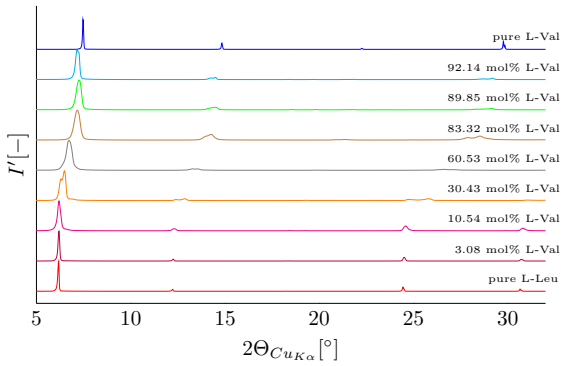

(a) 25 °C, $\overline{\zeta}_{EtOH} = 0.1924$

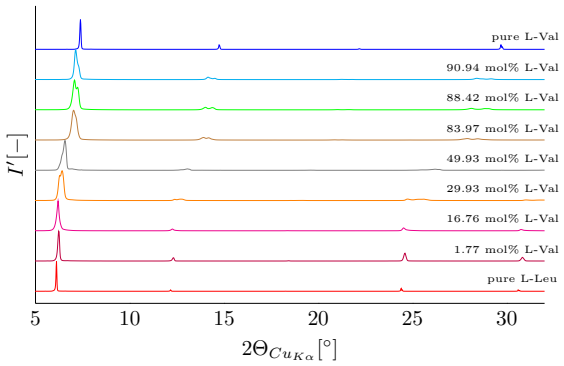

(b) 40 °C, $\overline{\zeta}_{EtOH} = 0.1992$

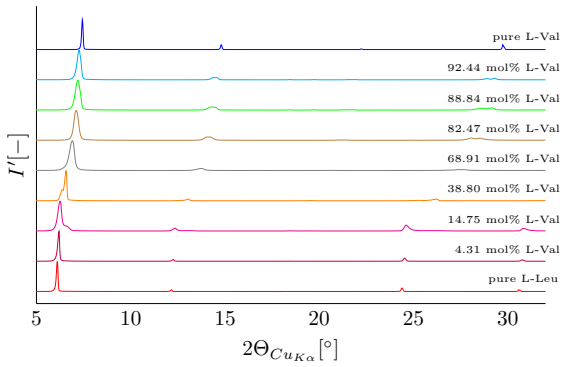

(c) 25 °C, $\overline{\zeta}_{EtOH} = 0.3004$

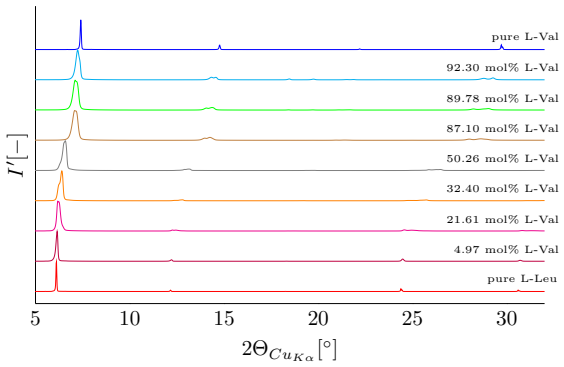

(d) 40 °C, $\overline{\zeta}_{EtOH} = 0.3004$

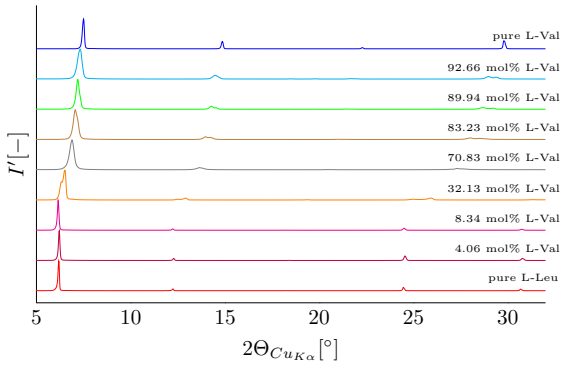

(e) 25 °C, $\overline{\zeta}_{EtOH} = 0.3851$

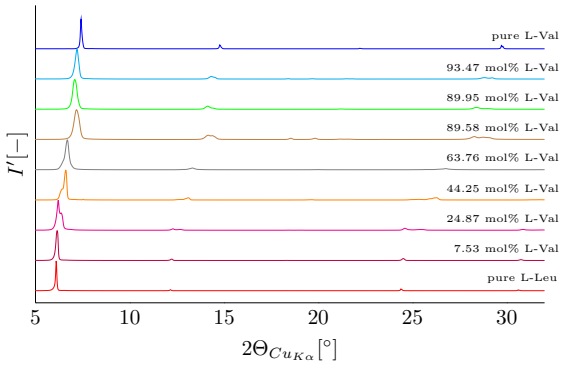

(f) 40 °C, $\overline{\zeta}_{EtOH} = 0.3995$

Figure A.1: PXRD patterns of various L-valine and L-leucine mixtures, recrystallized from different water/ethanol mixtures and equilibrated at 25 and 40 °C. Partly published in [1].

Table A.11: Liquid and solid molar fractions of L-valine /L-leucine in various water/isopropanol mixtures determined at 25 °C. Published in [2].

$x_{L-Val,L}$	$x_{L-Leu,L}$	$x_{IPA,L}$	$x_{L-Val,S}$	$x_{L-Leu,S}$
0.0048	0.0000	0.0900	1.0000	0.0000
0.0060	0.0006	0.0903	0.9182	0.0818
0.0065	0.0008	0.0910	0.8797	0.1203
0.0065	0.0010	0.0901	0.8302	0.1698
0.0068	0.0014	0.0905	0.4718	0.5282
0.0047	0.0017	0.0907	0.2728	0.7272
0.0022	0.0019	0.0907	0.0706	0.9294
0.0008	0.0018	0.0910	0.0351	0.9649
0.0000	0.0018	0.0912	0.0000	1.0000
0.0034	0.0000	0.1641	1.0000	0.0000
0.0047	0.0006	0.1655	0.9118	0.0882
0.0046	0.0006	0.1650	0.8999	0.1001
0.0048	0.0008	0.1651	0.8416	0.1584
0.0048	0.0012	0.1652	0.7318	0.2682
0.0040	0.0015	0.1650	0.3799	0.6201
0.0020	0.0018	0.1675	0.1353	0.8647
0.0007	0.0017	0.1658	0.0550	0.9450
0.0000	0.0017	0.1662	0.0000	1.0000
0.0027	0.0000	0.2310	1.0000	0.0000
0.0035	0.0005	0.2315	0.9307	0.0693
0.0037	0.0005	0.2293	0.9055	0.0945
0.0039	0.0007	0.2288	0.8575	0.1425
0.0041	0.0011	0.2290	0.7614	0.2386
0.0037	0.0014	0.2293	0.4101	0.5899
0.0020	0.0017	0.2298	0.1434	0.8566
0.0008	0.0017	0.2311	0.0834	0.9166
0.0000	0.0016	0.2339	0.0000	1.0000

Standard uncertainties are $\sigma(T) = 0.2\,K$, $U(x_L) \leq 0.0004$ and $U(x_S) \leq 0.0300$ (for a 95 % level of confidence).

Table A.12: Polynomial parameters fitted to Eq. (2.42), with $M_A = M_B = 4$ for L-valine /L-leucine solubilities in water/isopropanol mixtures at 25 °C.

$a_{m,i}/b_{m,i}$	L-Valine	L-Leucine
1,2	0.664	-3.228
2,2	-0.437	-3.370
3,2	-3.014	-3.207
4,2	-4.218	-2.571

Table A.13: Liquid and solid molar fractions of L-valine /L-leucine in various water/isopropanol mixtures determined at $40°C$.

$x_{L-Val,L}$	$x_{L-Leu,L}$	$x_{IPA,L}$	$x_{L-Val,S}$	$x_{L-Leu,S}$
0.0049	0.0000	0.1654	1.0000	0.0000
0.0067	0.0008	0.1658	0.9128	0.0872
0.0065	0.0010	0.1656	0.8955	0.1045
0.0067	0.0012	0.1656	0.8636	0.1364
0.0063	0.0021	0.1648	0.5485	0.4515
0.0047	0.0023	0.1658	0.4119	0.5881
0.0035	0.0026	0.1659	0.2248	0.7752
0.0010	0.0025	0.1664	0.0561	0.9439
0.0000	0.0020	0.1957	0.0000	1.0000
0.0038	0.0000	0.2185	1.0000	0.0000
0.0047	0.0006	0.2282	0.9190	0.0810
0.0050	0.0008	0.2283	0.8902	0.1098
0.0051	0.0009	0.2282	0.8717	0.1283
0.0053	0.0016	0.2282	0.6785	0.3215
0.0042	0.0020	0.2285	0.4658	0.5342
0.0032	0.0023	0.2284	0.2605	0.7395
0.0009	0.0023	0.2286	0.0484	0.9516
0.0000	0.0023	0.2291	0.0000	1.0000

Standard uncertainties are $\sigma(T) = 0.2\,K$, $U(x_L) \leq 0.0003$ and $U(x_S) \leq 0.0084$ (for a 95 % level of confidence).

Table A.14: Polynomial parameters fitted to Eq. (2.42), with $M_A = M_B = 4$ for L-valine /L-leucine solubilities in water/isopropanol mixtures at 40 °C.

$a_{m,i}/b_{m,i}$	L-Valine	L-Leucine
1,2	-1.739	-3.627
2,2	-3.191	-3.845
3,2	-4.933	-3.500
4,2	-5.043	-2.277

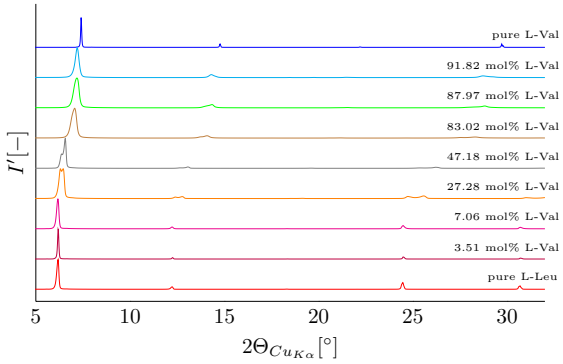

(a) 25 °C, $\overline{\zeta}_{IPA} = 0.1002$

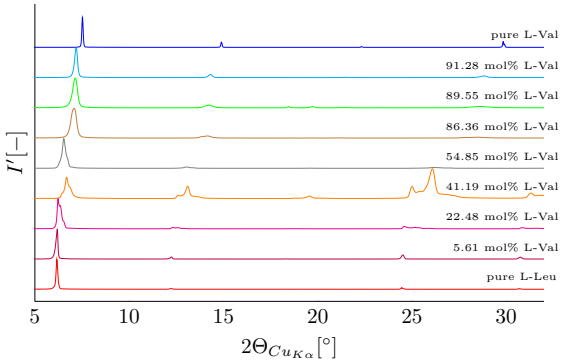

(b) 40 °C, $\overline{\zeta}_{IPA} = 0.2002$

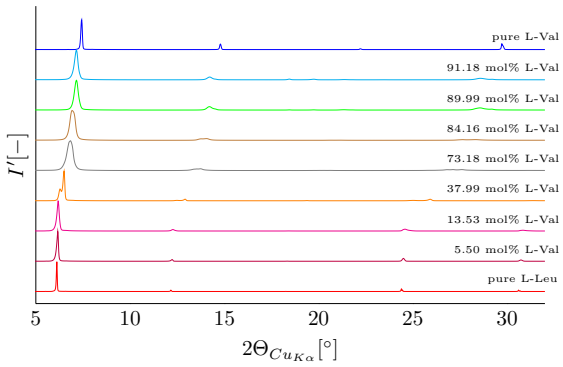

(c) 25 °C, $\overline{\zeta}_{IPA} = 0.1990$

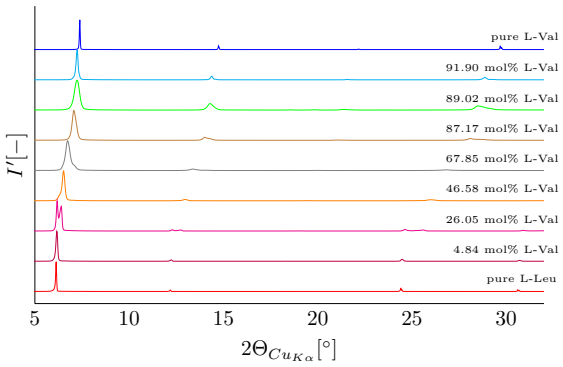

(d) 40 °C, $\overline{\zeta}_{IPA} = 0.2962$

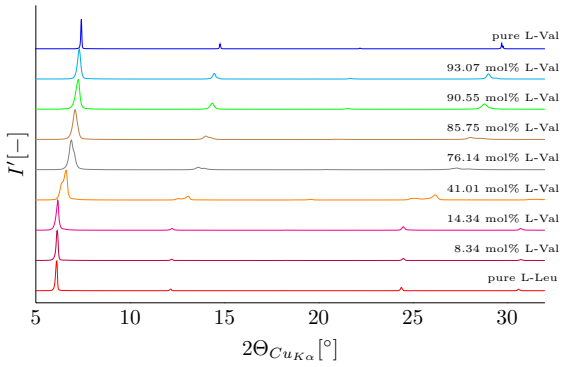

(e) 25 °C, $\overline{\zeta}_{IPA} = 0.3008$

Figure A.2: PXRD patterns of various L-valine and L-leucine mixtures, recrystallized from different water/isopropanol mixtures and equilibrated at 25 and 40 °C. Partly published in [2].

Table A.15: Liquid and solid molar fractions of L-valine /L-leucine in various water/acetone mixtures determined at 25 °. Published in [2].

$x_{L-Val,L}$	$x_{L-Leu,L}$	$x_{Ace,L}$	$x_{L-Val,S}$	$x_{L-Leu,S}$
0.0059	0.0000	0.0899	1.0000	0.0000
0.0073	0.0007	0.0894	0.9351	0.0650
0.0078	0.0010	0.0900	0.8998	0.1002
0.0080	0.0014	0.0897	0.8100	0.1900
0.0070	0.0016	0.0896	0.4012	0.5988
0.0054	0.0024	0.0896	0.2247	0.7753
0.0025	0.0024	0.0906	0.0836	0.9164
0.0009	0.0023	0.0902	0.0261	0.9739
0.0000	0.0023	0.0907	0.0000	1.0000
0.0045	0.0000	0.1062	1.0000	0.0000
0.0054	0.0006	0.1090	0.9426	0.0574
0.0056	0.0009	0.1115	0.8762	0.1238
0.0057	0.0010	0.1118	0.8381	0.1619
0.0058	0.0013	0.1109	0.6494	0.3506
0.0048	0.0016	0.1098	0.3609	0.6391
0.0023	0.0017	0.1120	0.0866	0.9134
0.0009	0.0017	0.1127	0.0420	0.9580
0.0000	0.0016	0.1132	0.0000	1.0000
0.0039	0.0000	0.1290	1.0000	0.0000
0.0044	0.0005	0.1280	0.9381	0.0619
0.0049	0.0007	0.1309	0.8950	0.1050
0.0051	0.0009	0.1286	0.8458	0.1542
0.0050	0.0011	0.1299	0.7231	0.2769
0.0045	0.0014	0.1292	0.3965	0.6035
0.0023	0.0016	0.1282	0.0997	0.9003
0.0008	0.0009	0.1297	0.0036	0.9964
0.0000	0.0008	0.1306	0.0000	1.0000

Standard uncertainties are $\sigma(T) = 0.2\,K$, $U(x_L) \leq 0.0002$ and $U(x_S) \leq 0.0124$ (for a 95 % level of confidence).

Table A.16: Polynomial parameters fitted to Eq. (2.42), with $M_A = M_B = 4$ for L-valine /L-leucine solubilities in water/acetone mixtures at 25 °C.

$a_{m,i}/b_{m,i}$	L-Valine	L-Leucine
1,2	-0.466	-3.870
2,2	-3.227	-4.110
3,2	-8.171	-4.063
4,2	-9.454	-3.964

Table A.17: Liquid and solid molar fractions of L-valine /L-leucine in various water/acetone mixtures determined at 40 °C.

$x_{L-Val,L}$	$x_{L-Leu,L}$	$x_{Ace,L}$	$x_{L-Val,S}$	$x_{L-Leu,S}$
0.0046	0.0000	0.0856	1.0000	0.0000
0.0059	0.0007	0.0882	0.9067	0.0933
0.0060	0.0008	0.0889	0.8703	0.1297
0.0063	0.0011	0.0821	0.8462	0.1538
0.0052	0.0016	0.0892	0.4198	0.5802
0.0040	0.0018	0.0901	0.3014	0.6986
0.0030	0.0020	0.0900	0.1635	0.8365
0.0009	0.0020	0.0903	0.0495	0.9505
0.0000	0.0020	0.0900	0.0000	1.0000
0.0040	0.0000	0.1063	1.0000	0.0000
0.0051	0.0006	0.1100	0.9158	0.0842
0.0052	0.0008	0.1097	0.8820	0.1180
0.0051	0.0010	0.1096	0.8694	0.1306
0.0050	0.0015	0.1095	0.4970	0.5030
0.0039	0.0017	0.1095	0.3385	0.6615
0.0028	0.0018	0.1101	0.1861	0.8139
0.0008	0.0018	0.1107	0.0535	0.9465
0.0000	0.0016	0.1108	0.0000	1.0000
0.0037	0.0000	0.1291	1.0000	0.0000
0.0047	0.0007	0.1292	0.9219	0.0781
0.0050	0.0008	0.1289	0.8929	0.1071
0.0051	0.0010	0.1287	0.8605	0.1395
0.0049	0.0016	0.1281	0.6367	0.3633
0.0040	0.0017	0.1270	0.3918	0.6082
0.0030	0.0019	0.1291	0.2032	0.7968
0.0009	0.0019	0.1242	0.0436	0.9564
0.0000	0.0019	0.1292	0.0000	1.0000

Standard uncertainties are $\sigma(T) = 0.2\,K$, $U(x_L) \leq 0.0001$ and $U(x_S) \leq 0.0069$ (for a 95 % level of confidence).

Table A.18: Polynomial parameters fitted to Eq. (2.42), with $M_A = M_B = 4$ for L-valine /L-leucine solubilities in water/acetone mixtures at 40 °C.

$a_{m,i}/b_{m,i}$	L-Valine	L-Leucine
1,2	-7.612	-5.603
2,2	-9.780	-5.980
3,2	-11.150	-5.748
4,2	-9.862	-4.784

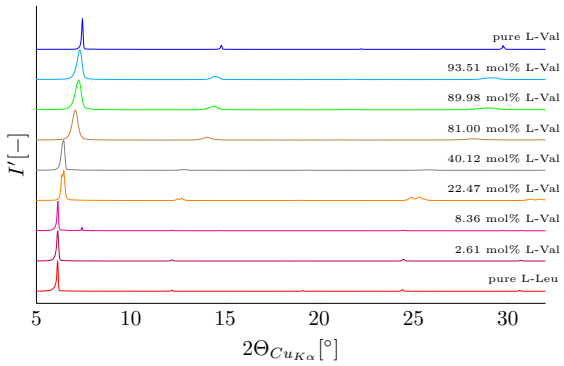

(a) 25 °C, $\overline{\zeta}_{Ace} = 0.0996$

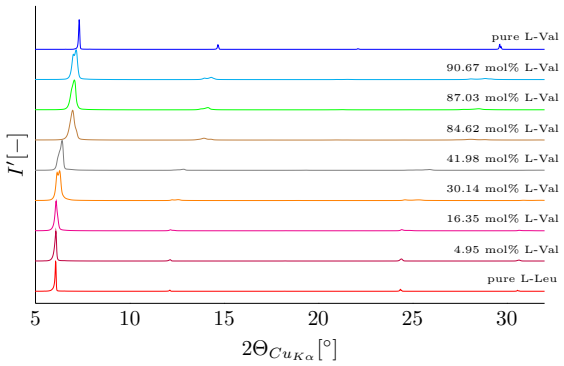

(b) 40 °C, $\overline{\zeta}_{Ace} = 0.0974$

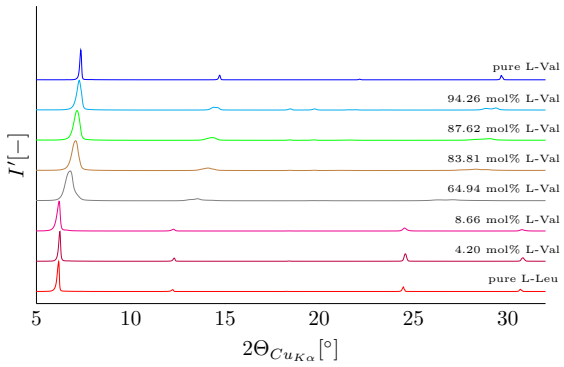

(c) 25 °C, $\overline{\zeta}_{Ace} = 0.1253$

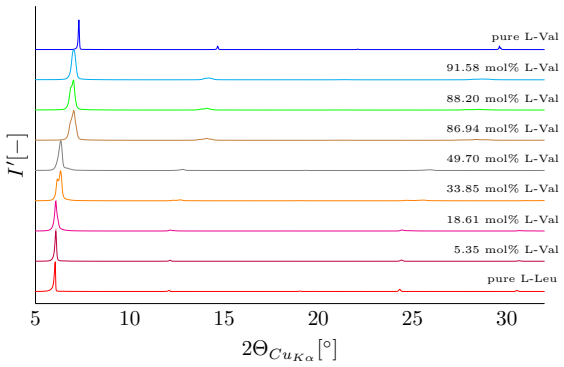

(d) 40 °C, $\overline{\zeta}_{Ace} = 0.1237$

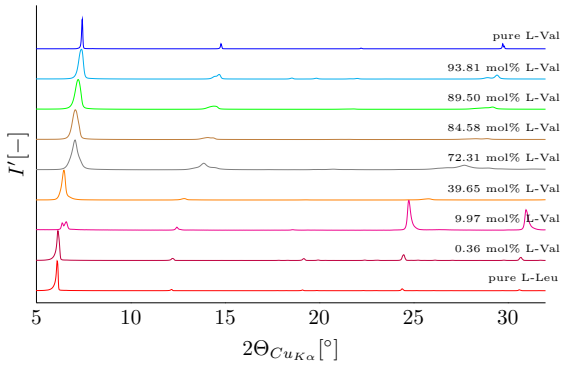

(e) 25 °C, $\overline{\zeta}_{Ace} = 0.1493$

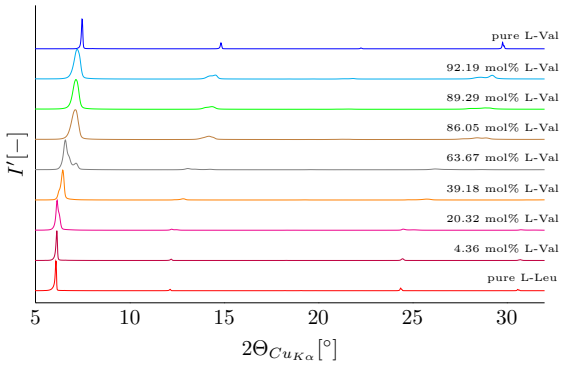

(f) 40 °C, $\overline{\zeta}_{Ace} = 0.1478$

Figure A.3: PXRD patterns of various L-valine and L-leucine mixtures, recrystallized from different water/acetone mixtures and equilibrated at 25 and 40 °C. Partly published in [2].

A.3 Thermodynamic Model Parameters and Melting Data

This section lists the model parameters for PC-SAFT and NRTL, which were either gathered from literature, and indicated accordingly, or fitted to experimental data sets. Further, melting properties of L-valine and L-leucine , which were determined via FSC in [64] are listed below. All of these parameters are used in the thermodynamic modeling of solid solution equilibria in Section **3.4**.

Table A.19: Component specific parameters and binary interaction parameters k_{ij} for water used in the PC-SAFT calculation. Table taken from [2].

Component	m	σ [Å]	$\frac{u}{k}$ [K]	$\frac{\varepsilon^{A_iB_i}}{k}$ [K]	$\kappa^{A_iB_i}$	$k_{ij}(H_2O)_{T_0}$	$k_{ij}(H_2O)_{T-T_0}$	Ref.
L-Valine	7.4851	2.5888	306.41	3183.80	0.0385	-0.0757[a]	3.85E-4	[76]
L-Leucine	8.3037	2.7000	330.00	3600.00	0.0200	-0.0630[a]	4.09E-4	[76]
Water	1.2047	*	353.94	2425.67	0.0451	0.0000	0.0000	[106]
Ethanol	2.3827	3.1771	198.24	2653.40	0.0324	-0.2663[b]	6.86E-4	[106]
Isopropanol	3.0930	3.2090	208.42	2253.90	0.0250	-0.2817[b]	7.12E-4	[107]
Acetone	2.8910	3.2280	247.42	0.0000	0.0300	-0.1563[b]	2.83E-4	[107]

*: $\sigma = 2.7927 + 10.11 \cdot \exp(-0.01775 \cdot T) - 1.417 \cdot \exp(-0.01146 \cdot T)$; a: $T_0 = 298.15$ K; b: $T_0 = 0$ K.

Table A.20: Binary interaction parameters k_{ij} between L-valine /L-leucine and various antisolvents fitted to pure solubility data in this work. Published in [2].

Component	L-Valine		L-Leucine	
	k_{ij,T_0}	$k_{ij,T-T_0}$	k_{ij,T_0}	$k_{ij,T-T_0}$
Ethanol	-0.0613	4.38E-4	-0.1147	7.45E-4
Isopropanol	-0.0160	6.04E-4	-0.0720	7.54E-4
Acetone	-0.0045	2.53E-4	-0.1032	5.38E-5

$T_0 = 298.15$ K.

Table A.21: NRTL parameter fitted in this work to solubility data in water at 25 °C. Published in [3].

$b_{L-Val,L-Leu}\,[J\,mol^{-1}]$	$b_{L-Leu,L-Val}\,[J\,mol^{-1}]$	α
3294632.26	-3228689.34	1.43E-5

Table A.22: Melting temperatures and molar melting enthalpies used in this work. Obtained from [64].

Component	T_m [K]	$\Delta H_m\,[kJ\,mol^{-1}]$
L-Valine	529	46.72
L-Leucine	518	49.09

Table A.23: Solid and liquid phase heat capacity slope and intercept parameters used in Eq. (A.26) of this work. Obtained from [64].

Component	$a^L_{p,m}\,[J\,mol^{-1}\,K^{-2}]$	$a^S_{p,m}\,[J\,mol^{-1}\,K^{-2}]$	$b^L_{p,m}\,[J\,mol^{-1}\,K^{-1}]$	$b^S_{p,m}\,[J\,mol^{-1}\,K^{-1}]$
L-Valine	0.351	0.453	106.488	32.573
L-Leucine	0.525	0.577	71.622	24.322

$$\Delta C_{p,m,i}(T) = \left(a^L_{p,m,i} - a^S_{p,m,i}\right) \cdot T + \left(b^L_{p,m,i} - b^S_{p,m,i}\right) \tag{A.26}$$

A.4 Detailed Flow Sheet of the Counter-Current Crystallization Pilot Plant

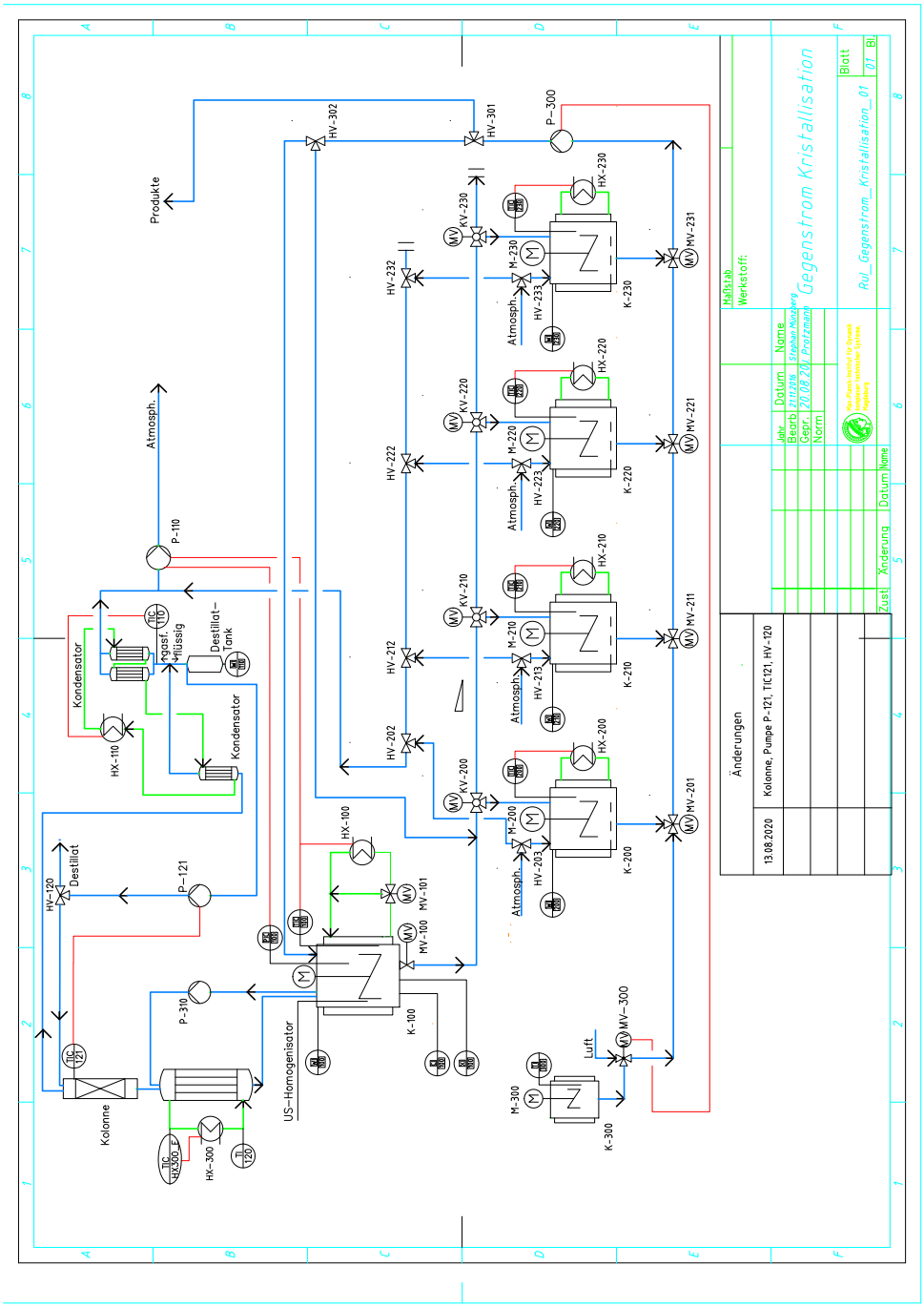

Figure A.4: Piping and instrumentation diagram of the counter-current crystallization pilot plant at the MPI Magdeburg.

A.5 Conference Contributions

Here, various conference contributions related to this dissertation are listed.
Presenting Authors are underlined.

A.5.1 Conference Proceedings

- „Conceptual Design of a Counter-Current Crystallization Process“
  V. Tenberg, M. Sadeghi, A. Seidel-Morgenstern, and H. Lorenz
  Chem.Ing.Tech. 2022, 94, No. 9, (Bio)Process Engineering – a Key to Sustainable Development, Aachen, Germany, p. 1343-1344

- „Amino Acid Intermediate Compound Produced via Liquid-Assisted Grinding“
  V. Tenberg and H. Lorenz
  Proceedings 27th International Workshop on Industrial Crystallization, Espoo, Finland, pp. 161-165

- „Separation of solid solutions using counter-current crystallization“
  V.Tenberg, S. Münzberg, M. Sadeghi, H. Lorenz, and A. Seidel-Morgenstern
  Book of Abstracts 21st International Symposium on Industrial Crystallization, Online Event, pp. 147-150

- „Thermodynamic description of phase diagrams in solid solution/solvent systems“
  M. Sadeghi, S. Münzberg, **V.Tenberg**, H. Lorenz, and A. Seidel-Morgenstern
  Book of Abstracts 21st International Symposium on Industrial Crystallization, Online Event, pp. 375-378

A.5.2 Presentations

- „Enhancement of Crystallization Behavior for Solid Solution Separation Using Different Antisolvents“
  V. Tenberg, M. Sadeghi, A. Seidel-Morgenstern, and H. Lorenz
  2022 American Insitute of Chemical Engineers Annual Meeting, Pheonix, AZ
  13.-18. November 2022

- „Conceptual Design of a Counter-Current Crystallization Process“
  V. Tenberg, M. Sadeghi, A. Seidel-Morgenstern, and H. Lorenz
  (Bio)Process Engineering – a Key to Sustainable Development, Aachen, Germany
  12.-15. September 2022

- „Phase Equilibria and Separation of Solid Solutions Using Solvent Mixtures in Counter-Current Crystallizers“
  V. Tenberg, M. Sadeghi, H. Lorenz, and A. Seidel-Morgenstern
  32nd European Symposium on Applied Thermodynamics 2022, Graz, Austria
  17.-20. July 2022

- „Separation of Solid Solutions Using Counter-Current Crystallization“
  V. Tenberg, S. Münzberg, M. Sadeghi, H. Lorenz, and A. Seidel-Morgenstern
  21st International Symposium on Industrial Crystallization, Online Event
  30. August – 2. September 2021

- „Separation of Solid Solutions Using Counter-Current Antisolvent Crystallization“
  V. Tenberg, M. Sadeghi, H. Lorenz, and A. Seidel-Morgenstern
  Annual Meeting of the ProcessNet-Group Crystallization, Online Event
  18.-19. March 2021

A.5.3 Posters

- „Recovery of natural substances from extracts based on solution thermodynamic considerations“
  S. Wünsche, M. Sadeghi, K. Oliynyk, **V. Tenberg**, A. Seidel-Morgenstern, and H. Lorenz
  International Conference On Properties And Phase Equilibria For Product And Process Design 2023, Tarragona, Spain
  21.-25. May 2023

- „Solid Phase Behavior and Stability Investigation of an Amino Acid Intermediate Compound Produced via Liquid-Assisted Grinding“
  V. Tenberg and H. Lorenz
  27th International Workshop on Industrial Crystallization, Espoo, Finland
  31. August – 2. September 2022

- „Description of Pharmaceuticals' Phase Diagrams for a Proper Solvent Selection Using PC-SAFT“
  M. Sadeghi, **V. Tenberg**, A. Seidel-Morgenstern, and H. Lorenz
  27th International Workshop on Industrial Crystallization, Espoo, Finland
  31. August – 2. September 2022

- „Solubility measurements and modeling of artemisinin in toluene/n-heptane mixtures“
  S. Wünsche, M. Sadeghi, **V. Tenberg**, K. Oliynyk, A. Seidel-Morgenstern, and H. Lorenz
  23rd European Symposium on Applied Thermodynamics 2022, Graz, Austria
  17.-20. July 2022

- „Thermodynamic description of phase diagrams in solid solution/solvent systems“
  M. Sadeghi, S. Münzberg, **V.Tenberg**, H. Lorenz, and A. Seidel-Morgenstern
  21st International Symposium on Industrial Crystallization, Online Event
  30. August – 2. September 2021

- „Phase Equilibria of Amino Acid Molecules Forming Solid Solutions“
  M. Sadeghi, S. Münzberg, **V.Tenberg**, H. Lorenz, and A. Seidel-Morgenstern
  31st European Symposium on Applied Thermodynamics 2021, Online Event
  5.-9. July 2021